ABSTRACT

Title of Dissertation: FLUID DYNAMICS OF EXTENSIONAL DEFORMATION AND CAPILLARY-DRIVEN BREAKUP OF DROPS AT LOW REYNOLDS NUMBER

Aditya Narendrababu Sangli
Doctor of Philosophy, 2021

Dissertation Directed by: Professor David I. Bigio
Department of Mechanical Engineering

In this dissertation, extensional deformation and capillary-driven breakup of drops at low Reynolds number is investigated using a combination of theoretical, experimental, and numerical techniques. The dissertation introduces a new non-dimensional measure for drop deformation, rationalizes previously unseen drop breakup behavior, and extends our overall understanding of the fluid dynamics behind drop deformation and breakup.

First, non-stagnant extensional deformation of Silicone oil drops in Castor oil is experimentally studied over a wide range of capillary numbers by injecting the drops along the centerline of a flow through a hyperbolic converging channel. The unique design of the channel is capable of imposing a constant extensional rate and is validated using lubrication theory. Based on a careful analysis of drop deformation at both small and large capillary numbers compared to the critical capillary number, a new measure called the semi-minor capillary number is introduced to characterize

drop behavior. Critical semi-minor capillary number is presented for a wide range of viscosity ratios and the significance of the new measure over the conventional capillary number measure is discussed.

During the course of the experiments, it was observed that drops undergoing non-stagnant extension exhibited a lag in velocity compared to the background flow velocity at the same point. This lag in velocity is attributed to flow induced deformation of the drops and the phenomenon is rationalized for a wide range of capillary numbers.

When drops are injected offset of the centerline of the channel, an anomalously large degree of deformation is observed even at low flow rates. A careful investigation of the phenomenon revealed that the strain rates along offset lines were at least an order of magnitude larger than the extensional rates along the centerline. A model is developed based on lubrication theory to predict the large deformation of drops and is successfully validated with experimental measurements.

Finally, in the absence of a forcing external flow, when slender drops are allowed to develop under the effect of interfacial tension they either retract into a sphere or breakup into multiple drops. This phenomenon is investigated using direct numerical simulations in a previously unexplored part of the parametric space where both inertial and viscous effects in the outside fluid are considered. A stability diagram is presented that shows a transition of drop states from asymptotically unstable to asymptotically stable states at different viscosity ratios. The drop behavior in different regimes is discussed and the significance of the balance between inertial and viscous forces is thoroughly described.

FLUID DYNAMICS OF EXTENSIONAL DEFORMATION AND CAPILLARY-DRIVEN BREAKUP OF DROPS AT LOW REYNOLDS NUMBER

by

Aditya Narendrababu Sangli

Dissertation submitted to the Faculty of the Graduate School of the
University of Maryland, College Park in partial fulfillment
of the requirements for the degree of
Doctor of Philosophy
2021

Advisory Committee:
Professor David I. Bigio, Chair & Advisor
Professor Amir Riaz
Professor James H. Duncan
Professor Kenneth Kiger
Professor Richard V. Calabrese, Dean's Representative

To my parents

Acknowledgments

I would like to thank several people who have supported me through the years as I completed this dissertation. First of all, I would like to thank my advisor, Professor David Bigio, for his mentorship throughout my graduate education. He afforded me tremendous freedom to pursue research topics that interested me and I have benefited greatly from his counsel in every area. I will forever cherish our wide-ranging conversations on science and philosophy and thank him deeply for his role in my personal development that had led me to where I am today. I would also like to thank Professor Amir Riaz who played an important role in advancing my computational fluid dynamics education during the final years of my PhD. He was patient with me as I learnt the techniques of the field and introduced me to interesting problems.

Members of the Advanced Manufacturing and Polymer Processing Lab have been of great support to me. In particular, I would like to thank Marcelo Arispe-Guzman and Connor Armstrong who helped me build a nice experiment that lasted six years. Together we developed as scientists and learned to do good experiments. I also thank Artiom Kostiouk and Margaret Lo who spent a summer generating lots of useful data for my research. Jiazhen Qiao and Bernard Chang from the Riaz group were always around to discuss interesting ideas and helped me setup numerical experiments.

I would also like to acknowledge the support from UMD's broader fluid dynamics community. In particular, the Calabrese, Duncan, and Kiger research groups have played a supporting role in my development as a member of the community. Derrick Ko was of great help early in my career and was patient with me as he shared his experimental expertise. I am indebted to Professor Howard Stone at Princeton who played a big role in my fluid dynamics education by introducing me to several new ideas, and inspired me to work on many problems in this dissertation. I learnt from him how to think about problems in fluid dynamics and I am grateful for his support. I also acknowledge the support from the University of Maryland supercomputing resources which I extensively used in my research.

The generous support from the Mechanical Engineering department allowed me to be financially stable through the years. Having been a teaching assistant throughout my tenure, I would like to thank Professor Gary Pertmer for his mentoring role in my development as a teacher.

My housemates and friends over the years have always been there for me when I needed them the most. I am particularly grateful to Alok Bharadwaj for his friendship.

Finally to my family, I say thank you. I am truly appreciative for your belief in me and the constant love and support through the years.

Table of Contents

List of Figures

Chapter 1: Introduction to the dissertation

This dissertation is a detailed study of extensional drop deformation and capillary-driven breakup at low Reynolds number. Many industrially relevant phenomena such as preparation of emulsions, dispersive and distributive mixing of liquid additives, and incorporating immiscible liquids into additive manufacturing applications involve deformation and breakup of drops. Extending our understanding of the dynamics behind such processes will be a useful scientific endeavor and will benefit many industries. In this regard, this dissertation revisits the classical problem to better understand it.

Extensional deformation of drops at low Reynolds number was formally studied first by G. I. Taylor [4] in a device called the four-roll mill. It is a testament to the usefulness and the simplicity of the device that many classical papers [1, 2, 5] over the decades have used the device to study drop deformation in stagnant extensional flows. Among them is a paper by Grace [5] which first published the so-called Grace curve – a widely used measure in mixing industries – to characterize the critical capillary number at different viscosity ratios. While extensional flows with a stagnation point find better use in labs, non-stagnant extensional flows are more common in industries than stagnation point extensional flows. Further, the

applicability of the grace curve has been questioned [6] under certain circumstances and in this dissertation, the problem is revisited using a new approach. Drop behavior in non-stagnant extensional flows are studied over a wide range of capillary numbers both above and below the critical capillary number. A unique channel design that can imposing a constant extension rate is introduced. Thus, the experiments in this dissertation are similar to the classical studies [1, 2, 5] but is easily translatable to an industrial setting.

Lubrication theory [7, 8] is used to understand the non-stagnant extensional flow in the channel. While single phase flows are typically studied using lubrication theory, experiments in this dissertation involve a drop deforming in the flow. Thus, it is important to fully understand the effect of the drop present in the flow and the implications of applying the theory. An objective of this dissertation is to apply the theory to predict some anomalous behavior of drops in different parts of the flow and compare drop velocity to the lubrication theory prediction.

Drop deformation at low Reynolds number is primarily caused by application of external viscous force. When the force is removed, the tendency of drops is to retract into a sphere or breakup into many drops. While the study of such transient behavior is a classical problem [1, 9] by itself, it fits into a general parametric space comprising of viscosity ratio and Reynolds number. Different parts of this space has received attention from researchers over the years [10, 11, 12, 13, 14, 15] who have all considered effects of viscosity ratio and inertia separately. In line with keeping this study relevant to industrial applications, another objective of this study is to explore behavior of slender drops in the new part of the parametric space.

The dissertation is organized into four independent studies. In chapter 2, the behavior of drops in a non-stagnant extensional flow is analyzed and a new non-dimensional measure is introduced. Chapter 3 is a verbatim reproduction of an article published in Physics of Fluids [16] and rationalizes a previously unobserved behavior of velocity lag in drops undergoing non-stagnant extension. In chapter 4, a model is developed based on lubrication theory and validated to predict drop deformation under shear-influenced deformation. Chapter 5 focuses on capillary-driven breakup of slender drops in a previously unexplored part of the parametric space. Finally, the appendix provides supplementary data from experiments and computations, and presents some non-trivial drop behavior in different domains.

Chapter 2: A new measure for drop deformation in extensional flows at low Reynolds number

2.1 Abstract

The critical capillary number of immiscible drops, which represents the state where the drop cannot be stable in a surrounding flow, is usually determined in low Reynolds number extensional flows by suspending them at the stagnation point of a four-roll mill device and subjecting them to different steady states. In this study, we subject drops to non-stagnant extensional flow in a converging channel and present a new measure – called the semi-minor capillary number – to describe the drop deformation process. The measure uses the instantaneous semi-minor dimension of the deforming drop as the length scale in calculating the capillary number. Our experiments at small initial capillary numbers, compared to the critical capillary number, yielded steady drops with a constant value of semi-minor capillary number. For large initial capillary numbers, the same constant represented an asymptotic limit of the self-similar deformation. The new measure of semi-minor capillary number thus helped rationalize drop behavior at both small and large initial capillary numbers. More importantly, it provided significance to drop behavior at large initial

capillary numbers which is a largely unstudied parametric space in the context of determining the critical capillary number. Finally, we present the critical semi-minor capillary number at different viscosity ratios and discuss its significance.

2.2 Introduction

Understanding and improving mixing of two immiscible liquids is of interest to a range of industries that manufacture food products [17, 18], cosmetics [19], paints [20], and even vaccines [21]. Studying the fundamental fluid dynamics problem behind immiscible fluid mixing – dispersion of a single drop of fluid into another – allows for process improvement at various scales that are of interest to these industries. In this chapter, we experimentally study the fundamental problem and unveil a new non-dimensional measure that predicts drop deformation in such systems.

Assuming both fluids are Newtonian and incompressible, the problem involves a drop of viscosity $\hat{\mu}$ and density $\hat{\rho}$ that is immiscible in a second fluid of viscosity μ and density ρ. The initial radius of the drop is assumed as a, and the interfacial tension between the fluids is assumed as σ. Making a low Reynolds number approximation for both the fluids, the motion is governed by the incompressible Stokes equation and continuity equation both inside and outside the drop. At the boundary of the drop, continuity of velocity and tangential stress between the two fluids is assumed. Due to the interfacial tension, the normal stress undergoes a jump across the interface and the shape of the drop can be described by the non-

dimensional boundary condition [8]

$$\lambda\hat{p} - p + [(\boldsymbol{\tau} - \lambda\hat{\boldsymbol{\tau}}) \cdot \boldsymbol{n}] \cdot \boldsymbol{n} = \frac{1}{Ca}(\boldsymbol{\nabla} \cdot \boldsymbol{n}). \tag{2.1}$$

Here, τ and $\hat{\tau}$ are the dimensionless stress tensors, and p and $\hat{p}$ are the dimensionless fluid pressures with capped variables corresponding to the fluid inside the drop. The ratio of viscosity of the two phases is λ $(= \hat{\mu}/\mu)$ and $\boldsymbol{n}$ is the normal vector to the interface directed outwards from the drop. Thus, $\boldsymbol{\nabla} \cdot \boldsymbol{n}$ is the curvature of the interface at the base of the normal vector. Ca is the capillary number – a dimensionless quantity – defined as the ratio of external viscous force on the drop to the interfacial force holding the shape together. The balance between the two forces dictates the shape of the drop in the flow. Capillary number is given by equation 2.2

$$Ca = \frac{\mu V}{\sigma}, \tag{2.2}$$

where V is a velocity scale of the external flow that causes motion of the drop. While the description of the problem is complete, the drop behavior in this system is non-trivial and many approaches have been used to study the problem [22, 23, 24]. Small deformation analyses [25, 26, 27, 28], slender body theories [29, 30, 31], and numerical methods [9, 32] all represent different attempts to uncover the fluid dynamics of deforming drops. Theoretical methods typically use known solutions of low Reynolds number flows to seek details about the flow. When detailed solutions provided by such theoretical methods are not needed, experimental methods [1,

2, 4, 5, 33] have provided useful insights. Visualizing flow fields within deforming drops [34, 35] helps understand the effect of external flow on drop motion. While such experiments are useful visualization exercises, a particular class of experiments [1, 2, 5, 33] aimed to classify drop behavior into stable and unstable regimes and were based on direct probing of equation 2.1.

From equation 2.1, it can be seen that only a small change in $\boldsymbol{\nabla \cdot n}$ is needed when the capillary number is small. This means that the deviation in shape of the drop from a sphere is small for small capillary numbers and is consistent with the fact that the interfacial tension force that resists deformation is high. The deviation of drop shape from sphericity also increases with increase in capillary number as per the same equation. This inspires an experiment where the capillary number can be systematically varied and the critical capillary number (Ca_{crit}) – where no stable shape can exist – can be discerned. Many experiments [1, 2, 5, 33] accomplished this is by subjecting the drop to increasing amounts of shear rate $\dot{\gamma}$, starting from a low value, in a linear flow and found the condition where the drop became unstable. The velocity scale in equation 2.2 was written as $a\dot{\gamma}$ making the capillary number

$$Ca = \frac{\mu a \dot{\gamma}}{\sigma}. \tag{2.3}$$

The experimental approach did not necessitate subjecting the drops to shear rate beyond the critical value since it was generally accepted that large capillary numbers always made the drop unstable. This unstable behavior of drops has been studied with a focus on breakup mechanisms after flow stoppage [36, 37], but without a

focus on the drop behavior during deformation. Since the regime of large capillary numbers was unexplored from the perspective of understanding transient drop deformation, we aimed to fill this gap in literature and sought a generalized mode of drop behavior over all capillary numbers – both above and below the critical capillary number. To accomplish this, we devised a new measure called the semi-minor capillary number (Ca_{sm}) defined as

$$Ca_{sm} = \frac{\mu b \dot{\gamma}}{\sigma}, \tag{2.4}$$

where b is the instantaneous semi-minor dimension at the center of mass location of a deforming drop. Thus, Ca_{sm} represents the ratio of external viscous force and the interfacial force on a drop of radius b. Since drop deformation at any capillary number is always characterized by a reduction in semi-minor dimension, Ca_{sm} can potentially capture drop behavior over all capillary numbers. To study the variation in Ca_{sm} at various capillary numbers, we subjected drops to steady extensional rates for a finite time in a non-stagnant extensional flow. These flows have been investigated before [38, 39, 40] but in channels that did not impose a steady extensional rate. Achieving a steady extensional rate was important to maintain consistency with the methods in literature [1, 2, 5, 33]. We thus designed a flow converging channel whose spanwise width reduced as inverse of the streamwise coordinate [41, 42, 43, 44] which rendered the extensional rate along the centerline of the channel near constant [7, 16]. A wide range of extensional rates were obtained by simply controlling the flow rate in the channel. We studied the variation of Ca_{sm}

of deforming drops in the flow and discovered the existence of a unique Ca_{sm} that fully captured drop behavior over all capillary numbers.

The chapter is organized as follows. In section 2.3 we describe the experimental setup, fluids used in the study, our experimental methods, and the data analysis technique. Next, in section 2.4 we analyse drop behavior at various capillary numbers and discuss them in three parts. First, we describe drop behavior in the channel at small capillary numbers which revealed the existence of a critical Ca_{sm}. This is followed by discussion of drop behavior at large initial capillary numbers where the critical Ca_{sm} represented an asymptotic limit. Finally, we use data from literature to plot and discuss the critical Ca_{sm} over different viscosity ratios. In the conclusions section, we assert that Ca_{sm} provides kinematic significance to the drop deformation phenomenon in the parametric space of large capillary numbers and discuss the significance of the metric in industrial applications.

2.3 Experiments

A 3D model of the flow channel used in this study is shown in figure 2.1. The channel had two bounding walls parallel to each other and the other two bounding walls slowly varying as $f(x)$ starting from the indicated origin. The fluid flow was streamwise along positive x direction.

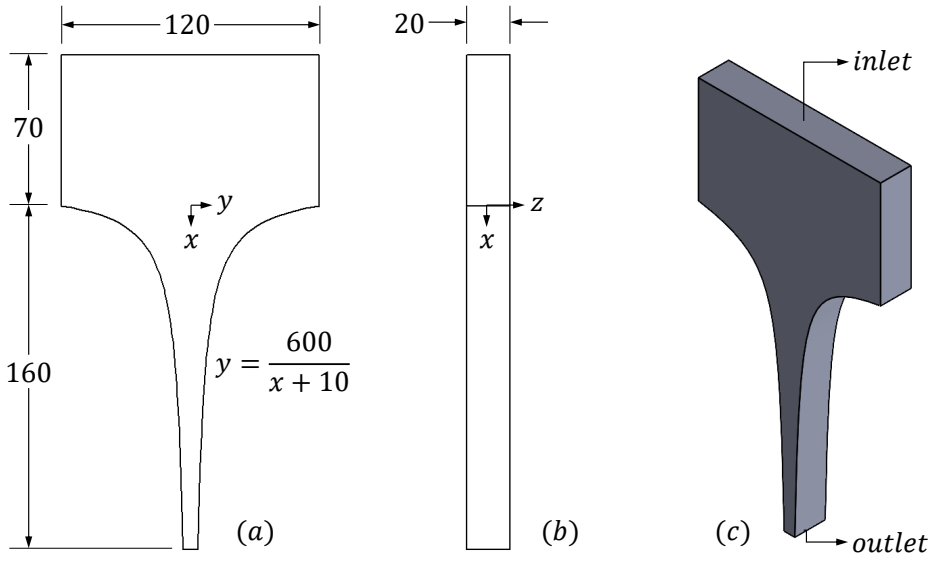

Figure 2.1: (a) Front view, (b) side view, and (c) isometric view of a planar channel with flow streamwise along x. All dimensions are in mm. The origin of the coordinate system is equidistant from the two planar bounding walls.

The channel was machined from a transparent block of acrylic and was supported using an aluminium frame. A reciprocating piston was used to push the bulk fluid through the channel, and a rack and pinion mechanism was used to control its motion. An Arduino was used to control the input voltage to the motor coupled with the pinion gear. This regulated the linear speed of the piston and allowed fluid flow rate control in the channel. From the outlet of the channel, a pipe channeled the liquid into a long column where static pressure of the liquid head ensured a steady state of the fluid in the flow channel. The experimental setup is shown in figure 2.2(a). The channel had an injection port, as seen in figure 2.2(a), that allowed for the injection of a single drop of an immiscible fluid using a syringe into the bulk flow. The injection port consisted of a resealable membrane which

ensured no fluid leaked out of the channel during the drop injection process.

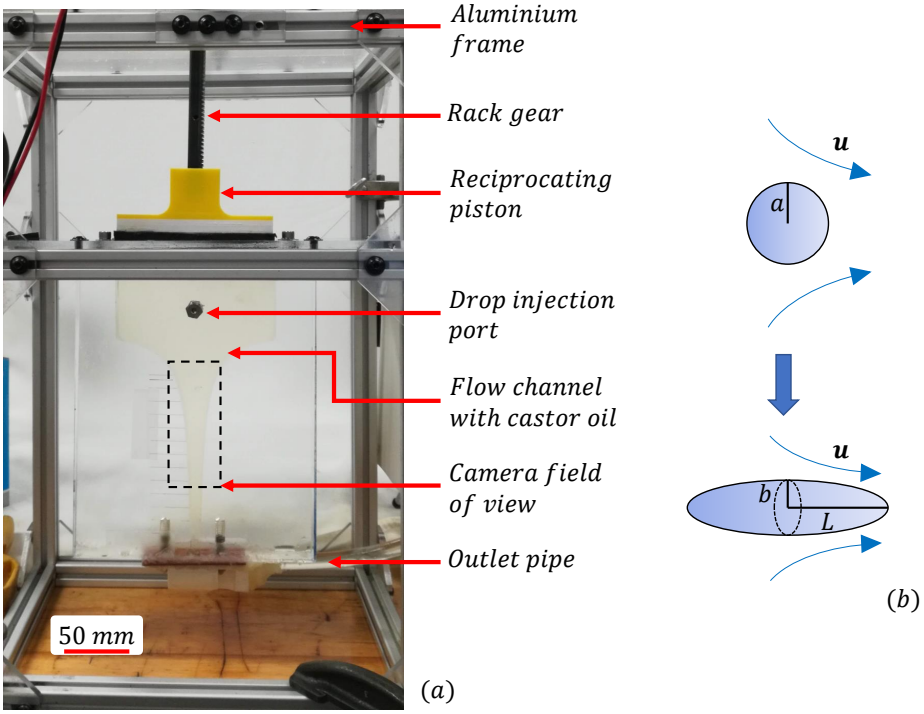

Figure 2.2: (a) The experimental setup showing the planar converging channel and the flow control mechanism. Flow rate of Castor oil is controlled through the motion of the reciprocating piston into the channel. (b) shows the schematic of an initially spherical drop undergoing deformation due to the external flow. L is the semi-major length of the deformed drop and b is the semi-minor length (also referred to as the width).

The fluids used in this study were Castor oil (procured from Bulk Apothecary) as the bulk fluid and Silicone oil (procured from MicroLubrol™) as the drop. The viscosity of Castor oil was $0.72\,\mathrm{kg\,m^{-1}\,s^{-1}}$ and density was $961\,\mathrm{kg\,m^{-3}}$. The viscosity of Silicone oil was $0.20\,\mathrm{kg\,m^{-1}\,s^{-1}}$ and density was $970\,\mathrm{kg\,m^{-3}}$. The viscosity ratio for the system was thus 0.28 and the interfacial tension between the two phases was approximately $0.004\,\mathrm{N\,m^{-1}}$. The main experiment involved studying the deformation of the Silicone oil drop in Castor oil flow through the channel.

After injecting the drop into the static Castor oil in the channel, the piston was slowly moved so that the drop appeared in the field of view of the camera. At this position, the piston motion was stopped, and the drop was allowed to stabilize into a sphere. For all experiments, the initial location of the drop was chosen as (30 mm, 0, 0) as per the coordinate system indicated in figure 2.1. The motion induced by the small difference in density between the two fluids was insignificant compared to the flow rate imposed and it allowed us to neglect any effect of gravity on the experiment. The Arduino was then programmed to supply a definite amount of voltage to the motor which set the flow rate in the channel. Using the initial radius of the drop and the extensional rate [16], the initial capillary number (Ca_i) of the drop was calculated using equation 2.3. A camera (Casio Exilim Pro EX-F1) was used to capture images of the drop as it translated and deformed in the flow field. Due to the symmetry of the channel geometry, the drop was restricted to flow along the centerline. Figure 2.2(b) shows a schematic of drop transition from initial state to a deformed state due to the influence of external flow.

Using different combinations of initial radius and flow rate in the channel, we imposed different capillary numbers on the drop. The initial radius of drops ranged from 1.0 mm to 2.2 mm. Reynolds number for all experiments, calculated using the drop radius and properties, never exceeded 1.00. For each experiment, the recorded images of drop deformation in the flow were analysed using a custom-built MATLAB program which extracted the end-to-end length of the drop and its width at the center of mass location. The half-width was used in equation to calculate Ca_{sm} for every transient drop shape. Note that $Ca_{sm} = Ca_i$ for the initial shape.

2.4 Results and Discussion

Central to our experimental methods was the ability of the flow to impose a near constant extensional rate along the drop trajectory. We confirmed this by evaluating the x component of velocity along the centerline of the channel using lubrication theory. The velocity was validated experimentally, and with numerical simulations [16]. Armed with the relationship between extensional rate and the flow rate of the single-phase flow, we injected drops into the flow and subjected them to various capillary numbers (Ca_i).

In this section, we first present drop behavior in two domains – below and above the critical capillary number – and show the significance of the new measure of Ca_{sm}. Then we use data from literature and present the critical Ca_{sm} at different viscosity ratios and discuss its significance.

2.4.1 Drop deformation at $Ca_i < Ca_{crit}$

The critical capillary number (Ca_{crit}) for pure extension of drops of viscosity ratio 0.28 is approximately 0.15 [2]. When the imposed Ca_i was less than Ca_{crit}, the viscous stress on the drop caused the drop to change its curvature at every point according to equation 2.1. Since the flow was associated with a pressure gradient in the streamwise direction, pressure outside the drop near its leading end in the flow was larger and caused the drop curvature at that point to increase. This in turn caused a reduction in width of the drop at its center of mass due to conservation of drop volume – resulting in a decrease in curvature at that point

in the xy plane. When the imposed capillary number was low, small changes in curvature were sufficient for the interfacial stress to fully balance the viscous stress imposed by the outside fluid and the drop attained a stable shape. We subjected the drop to many such steady states at $Ca_i < Ca_{crit}$. Figure 2.3 shows an experiment with $Ca_i = 0.12$.

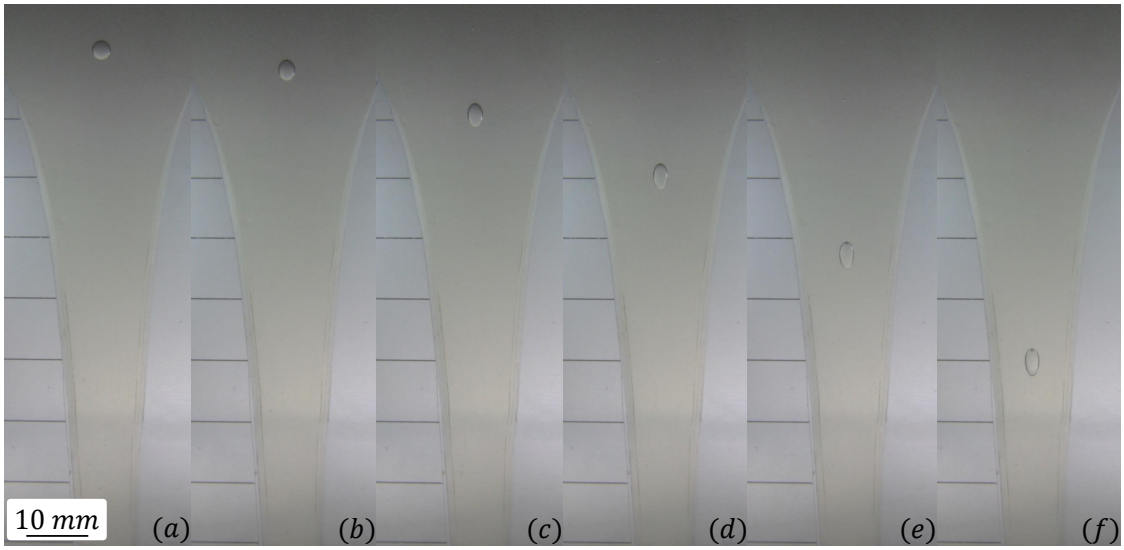

Figure 2.3: Drop deformation at $Ca_i = 0.12$. (a) is the initial state where the flow is initiated. (b) to (f) shows subsequent deformation. The drop deforms and quickly attains a steady prolate spheroidal shape.

After the flow onset, the drop transformation from a sphere to a prolate spheroidal shape was quantified by measuring the drop L/b, where L is the semi-major length and b is the semi-minor length of the spheroid. Attainment of steady states for other $Ca_i < Ca_{crit}$ in time is shown in figure 2.4. It can also be seen from figure 2.4 that around $Ca_i = 0.19$, L/b continuously increased in the flow consistent with the behavior slightly beyond the critical capillary number.

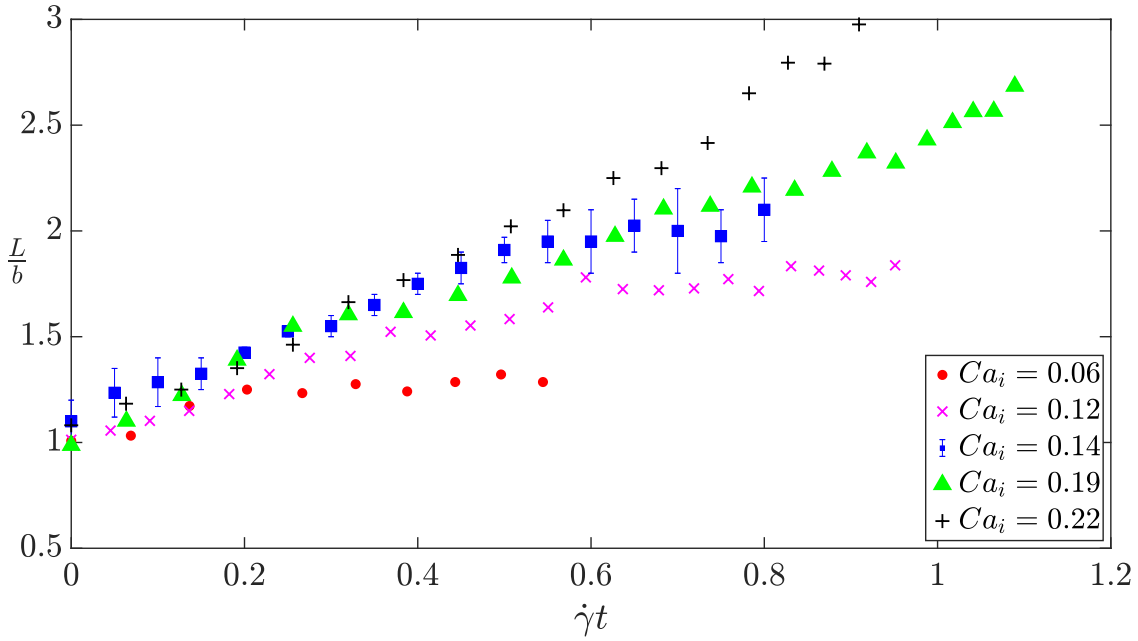

Figure 2.4: Drop deformation at various Ca_i versus $\dot{\gamma}t$ where $\dot{\gamma}$ is the extensional rate and t is time. Note the attainment of steady states for low Ca_i and the continuous deformation for $Ca_i > Ca_{crit}$. Sample error bar is shown for $Ca_i = 0.14$.

Since a prolate spheroid is associated with curvature along two planes at every location along its major axis, the decrease in width of the drop at the center of mass location had an unintended consequence. As the width reduced, the curvature in the yz plane – visualized in figure 2.2(b) using a dotted line on the deformed shape – increased and caused the pressure associated with interfacial tension to increase. This increase in pressure on the inside of the drop prevented further reduction in width. Thus, as the Ca_i increased, the degree of reduction in width reduced. A state was reached where further increase in extensional rate on the drop only caused a smaller decrease in width – compared to a larger reduction in width at lower Ca_i. Thus, the product of extensional rate and instantaneous semi-minor dimension was rendered constant for Ca_i larger than this critical value. This implied that the

capillary number associated with the semi-minor dimension (Ca_{sm}), as calculated from equation 2.4, was also constant for these cases.

The attainment of a constant value of Ca_{sm} for various steady states was better visualized by tracking Ca_{sm} for every Ca_i. Figure 2.5 shows other $Ca_i < Ca_{crit}$ where all drops attained steady shapes that corresponded to the same critical value of $Ca_{sm} \approx 0.11$. Note that each curve represents an experiment starting from an initial state of a spherical drop with $L/b = 1$ and ending at deformed shape where $L/b > 1$. Since $Ca_i < Ca_{crit}$ all yielded steady shapes, note that all data points become concurrent after a modest degree of drop deformation.

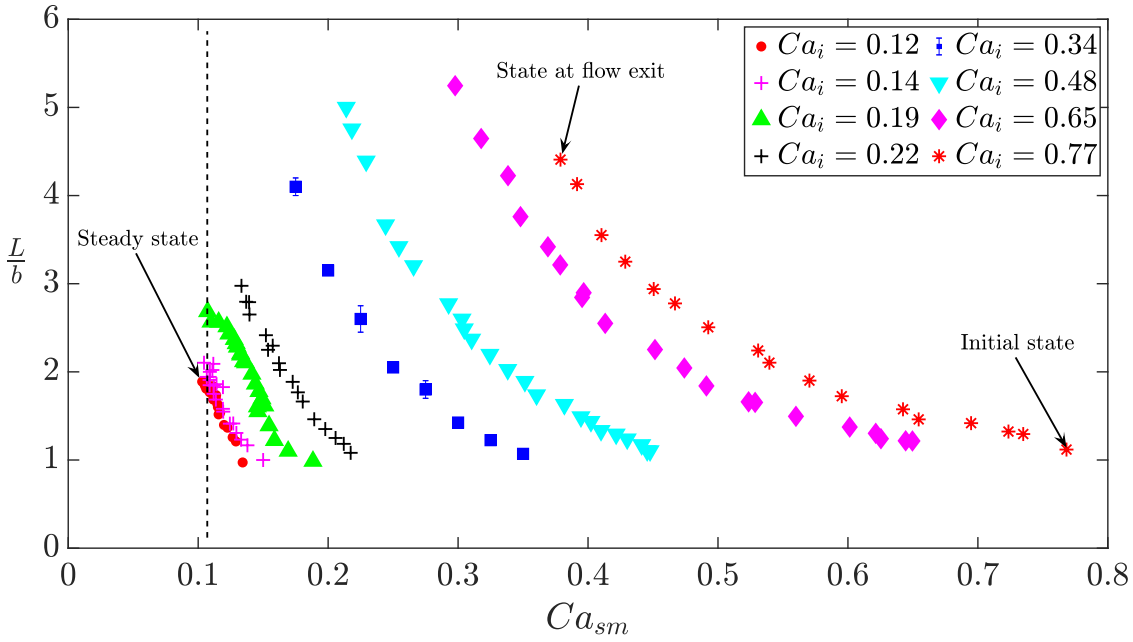

Figure 2.5: Tracking the L/b of deforming drops as a function of Ca_{sm}. Each curve represents a single experiment carried out at a fixed Ca_i. Drops start from an initial state of $L/b = 1$ where $Ca_i = Ca_{sm}$. Subsequent deformation is tracked till drops reached a steady state for $Ca_i < Ca_{crit}$, or till drops exit from the flow for $Ca_i > Ca_{crit}$. The vertical dashed line is the lower bound (and a unique value for a given viscosity ratio) of Ca_{sm} for all Ca_i. Sample error bar is shown for $Ca_i = 0.14$.

Further evidence for the existence of a constant Ca_{sm} at $Ca_i < Ca_{crit}$ was

found by analysis of data from [2]. In their comprehensive study of drop behavior at various initial capillary numbers, the critical capillary number was determined as the Ca_i state where a stable drop did not exist. However, their definition of Ca_i was based on a length scale equal to the initial radius of the spherical drop. From a volume conservation calculation, we determined the instantaneous width of the drop at every steady state and used it in equation 2.4 to calculate Ca_{sm}. Figure 2.6 shows a plot of Ca_{sm} versus Ca_i for three viscosity ratios from [2].

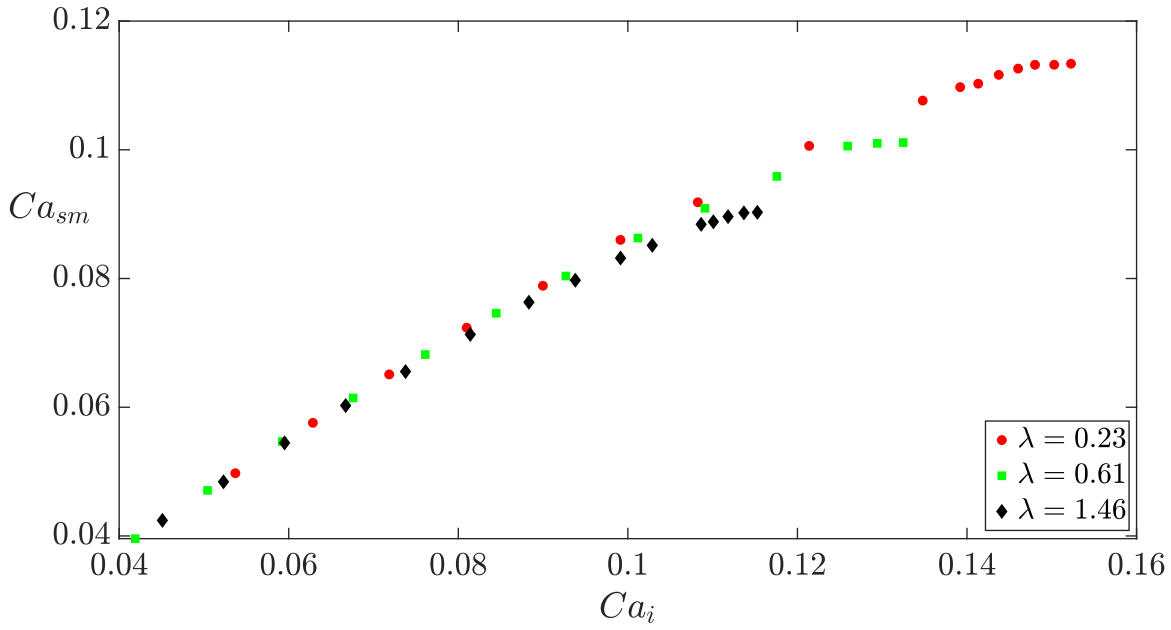

Figure 2.6: Data extracted from [2]. The plot shows Ca_{sm} at steady states calculated for various Ca_i. The three curves represent different viscosity ratios (λ). Note that as Ca_i is increased, Ca_{sm} becomes independent of Ca_i and is referred to as the critical Ca_{sm}. The largest Ca_i for each viscosity ratio is the Ca_{crit}.

For $Ca_i << Ca_{crit}$, note that the Ca_{sm} increases with increase in Ca_i. This is consistent with drop behavior at small degrees of deformation where the curvature in the yz plane is not sufficient to oppose further reduction in width. However, after a certain value of Ca_i was exceeded, further increase in Ca_i rendered Ca_{sm} constant

(a value we refer to as the critical Ca_{sm}) as evident from figure 2.6. We obtained a critical $Ca_{sm} = 0.11$ for our system with viscosity ratio of 0.28. Our next goal was to discern the role of critical Ca_{sm} when the imposed capillary number was large.

2.4.2 Drop deformation at $Ca_i > Ca_{crit}$

In this parametric space, the viscous stress on the drop was much larger than the interfacial stress that held the drop together. However, the dynamics of drop deformation explained in section 2.4.1 still applied. Drops at large Ca_i reduced in width by a large amount compared to their steady state counterparts at low Ca_i. As long as the drops were subject to flow in the channel, they continued to deform and attained long shapes. Figure 2.7 shows an experiment at $Ca_i = 0.60$ where the drop never stopped deforming in the flow.

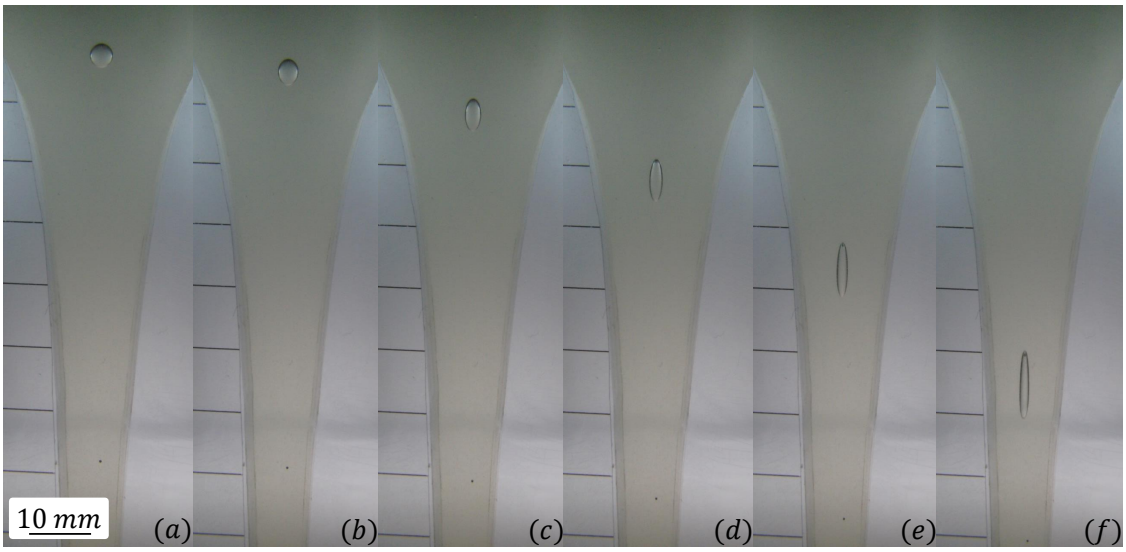

Figure 2.7: Drop deformation at $Ca_i = 0.60$. (a) is the initial state where the flow is initiated. (b) to (f) shows subsequent deformation. The drop deforms continuously in the flow and no steady state is observed.

As we subjected drops to many $Ca_i > Ca_{crit}$ and plotted the change in shape over time, we discovered a self-similar behavior. As seen in figure 2.8, every Ca_i followed the same trajectory for L/b vs $\dot{\gamma}t$ where $\dot{\gamma}$ is the extensional rate and t is time.

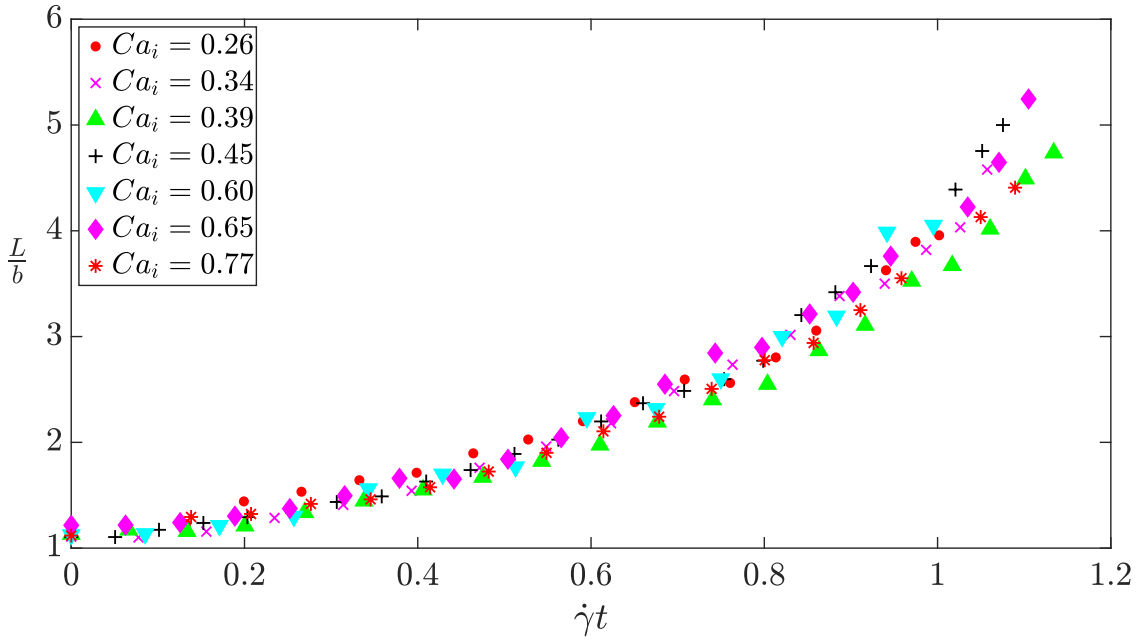

Figure 2.8: Self-similar behavior of drops at $Ca_i > Ca_{crit}$.

Since the drop deformation process at large Ca_i was self-similar, an upper bound for L/b existed regardless of $Ca_i > Ca_{crit}$. The reason for existence of an upper bound was due to the diminishing duration of time spent by the drop in the flow with increase in flow rate. Notwithstanding this, the self-similar curve in figure 2.8 uniquely characterized the drop behavior at large Ca_i.

Further, figure 2.9 shows that the behavior at large Ca_i nearly follows the transformation from a sphere to a prolate spheroid. In figure 2.9, $L/b \propto \tilde{b}^{-3}$ represents a volume conservation between a sphere and a prolate spheroid, and

$L/b \propto \tilde{b}^{-2}$ represents an area conservation between a circle and an ellipse. For similar L/b, the latter transformation causes larger reduction in width compared to the former. It can be seen that the deforming drop deviated from both the curves. The deviation from $L/b \propto \tilde{b}^{-3}$ observed for long shapes was due to the planar nature of the flow where the drop narrowed more in the xy plane than the xz plane. Since the semi-minor dimension was only tracked in the xy plane, the drop transition deviated from the $L/b \propto \tilde{b}^{-3}$ behavior in figure 2.9. Despite the larger reduction in xy dimension, the drop behavior was not consistent with $L/b \propto \tilde{b}^{-2}$ and the reason will be explained ahead.

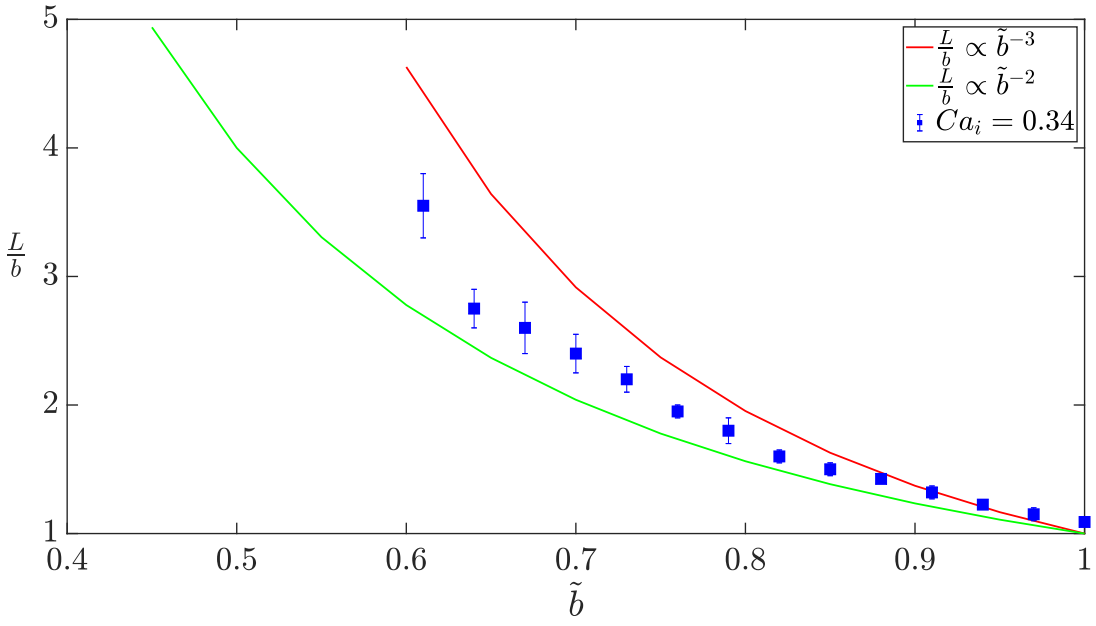

Figure 2.9: Kinematics of drop deformation from initial state ($L/b = 1$) to deformed state. $\tilde{b} = b/a$ where a is the initial radius of the drop.

We also tracked Ca_{sm} of deforming drops at $Ca_i > Ca_{crit}$ already shown in figure 2.5. Since the extensional rate on drops was large, the curvature at the leading end increased more than the case with $Ca_i < Ca_{crit}$. The semi-minor dimension

continued to reduce as $L/b \propto \tilde{b}^{-3}$ but the process suffered with an increase in yz curvature at the center of mass location. Increasing curvature prevented a large reduction in width ($L/b \propto \tilde{b}^{-2}$) and thus the drop shape transition did not remain consistent with the green solid line in figure 2.9. The larger slope of the experimental data in figure 2.9 compared with the $L/b \propto \tilde{b}^{-2}$ lead to the conclusion that the semi-minor dimension of the drop nearly stopped changing as the semi-major length of the drop continued to increase. This is possible for slender drops since a small reduction in width can cause a large increase in length. We extracted the cross-sectional profile of a deforming drop from the experimental data at $Ca_i = 0.44$ and is shown in figure 2.10. Note the attainment of a state towards the end where the semi-minor dimension $\tilde{b}$ at the center of mass location of the drop nearly stops changing while the semi-major dimension $\tilde{L}$ continues to increase.

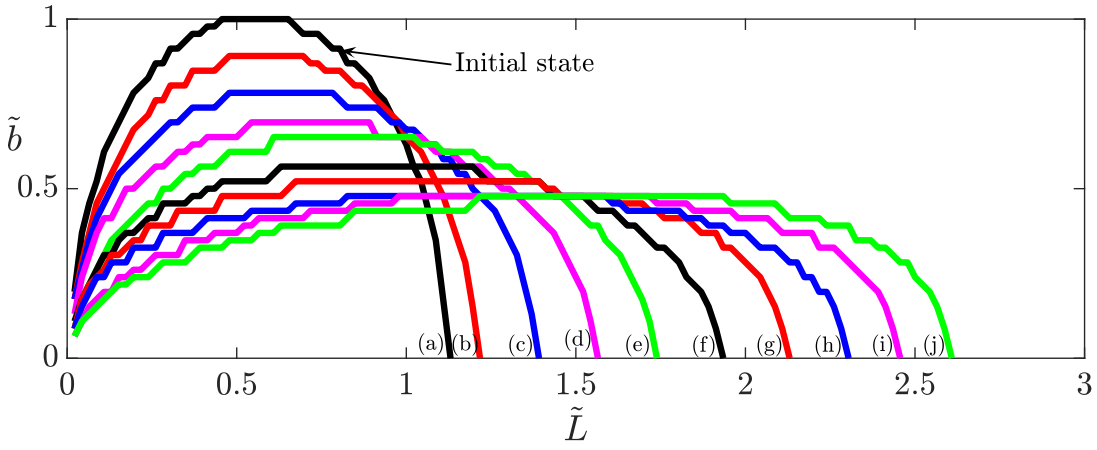

Figure 2.10: Instantaneous cross sections in the xy plane of a deforming drop at $Ca_i = 0.44$. $\tilde{b} = b/a$ and $\tilde{L} = L/a$ where a is the initial radius of the drop. (a) is the initial state and (b) to (j) shows the subsequent deformation in time. Note that $\tilde{b}$ at the center of mass location changes by a small amount with increasing deformation.

Despite the large deforming viscous forces on the drop, the semi-minor dimension cannot reduce to zero. Before this stage is reached, daughter drops pinch-off from the parent slender drop in a process called elongative end pinching, but the study is beyond the scope of this chapter. However, it was natural to expect a lower bound for Ca_{sm} based on the dynamics of drop deformation within the explored parametric space. From the discussion in section 2.4.1, the obvious choice for the lower bound was the critical Ca_{sm} as interpreted in that parametric space. If the drops spent longer time in the flow, the experimental data for all drops at $Ca_i > Ca_{crit}$ in figure 2.5 would asymptotically reach the critical Ca_{sm}.

2.4.3 Significance of semi-minor length b in extensional deformation of drops

All of the literature on extensional deformation of drops quantify the capillary number Ca_i using the initial radius of the drop (a) as the length scale. The theoretical basis for this is that both small deformation and slender body theories that predict drop deformation express critical parameters in terms of the initial radius. For example, in small deformation theory, the slight deviation from sphericity of the drop is expressed as a deviation from its initial radius a. Similarly, the slender body theory expresses the slenderness of a drop as L/a. Using a as a length scale is convenient because it is a truly independent parameter in the system that can be determined a priori. From an industrial application perspective, it is also convenient to quantify dispersion metrics in terms of a parameter – the initial capillary number – that can be established before commencing the mixing operation. However, Stegeman et al. [6] have pointed out certain issues with relying on the initial capillary number to predict drop sizes after the mixing process. In particular, the drop size after the mixing process at large capillary numbers were smaller than the prediction by the Grace curve. The Grace curve quantifies the critical capillary number Ca_{crit} based on initial radius and provides no information about the transient sizes of drops undergoing deformation.

Thus, there is a clear need to devise a new metric that considers the kinematics of drop deformation at any capillary number. As seen in previous sections, using the semi-minor length b of the drop accomplishes it. Calculating a capillary number

using b as the length scale revealed unique trends in behavior both above and below the critical capillary number.

2.4.4 Critical Ca_{sm} at different viscosity ratios

Since we established that deforming drops at any extensional rate had a lower bound for Ca_{sm}, it was of interest to plot the critical Ca_{sm} and compare it with Ca_{crit} that were obtained from other experiments [2, 5]. To accomplish this, we used data from [2] who studied drop behavior over a wide range of viscosity ratios (0.001 to 88.6). It was relatively easy to calculate the semi-minor dimension of the drop at the critical capillary number using a volume conservation calculation. Using the semi-minor dimension, we calculated the critical Ca_{sm} as per equation 2.4 and plotted it over different viscosity ratios in figure 2.11.

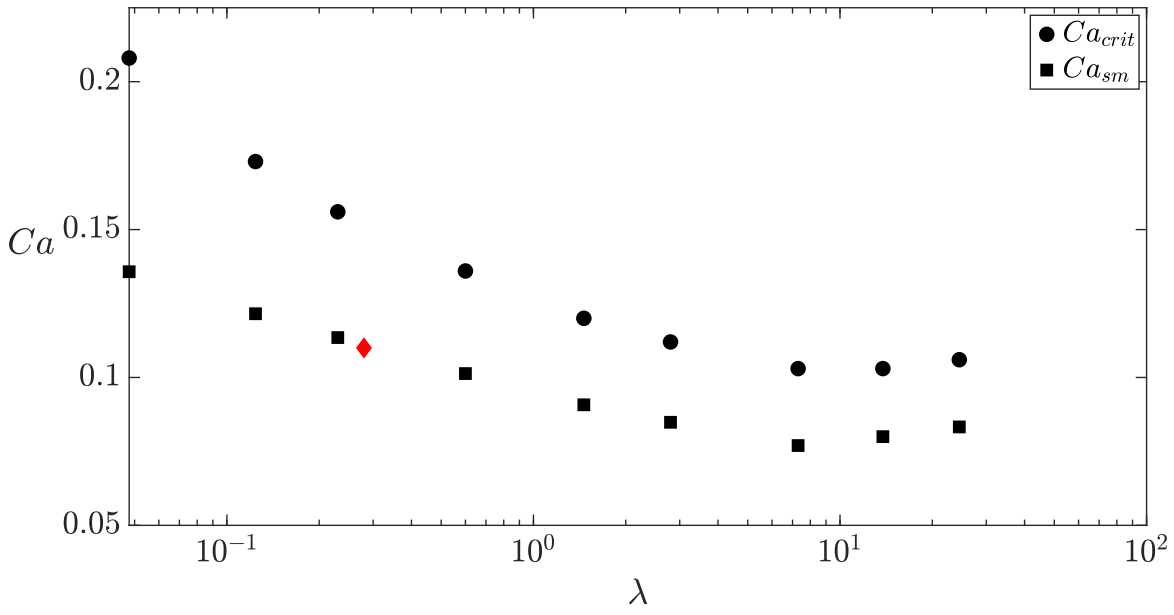

Figure 2.11: Ca_{crit} and critical Ca_{sm} at different viscosity ratios (λ) using data extracted from [2]. The red diamond represents critical Ca_{sm} obtained experimentally in this study for $\lambda = 0.28$.

The critical Ca_{sm} at every viscosity ratio is lower than the Ca_{crit}. This was expected because the Ca_{crit} used the radius of an undeformed drop a as the length scale while Ca_{sm} is based on the instantaneous semi-minor dimension b of a deforming drop. Thus, at a given viscosity ratio, critical $Ca_{sm} < Ca_{crit}$.

2.5 Conclusion

The aim of this work was to investigate drop deformation at small and large capillary numbers compared with the critical capillary number to find a universal metric that could characterize drop behavior in the entire parametric space of capillary number. While the critical capillary number is useful in classifying drop behavior into stable and unstable regimes, it does not provide any insight into drop dynamics at super critical capillary numbers. Our work addressed this by devising a new measure called the semi-minor capillary number. The measure took advantage of a universal drop behavior – exerting steady extensional strain on drops causes a monotonic reduction in their semi-minor dimension. We showed that drops at both small and large capillary numbers all attained the same critical value of semi-minor capillary number.

The flow channel used in the study was able to impose small and large extensional rates by simple flow control. The unique design imposed a near constant extensional rate on suspended drops. Such non-stagnant extensional flows produced in the channel are commonly used for extensional mixing of fluids in industries and figure 2.8, which shows the degree of drop deformation as a function of net

extensional strain, is useful data to design such mixers.

Finally, figure 2.11 which shows the critical semi-minor capillary number over several viscosity ratios is significant in many ways. While the critical capillary number curve – commonly referred to as the Grace curve – is useful to find the critical initial size of drops in a flow, it provides no information about the transient shapes that those deforming drops attain. Further, if a mixing process involves super critical capillary numbers, the Grace curve can only be used to estimate the daughter drop sizes *after* breakup of the slender thread. If estimates are needed for the minimum drop size attainable at *any* capillary number before breakup, the critical semi-minor capillary number curve is the only useful metric.

Chapter 3: Velocity of suspended fluid particles in a low Reynolds number converging flow

3.1 Abstract

We studied a pressure driven, low Reynolds number fluid flow through a planar channel whose spanwise width along the flow varied inversely as the streamwise coordinate, such that the extensional rate on the centerline was near constant. The effect of the near constant extensional rate on an immiscible droplet of Silicone oil was studied by tracking its deformation. The droplet rapidly deformed into an ellipsoid and displayed a consistent lag velocity compared to the single-phase background flow at the same point. The observations were attributed to flow induced deformation of the immiscible droplet which was a function of the magnitude of the initial Capillary number. The streamwise component of the single phase velocity along the centerline of the converging flow was also estimated to leading order using lubrication theory. The estimated velocity compared favorably with numerical simulations; and validation with experimental measurement of the flow of Castor oil through the channel by tracking tracer particles. The accuracy of the determination of the velocity field by the lubrication theory allowed for the

careful measurement of the velocity difference between the drop and suspended fluid velocities. This research validated lubrication theory predictions of flow velocity through a converging channel, and provided an experimental insight on behavior of a suspended phase.

3.2 Introduction

Fluid motion at low Reynolds number through channels with narrow geometries can be described by an approximation of the Navier Stokes equation, called the lubrication approximation. The lubrication approximation assumes a *narrow* channel gap where the distance along the direction transverse to the flow is much smaller than the characteristic distance along the flow direction [8]. The study of the effect of such flows - which is associated with large velocity gradients along certain directions - on a suspended phase is motivated by a unique application in polymer based additive manufacturing, where polymer flow through nozzles can be described by the lubrication approximation [45].

Narrow channels are ubiquitous in applications that utilize changes in geometry to manipulate fluid motion. These changes include the use of converging-diverging sections [44, 46, 47, 48], corrugated channel walls [49, 50], serpentine channels [51, 52, 53] and deformable channels [54, 55, 56]. Confined flows such as flow around a corner [57, 58] have been treated using asymptotic techniques and have revealed the existence of certain unique flow features that arise due to the geometry of the flow. The single phase flow of a fluid through a channel undergoing geometric

changes - like varying cross section - can usually be estimated using a known solution for a closely related simple geometry [59, 60, 61] or solved using lubrication theory [7, 62, 63]. The latter is a useful tool which uses asymptotic techniques and provides reliable results even at low orders of approximation. Lubrication theory has also been extended to higher orders of approximation [64], widening it's applicability to a larger class of single phase flows.

On the other hand, the study of multiphase confined flows is motivated by the ability of the bulk phase to affect the motion of the dispersed phase. Of particular interest is the case where the interface between the two phases is deformable. Examples include the motion of a deformable capsule in a corner flow [65], migration of particles towards walls of a deformable channel [66], and away from a flexible membrane suspended in the flow [67]. Particle motion in the vicinity of the walls of the channel can be studied using lubrication approximation [68] in the context of the varying gap between a wall and the curvature of the solid as it approaches the wall. Motion of solids with zero local curvature at the minimum gap to the wall has also been studied [69]. Related to the problem, another class of multiphase flows that is studied using lubrication theory is the transport of a densely filled solid system [70] where the approximation can be applied due to the narrow gap between the particles. However, when the particle concentration in the fluid is sparse, the motion of the particle is affected by one way coupling between the fluid and particle, and has been studied in converging-diverging flows [46]. Such flow channels can also impose velocity gradients which can be used to deform a suspended particle.

Unique, and controllable, velocity gradients can be engineered by designing

bounding walls of the channel based on requirement. For a symmetric, converging channel, an extensional rate can be imposed along the centerline in the streamwise direction which can lead to elongation of a suspended, deformable interface [38, 39]. Multiple studies [42, 43, 71, 72] have shown that the extensional rate can be near constant if the spanwise width varies inversely as the streamwise coordinate. The near constant extensional rate can be used to stretch a small but deformable particle suspended in it. Neglecting inertial effects at low Reynolds number, the degree of deformation of an immiscible droplet with radius a depends on the initial Capillary number (Ca) defined as

$$Ca = \frac{a\dot{\gamma}\mu}{\sigma} \tag{3.1}$$

where $\dot{\gamma}$ is the near constant extensional rate imposed by the outer fluid for a fixed flow rate, μ is the viscosity of the outer fluid, and σ is the interfacial tension between the two phases. The droplet is assumed to be of sufficiently small volume fraction so that it's behavior in the flow solely depends on the streamwise velocity gradient imposed by the bulk phase. For Capillary number below a critical value, the droplet attains a shape that is stable in the imposed velocity gradient. However, exceeding the critical Capillary number will cause the droplet to continuously elongate and lead to eventual breakup. Classical experiments [1, 4, 5] have characterized the critical Capillary number as a function of viscosity ratio in extensional flows.

The extensional rate imposed by the bulk phase can be studied using lubrication theory. An analysis by Lauga et al.[7] used lubrication theory to describe the low Reynolds number flow of a fluid through a narrow channel with rectangular

cross section where two bounding planes were parallel, and the other two bounding planes were slowly varying. They derived the equations for flow and showed that it is fully three dimensional even at leading order.

In the present work, we study a low Reynolds number flow through such a planar converging channel. The width of the channel varies as inverse of the streamwise distance which imposes a near constant extensional rate along the centerline. The lubrication approximation used by Lauga et al. [7] is used to predict the velocity field. We use numerical simulations of the low Reynolds number flow to validate the predictions of the lubrication theory. The velocity field is also measured experimentally by suspending a small solid particle in the flow which acts as a tracer to measure fluid velocity.

Conversely, when the size of the particle is larger, Faxen's law predicts a relative translational velocity between the particle and the single phase velocity at the same point. The relative velocity arises due to the force exerted by the bulk flow on the particle. In this study, we explore the effect of the viscous forces exerted by the flow on a deformable particle where we present experiments performed on the deformation of a single immiscible droplet suspended at the center of the channel. While the centerline of the flow is not associated with any transverse velocity due to geometrical symmetry, the existence of the constant streamwise velocity gradient - the constant extensional rate - will cause the droplet to stretch. These problems have applications in polymer based additive manufacturing [73] where the viscous flow of the polymer through narrow die geometries can be described by lubrication theory, and the effect of the flow on a suspended phase [74] needs to be understood.

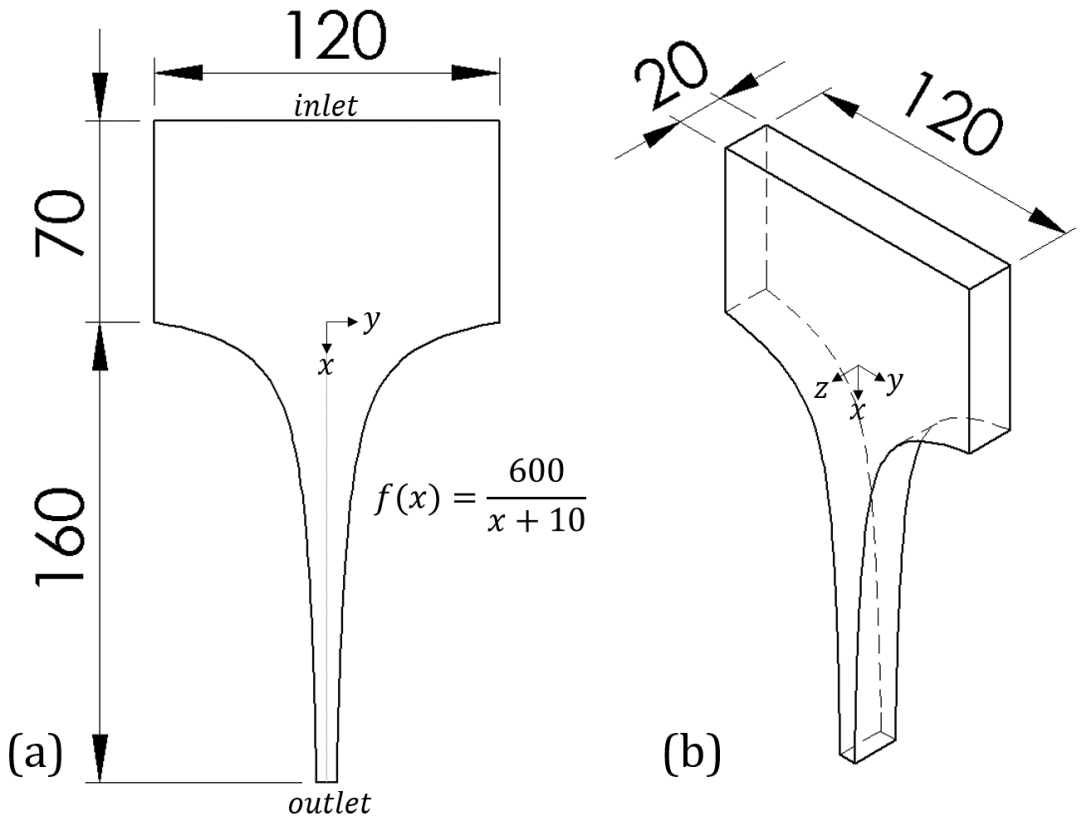

Figure 3.1: (a) Front view and (b) isometric view of a planar channel with flow streamwise along x. The spanwise width reduces inversely as the streamwise coordinate. All dimensions are in mm. The origin of the coordinate system is equidistant from the two planar bounding walls. Half-width of the channel at the outlet (where $x = 160\,\text{mm}$) is 3.53 mm. We use an axial length scale $\lambda = 160\,\text{mm}$, and a transverse length scale $h = 10\,\text{mm}$.

3.3 Lubrication analysis for a planar converging flow

We consider a pressure driven, low Reynolds number flow through a planar converging channel shown in Fig. 3.1. The flow is streamwise along x direction and the converging section has a wall profile based on the equation $f(x) = 600/(x+10)$. The channel is oriented with the streamwise direction along gravity.

Lauga et al. [7] posit the use of such planar channels, having streamwise

variations in cross sectional area, for mixing at low Reynolds numbers. Using lubrication theory, they showed that the velocity field is fully three-dimensional even at leading order which is advantageous for geometry induced mixing of species. We validate their analysis by studying a single phase flow in the channel shown in Fig. 3.1, and extend their study by investigating a two phase flow effect. As per the analysis of Lauga et al. [7], the governing equations of fluid flow are the incompressible stokes equation and mass conservation –

$$\nabla p = \mu \nabla^2 \mathbf{u}, \tag{3.2}$$

$$\nabla \cdot \mathbf{u} = 0. \tag{3.3}$$

In equations 3.2 and 3.3, p is the pressure, $\mathbf{u}$ is the velocity field, and μ is the viscosity of the fluid. If λ is an axial length scale and h is a transverse length scale, then $\epsilon = (h/\lambda) \ll 1$ means that dimension along transverse direction is much smaller than the dimension along the flow direction. This is a common assumption for lubrication theory to be applicable. Using these scales, the x, y and z lengths were non dimensionalized by Lauga et al. [7] as

$$(x, y, z) = (\lambda \tilde{x}, h\tilde{y}, h\tilde{z}). \tag{3.4}$$

Further, u and p, the velocity component along x and pressure respectively were non dimensionalized as

$$u = \frac{Q}{h^2}\tilde{u} \tag{3.5}$$

$$p = \frac{\lambda \mu Q}{h^4} \tilde{p} \tag{3.6}$$

where Q is the flow rate in the channel. Using the techniques of asymptotic analysis, Lauga et al. [7] solved for the leading order non dimensional u component of velocity as

$$\tilde{u}_0(\tilde{x}, \tilde{y}, \tilde{z}) = \frac{1}{2} \frac{d\tilde{p}_0}{d\tilde{x}} \left\{ (\tilde{z}^2 - 1) + \sum_{n \geq 0} \frac{4(-1)^n}{k_n^3} \frac{\cosh\left(k_n \tilde{y}\right)}{\cosh\left(k_n f(\tilde{x})\right)} \cos k_n \tilde{z} \right\}, \tag{3.7}$$

where $\tilde{p}_0$ is the leading order solution for the pressure and $k_n = (n + \frac{1}{2})\pi$. Further, the pressure gradient along the x direction was obtained as

$$\frac{d\tilde{p}_0}{d\tilde{x}} = \frac{3}{4f(\tilde{x})} \left\{ \frac{6}{f(\tilde{x})} \sum_{n \geq 0} \frac{\tanh\left(k_n f(\tilde{x})\right)}{k_n^5} - 1 \right\}^{-1}. \tag{3.8}$$

In this study, we focus on the centerline of the flow $(\tilde{y}, \tilde{z} = 0)$ in the flow channel shown in Fig. 3.1. The wall profile in terms of non dimensional variables was $f(\tilde{x}) = 6/(16\tilde{x} + 1)$. Substituting this in Equation 3.7, we get

$$\tilde{u}_0(\tilde{x}) = \frac{1}{2} \frac{d\tilde{p}_0}{d\tilde{x}} \left\{ -1 + \sum_{n \geq 0} \frac{4(-1)^n}{k_n^3} \frac{1}{\cosh k_n \frac{6}{16\tilde{x}+1}} \right\} \tag{3.9}$$

where $d\tilde{p}_0/d\tilde{x}$ is obtained by substituting $f(\tilde{x}) = 6/(16\tilde{x}+1)$ in equation 3.8. $d\tilde{p}_0/d\tilde{x}$ and $\tilde{u} = \tilde{u}_0(\tilde{x})$ were numerically truncated at $n = 50$ (same as Lauga et al. [7]). The solid line in Fig. 3.2 shows a plot of $\tilde{u}$ vs $\tilde{x}$ and the inset plot shows the variation of $\partial\tilde{u}/\partial\tilde{x}$ along $\tilde{x}$.

The plot indicates that the leading order streamwise component of velocity

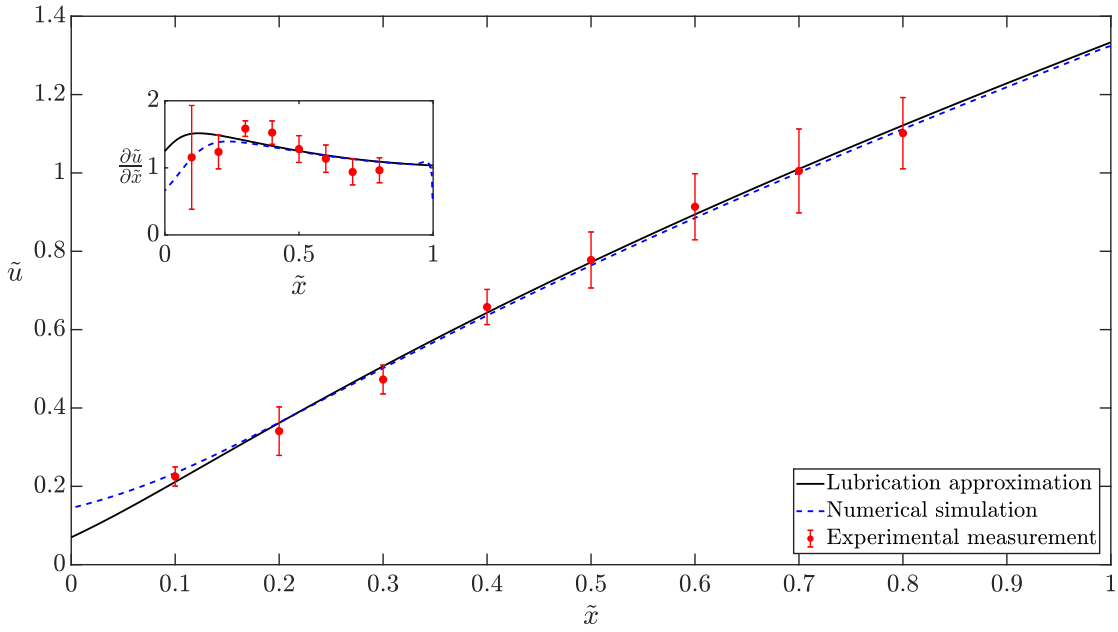

Figure 3.2: Non dimensional velocity ($\tilde{u} = u/(Q/h^2)$) vs. Non dimensional streamwise coordinate ($\tilde{x} = x/\lambda$) along the centerline of the flow obtained using lubrication approximation (solid line) and numerical simulation (dashed line). Error bars on experimental data represent standard deviation from the mean value. Inset graph plots the slope of the lubrication approximation and is equivalent to the variation of extensional rate.

increases approximately linearly in the flow along the centerline. This implies that the extensional rate (or $\partial\tilde{u}/\partial\tilde{x}$) is near constant. We used numerical simulations of the flow to find the velocity along the centerline, and experimentally measured it by using tracer particles in the flow.

3.3.1 Numerical simulations

Numerical simulations are commonly used to visualise and derive certain physical quantities associated with fluid flows. We first discretized the three dimensional geometry of flow using hexahedral elements. Appropriate boundary conditions were applied and the conservation of mass and momentum equations were solved using a numerical method. In this study, we used a commercially available software - ANSYS FLUENT - for the entire operation. The supplementary material details domain discretization, numerical scheme, and verification of results. A major theme of this study is to show the effect of the flow, which is initiated from rest, on a suspended fluid particle. Transient effects of such a flow can be neglected and our rationale is elaborated in the supplemental material. The dashed line in Fig. 3.2 shows the velocity obtained using numerical simulations and validates the flow velocity along the centerline obtained from the lubrication theory. A further level of validation is obtained by experimentally measuring the velocity along the centerline using tracer particles.

3.3.2 Experimental measurement of velocity

Fig. 3.3a shows the experimental setup with the flow channel and the linear actuator used for flow control. The flow channel was constructed using a transparent block of acrylic where the flow domain shown in Fig. 3.1 was machined. The channel was suspended using an Aluminum frame. A linear actuator, programmed to move at specific speeds, was used to impose specific flow rate of the bulk fluid. The bulk fluid used in this study was castor oil (Viscosity = $0.72\,\mathrm{kg\,m^{-1}\,s^{-1}}$, density = $961\,\mathrm{kg\,m^{-3}}$). At the outlet, a pipe was used to channel the flow into a tank maintained at the same height as the experimental apparatus. The static pressure head ensured that gravity did not cause unintended outflow from the flow channel.

A single Low Density Polyethylene (LDPE) pellet was suspended as a tracer particle into the flow of castor oil through the channel. Density of LDPE is approximately equal to castor oil and the particle was cylindrical shaped with an average diameter of 2 mm and length 3 mm. After carefully suspending the single particle at the center of the channel, the flow was initiated and a constant flow rate was imposed. Images of the particle in the flow were taken using a camera (Casio Exilim Pro EX-F1) at 30 frames per second to measure the translation velocity. The experiment was repeated for three different flow rates with constant inlet speeds of $2.4\,\mathrm{mm\,s^{-1}}$, $3.2\,\mathrm{mm\,s^{-1}}$, and $4.8\,\mathrm{mm\,s^{-1}}$. This translated to flow rates of $5760\,\mathrm{mm^3\,s^{-1}}$, $7680\,\mathrm{mm^3\,s^{-1}}$, and $11\,520\,\mathrm{mm^3\,s^{-1}}$ respectively. Fig. 3.2 shows the measured velocity of the tracer particle which approximated the background flow.

The validation exercise showed that lubrication theory could approximate the

flow in the channel along the centerline and the equations presented by Lauga et al.[7] could be used to gain further insights on velocity gradients. It is a useful tool to model the flow in the channel and resolve their designs. In the next section, we study the effect of such a flow on suspended immiscible droplets.

3.4 Effect of flow on suspended immiscible droplets

We injected a droplet of silicone oil (Viscosity = $0.2\,\mathrm{kg\,m^{-1}\,s^{-1}}$, Density = $970\,\mathrm{kg\,m^{-3}}$) with radius around 2 mm into castor oil (Viscosity ratio ≈ 0.28) using the droplet injection port. We then actuated the flow of castor oil and moved the droplet to the approximate location (30 mm, 0, 0) of channel shown in Fig. 3.1 and the flow actuation was stopped. At this initial location of the experiment, the droplet was allowed to relax into a sphere. Density difference between the two phases was small enough to assume no effect of gravity on the experiment and the interfacial tension was approximately $0.004\,\mathrm{N\,m^{-1}}$. Initial location of the droplet was chosen as (30 mm, 0, 0) to avoid subjecting the droplet to the initial spike in extensional rate seen in the inset plot of Fig. 3.2. The initial radius (a) was measured and the initial Capillary number was calculated using equation 3.1 before commencing the experiment. Reynolds number,

$$Re = \frac{\rho V a}{\mu}, \tag{3.10}$$

calculated with ρ = density of outer fluid ($961\,\mathrm{kg\,m^{-3}}$), μ = viscosity of outer fluid ($0.72\,\mathrm{kg\,m^{-1}\,s^{-1}}$), velocity scale V equal to the inlet velocity, and length scale a equal to initial radius of the droplet was around 0.04 to 0.16 over different experiments

and inlet speeds. At such low Reynolds number, the flow develops to the steady state value almost instantaneously. An experimental run consisted of subjecting the droplet to the flow at fixed flow rate. We only subjected the droplet to the flow from an initial location of $\tilde{x} \approx 0.20$ to $\tilde{x} \approx 0.60$ where the extensional rate was most steady, and avoided the variation near the inlet and the outlet of the channel. Images of the droplet in motion were captured at 10 frames per second for lower flow rates and 30 frames per second for higher flow rates. The Capillary number on the droplet was varied over different experimental runs by keeping the droplet size constant and varying the flow rate. However, for experiments at the largest Capillary number, we used slightly larger drop sizes due to experimental constraint of producing large flow rates. We varied the Capillary number from 0.12 to 0.77 to illuminate the effect of the initial Capillary number on droplet behavior. Fig. 3.3 shows two sets of experiments at initial Capillary number of 0.15 and 0.60.

The droplet with initial Capillary number of 0.15 in Fig. 3.3 deformed and quickly assumed a steady elongated shape and translated in the flow field. Capillary number of 0.15 is thus lower than the critical Capillary number which refers to condition of continuous deformation under the fixed extensional rate imposed by the outer fluid. For the viscosity ratio of the fluids we used, the critical Capillary number for extensional deformation of droplets is approximately 0.25 [1, 5]. However, the droplet behavior was different for large Capillary numbers. For an initial Capillary number of 0.60 the droplet continuously stretched in the imposed flow and this behavior is typical under conditions beyond the critical Capillary number. However, droplet breakup could not be observed since it quickly left the field of view. The

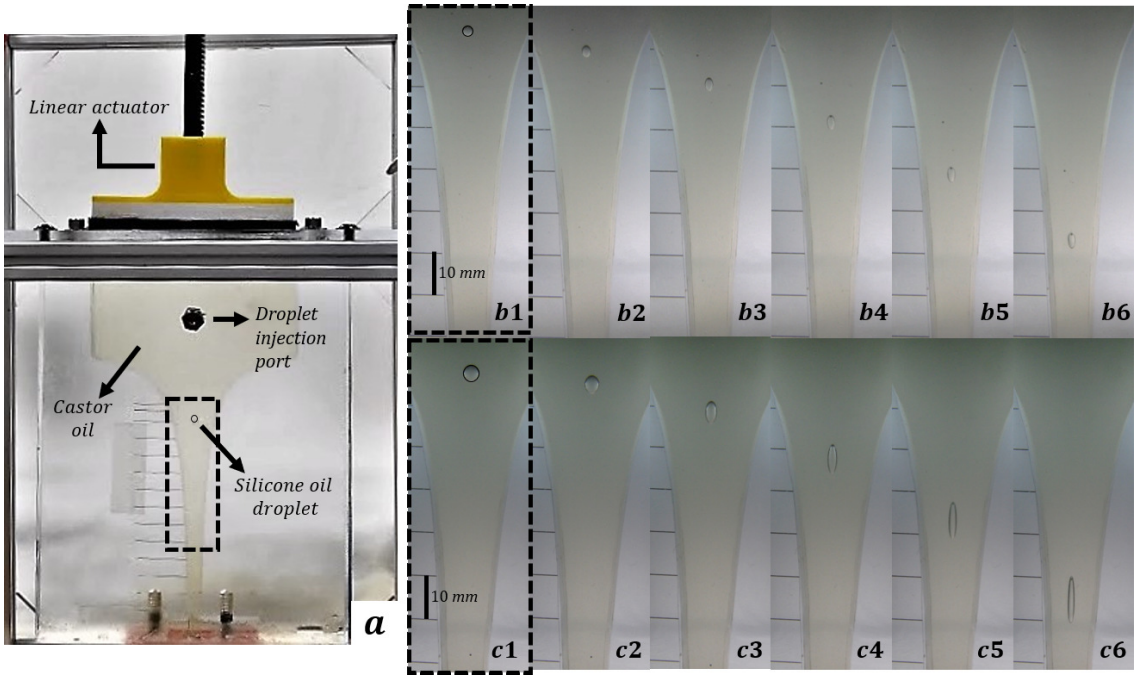

Figure 3.3: (a) The experimental apparatus to measure droplet deformation in the flow channel. Flow rate of Castor oil is controlled through the motion of the linear actuator into the channel along the downward direction. The motion of a Silicone oil droplet (highlighted black circle) in the region of interest (black dotted line) is captured using high speed photography. Viscosity ratio is around 0.28. Fig. b1 and c1 shows the initial state for Capillary number equal to 0.15 and 0.60 respectively. Fig. b2 to b6 and c2 to c6 shows the subsequent deformation induced by the motion.

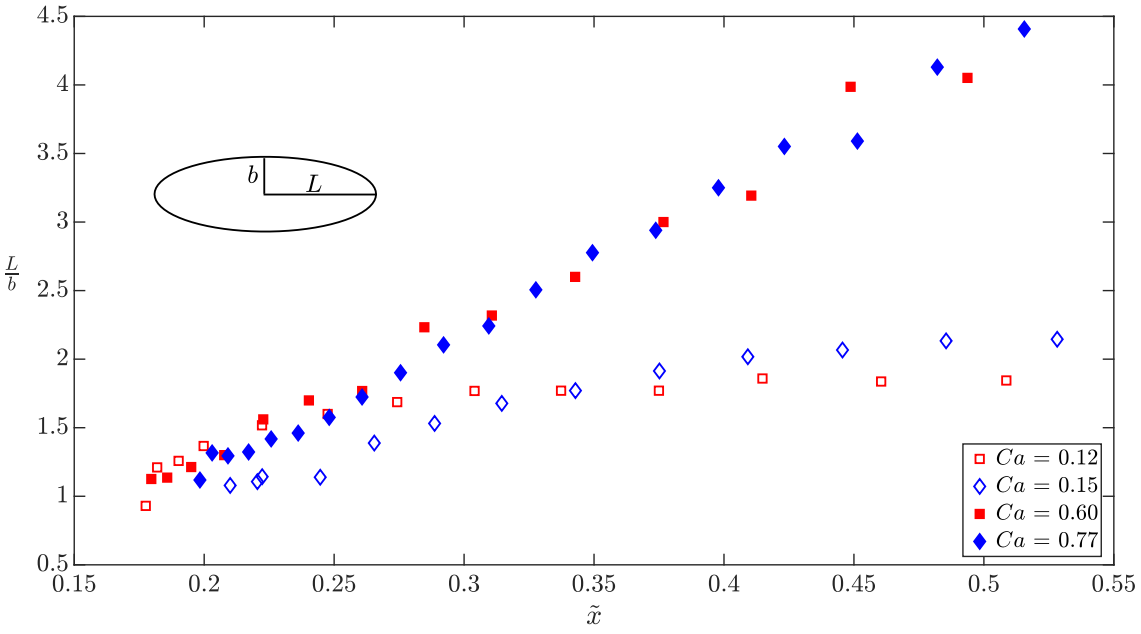

Figure 3.4: L/b vs $\tilde{x}$ for different initial Capillary numbers (Ca). The $\tilde{x}$ refers to the instantaneous center of mass location of the droplet. Note the attainment of a steady elongated shape for low initial Capillary numbers (hollow symbols) and continuous elongation for high initial Capillary numbers (solid symbols).

time spent by the droplet in the channel was inversely proportional to the inlet flow rate. Fig. 3.4 shows the change in L/b, where L is the half length (major axis) and b is the half width (minor axis) of the ellipsoidal droplet, for four different initial Capillary numbers.

We also measured the velocity of the droplet by tracking the center of mass. Fig. 3.5 shows the velocity of droplets at different initial Capillary numbers compared with the lubrication approximation of the single phase background flow. For the smaller values of initial Capillary number ($Ca = 0.12$ and $Ca = 0.15$), due to the small particle size and negligible deformation, droplets closely tracked the background flow at their steady state. However, every droplet lagged the background flow with the magnitude of lag increasing with initial Capillary number.

We explain this observation as a consequence of flow induced deformation which causes a deforming object to lag the background flow.

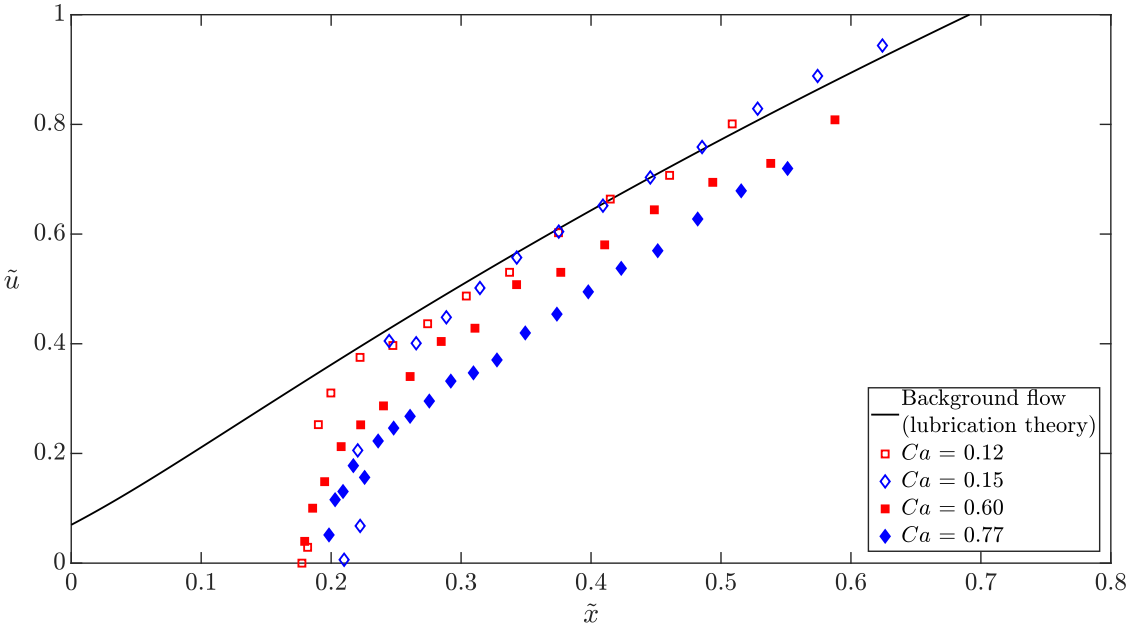

Figure 3.5: Comparison of droplet translational velocity and the background flow velocity. Ca refers to initial Capillary number and $\tilde{x}$ refers to the instantaneous center of mass location of the droplet. Note the large initial slope for low initial Capillary numbers (hollow symbols) compared with the high initial Capillary numbers (solid symbols).

When the flow was initiated, the extent of droplet deformation was a function of the initial Capillary number relative to the critical Capillary number. In the case of small initial Capillary number ($Ca = 0.12$ and $Ca = 0.15$) the droplet deformed quickly to a steady-state shape that was consistent with the balance between viscous and interfacial effects. The viscous stress on the droplet was the product of the viscosity of the external fluid and the extensional rate imposed by it, and was an $O(0.1)$ quantity. However, the interfacial stress that held the shape together was the ratio of interfacial tension and the initial size of the drop and was an $O(1)$

quantity. Droplets at low initial Capillary numbers thus reached a steady state since the viscous stress from the outside fluid could not overcome the interfacial stress. However, in the case of a large initial Capillary number ($Ca = 0.60$ and $Ca = 0.77$), where the external viscous stress was much greater than the interfacial stress, the minor axis of the droplet (b) continuously reduced until it reached $O(b_{crit})$, where b_{crit} is the droplet radius associated with the critical Capillary number at that flow rate. At this point, the minor axis of the droplet asymptotically stopped reducing and the primary change in dimension of the droplet from this point onwards was mostly the elongation of the major axis (L). L/b continued to thus increase without any bound.

In all the cases, as seen in Fig. 3.5, the droplets experienced both a change in shape and velocity. In the case of small initial Capillary number ($Ca = 0.12$ and $Ca = 0.15$) which is lower than the critical Capillary number, the droplet assumed a slightly deformed ellipsoidal steady shape. The droplets initially demonstrated a rapid increase in velocity $\tilde{u}$ with minimal translation $\tilde{x}$. Since the velocity of the droplet was determined by the location of the center of the droplet, much of the change of velocity was related to the change of shape. The change of shape is minimal and the droplet quickly achieved a steady-state. The droplet then closely lagged the background fluid velocity by assuming a slightly deformed ellipsoidal steady shape. This effect can be seen more profoundly for a slightly larger initial Capillary number of 0.17 which is still lower than the critical Capillary number. Fig. 3.6 shows droplet behavior at $Ca = 0.17$ and shows the correlation of steady state attainment with reduction in the magnitude of lag - which is defined as the

difference between the background flow velocity and the droplet velocity.

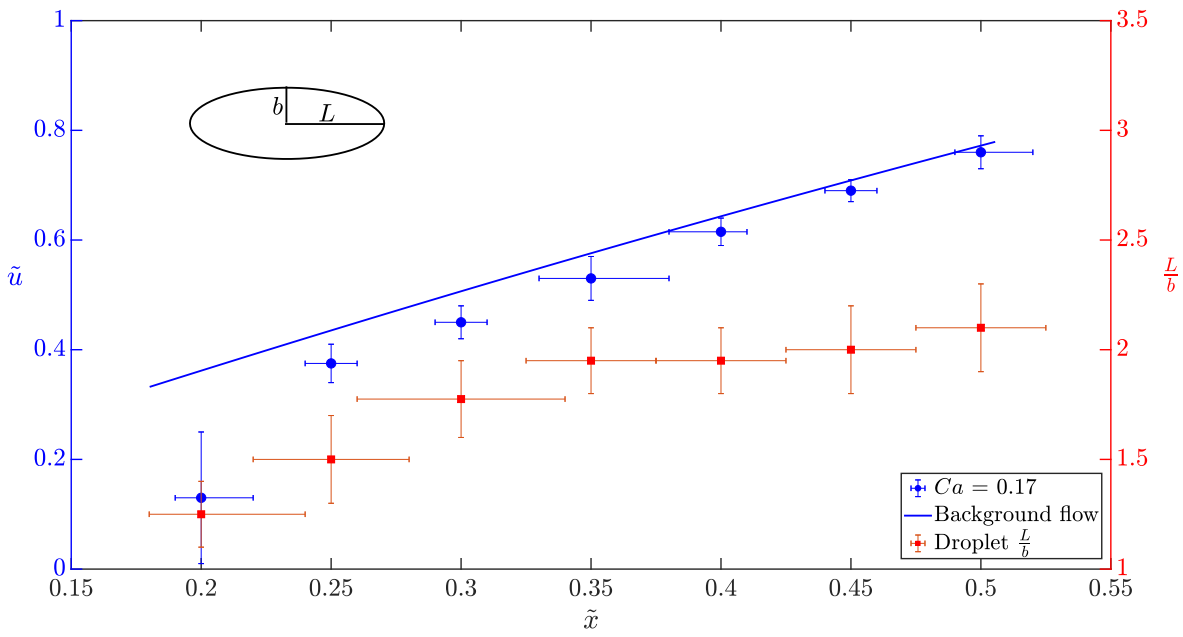

Figure 3.6: Motion induced deformation of droplet at initial Capillary number of 0.17. Crosses represent variation of L/b and circles represent variation of $\tilde{u}$. Solid line is the lubrication approximation of velocity of the single phase background flow. The droplet attains a steady shape at $\tilde{x} \approx 0.3$. The $\tilde{x}$ refers to instantaneous center of mass location of the droplet.

The droplet behavior beyond the critical Capillary number was similar but required more interpretation. When the initial Capillary number was larger than the critical Capillary number, the droplets were subjected to higher viscous forces creating an affine stretching where the drop deformed from a sphere to an ellipsoid and then to a cylinder. Droplet behavior at a large initial Capillary number of $Ca = 0.67$ is shown in Fig. 3.7. As evident from the plot, the droplet continued to deform with the minor axis (b) asymptotically reducing, while the length (L) continued to grow - causing L/b to increase. Since the largest change in shape occurred initially, the droplet took longer to achieve the background flow velocity

and the region of rapid increase in velocity with small translation along $\tilde{x}$ was extended. This caused the magnitude of lag to be higher than for droplets at low initial Capillary numbers. Furthermore, Fig. 3.7 shows that the lag magnitude was greater initially and slowly reduced as the droplet progressively reduced in width.

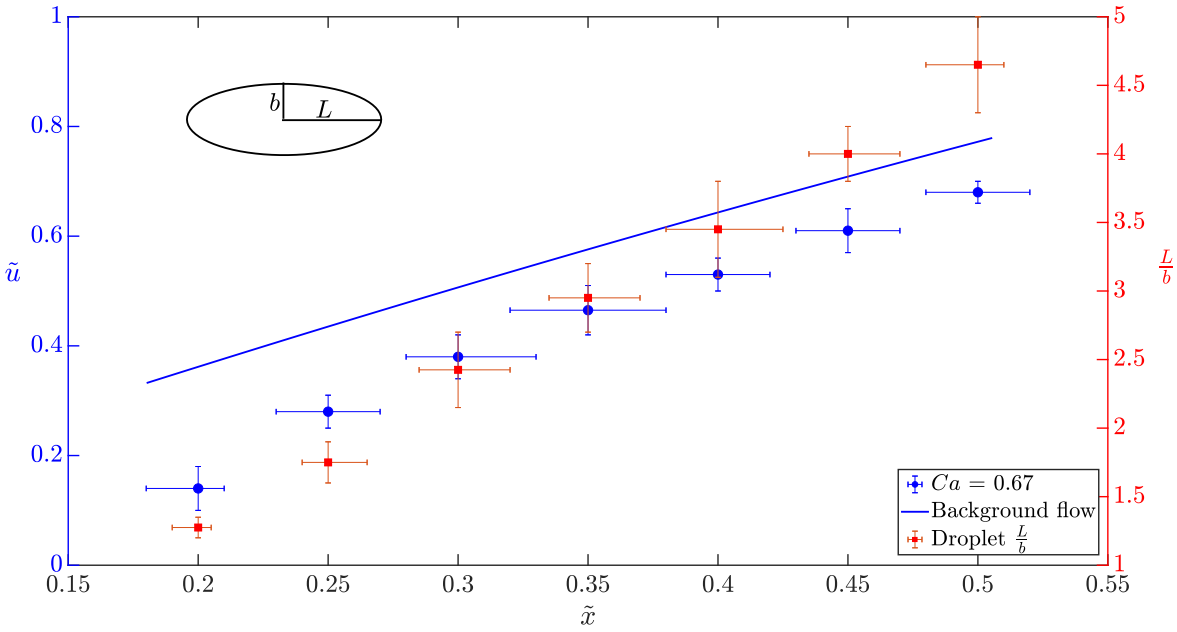

Figure 3.7: Motion induced deformation of droplet at initial Capillary number of 0.67. Squares represent variation of L/b and circles represent variation of $\tilde{u}$. Solid line is the lubrication approximation of velocity of the single phase background flow. The droplet continuously deforms in the domain with asymptotic reduction in b after reaching b_{crit}. The $\tilde{x}$ refers to instantaneous center of mass location of the droplet.

3.5 Conclusion

We used the lubrication approximation of the velocity field to compute a low Reynolds number flow through a converging channel. The leading order lubrication approximation of the velocity was found to agree to a high degree with numerical simulation and experimental measurement of the flow. The linear variation of the

streamwise velocity along the flow rendered the extensional rate near constant along the centerline. The flow channel can thus be used in applications where a constant extensional rate is desired in a low Reynolds number flow.

When immiscible fluid particles were suspended in the flow, we observed a lag in velocity of the particles compared to the single phase velocity at the same point. The occurrence of a relative translational velocity is consistent with the behavior of a particle suspended in an unconfined flow undergoing motion far from it. We report two distinct domains for lag velocity based on initial Capillary number. First, for Capillary number smaller than the critical Capillary number, the lag velocity rapidly approached a near constant value and closely lagged the background flow. This is due to the rapid approach to a steady-state shape balancing the external viscous and interfacial tension forces. Second, for Capillary number much greater than the critical Capillary number, where the droplet undergoes a large change of shape from a sphere to an ellipsoid for a longer time. The subsequent asymptotic lag velocity was greater in the second domain than the first. The magnitude of lag increased with the initial Capillary number and this non-intuitive behavior of droplets in low Reynolds number confined flows is a consequence of the finite size of the particles and the deformation induced by the flow.

Our study can be extended by using the lubrication approximation of the flow to predict the velocity gradients along the transverse direction to the flow. When a droplet is suspended offset of the centerline and flow initiated, it experiences transverse velocity gradients and undergoes shear deformation. Lubrication theory can help predict the behavior of droplets at these locations. We envision an

application of our study in Polymer Based Additive Manufacturing (PBAM) which routinely involve low Reynolds number flows through narrow nozzles. A new development in this area is the introduction of an immiscible fluid into the bulk flow which deforms the introduced phase due to viscous effects. Controlling the geometry of the channel and the flow rate provides a means to control the size and shape of the immiscible fluid as it is deposited on the build plate of the PBAM machine. Unique parts can thus be printed which have a predetermined distribution of a second immiscible phase in the bulk polymer.

Chapter 4: Modelling shear-influenced deformation of drops in a converging channel using lubrication theory

4.1 Abstract

Low Reynolds number flow through planar converging channels imposes pure extensional strain on suspended particles along the centerline of the flow. However, when the particles are near the wall, the no-slip condition for the velocity imposes an additional shear component to the total strain. If the suspended particles are deformable – like drops – their shape and size can be tuned by simply controlling the flow rate. In this study we apply concepts from lubrication theory and kinematics of mixing to describe the behavior of drops undergoing shear-influenced deformation. We theoretically model the motion of a drop suspended in the lubrication flow and predict its deformation by considering its initial location and time spent in the flow. We present a space-time phase space that predicts all possible particle trajectories and the procedure to calculate the drop deformation from the phase space. We then experimentally validate the model by tracking the deformation of suspended Silicone oil drops in a flow of Castor oil through a converging channel. Our model accurately predicts the net drop deformation for different combinations of initial

drop locations and time spent in the flow by the drop. We believe that our model can be conveniently used to calculate drop deformation in flows where the single phase flow solution is available.

4.2 Introduction

Confined flows are ubiquitous in applications across several length scales – ranging from water pipes of a household plumbing system to the blood vessels of a human circulatory system. While some confined flows have inertial effects, many applications in microfluidics [75, 76], polymer processing [45], and 3D printing [77] involve flows where all inertial effects can be neglected. In each of these applications, the absence of a free surface results in a unique flow profile due to the no-slip boundary condition at the walls. The profile is parabolic with streamwise velocity maximum at the center of the flow and zero at the walls – resulting in a spanwise velocity gradient. These gradients are constant in steady flows in channels with non-varying walls. However, the presence of slowly-varying walls leads to varying degree of these gradients along the flow. These velocity gradients can be harnessed to deform suspended particles – like drops [78, 79] – enabling new applications in the aforementioned areas. For example, suspending immiscible drops in a polymer flow allows for 3D printing of unique geometries with a controllable distribution of drop sizes within the printed geometry [80]. In this chapter, we show how to model the deformation of such a suspended drop in a low Reynolds number converging flow and validate the model using experiments.

Lubrication theory is a useful tool to study low Reynolds number flows through narrow channels [8, 81, 82]. The theory takes advantage of the presence of a small parameter in the flow geometry – usually the spanwise depth of the channel compared with the overall streamwise length – and uses it to perturb the Stokes equations of motion. The resulting series solution of the flow is accurate even at low orders of approximation. A previous study [7] used the technique to solve for the flow in a planar channel with slowly varying walls. Due to manufacturing constraints associated with axisymmetric channels, planar channels are ubiquitous in low Reynolds number microfluidic flows that can be fabricated in a single lithographic step. While single phase microfluidic flows have many well-established applications in biotechnology, multiphase microfluidic flows is an emerging research area. For example, some studies have explored the use of microfluidic channels as flow focusing devices for a suspended fluid. The geometry of the channel – which is typically narrow and has a rectangular cross section – enables passive control over the process. While scaling analysis [23, 83] has been broadly used to relate the flow rate through the channel and the morphology of the suspended phase, there have been no attempts to use detailed solutions of the flow in channels to predict their effect on the suspended drops [84].

When the solution for a flow is available, it is relatively easy to predict the trajectories of particles suspended in the flow. Applying equations of mixing kinematics allows for Lagrangian tracking of such particles in a steady state velocity field [85]. In this context, substituting solutions from lubrication theory into trajectory predicting equations of the theory of mixing should allow for determining

the behavior of suspended particles in the flow. To demonstrate the intended application of lubrication theory, we study a low Reynolds number flow through a planar converging channel shown in Figure 4.1.

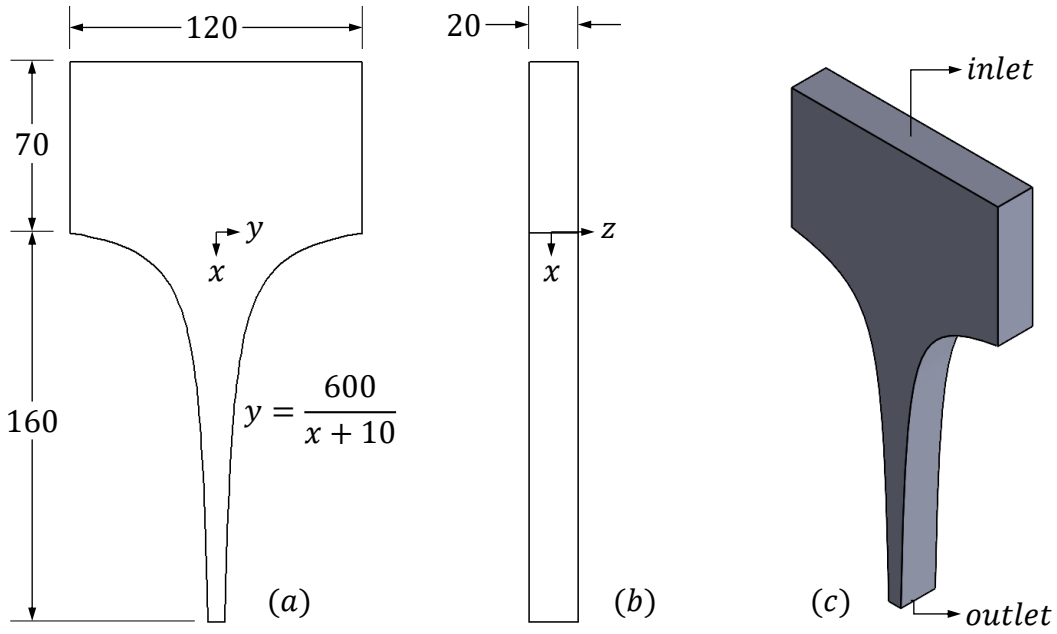

Figure 4.1: (*a*) Front view, (*b*) side view, and (*c*) isometric view of a planar channel with flow streamwise along x. All dimensions are in mm. The origin of the coordinate system is equidistant from the two planar bounding walls.

The channel has a fixed depth of 20 mm and the converging portion has a length of 160 mm. The converging portion of the channel has a wall profile based on a hyperbolic equation which renders the extensional rate of the single phase low Reynolds number flow near constant along the centerline. A previous study [16] used lubrication theory to study the flow along the centerline while this study will focus on locations near the wall that are shear-influenced.

This chapter is organized as follows. In section 4.3 we present the theoretical model, including assumptions, that predicts drop deformation in the flow. In section

4.4 we present the experiments performed to validate the model. In section 4.5, we present our results in two parts. First we present a phase space that depicts trajectories of particles in space-time. Then we illustrate how the phase space can be used to determine drop deformation in the flow and present model validation results. Finally, we provide some potential applications of our results.

4.3 Theoretical model

We consider an isothermal, Newtonian, and low Reynolds number flow of a fluid with viscosity μ_o and density ρ_o through the channel shown in Figure 4.1. Following the steps outlined in the previous study by Lauga et al. [7] to find the single-phase flow solution, we non-dimensionalize all variables using the following equations. Note that all capped variables are non-dimensional.

$$(x, y, z) = (\lambda\tilde{x}, h\tilde{y}, h\tilde{z}). \tag{4.1}$$

$$u = \frac{Q}{h^2}\tilde{u} \tag{4.2}$$

$$p = \frac{\lambda\mu_o Q}{h^4}\tilde{p} \tag{4.3}$$

In equation 4.1, $\lambda = 160\,\text{mm}$, $h = 10\,\text{mm}$, u is the x component of velocity, Q is the flow rate, and p is the pressure. Following Lauga et al. [7], we find the leading order solution for the x component of the velocity as

$$\tilde{u}_0(\tilde{x},\tilde{y},\tilde{z}) = \frac{1}{2}\frac{d\tilde{p}_0}{d\tilde{x}}\left\{(\tilde{z}^2-1) + \sum_{n\geq 0}\frac{4(-1)^n}{k_n^3}\frac{\cosh\left(k_n\tilde{y}\right)}{\cosh\left(k_n f(\tilde{x})\right)}\cos k_n\tilde{z}\right\}, \tag{4.4}$$

where $\tilde{p}_0$ is the leading order solution for the pressure and $k_n = (n+\frac{1}{2})\pi$. The wall profile is $f(\tilde{x}) = 6/(16\tilde{x}+1)$. The axial pressure gradient is given by

$$\frac{d\tilde{p}_0}{d\tilde{x}} = \frac{3}{4f(\tilde{x})}\left\{\frac{6}{f(\tilde{x})}\sum_{n\geq 0}\frac{\tanh\left(k_n f(\tilde{x})\right)}{k_n^5} - 1\right\}^{-1}. \tag{4.5}$$

A single drop of a second fluid with viscosity μ_i and density ρ_i is injected into the flow at $(\tilde{y}=0, \tilde{z}=(\tilde{z}_1+\tilde{z}_2)/2)$. The initial configuration and the subsequent deformation of the drop induced by the flow is depicted in Figure 4.2.

Initially, the spherical drop is located at $\tilde{x}_0$ and is bound between $\tilde{z}_1$ and $\tilde{z}_1$. Due to the motion of the surrounding fluid as indicated in equation 4.4, the drop undergoes shear-induced deformation. By implementing a simple Lagrangian tracking of two points on the drop, we can track the deformation in time. From the theory of mixing kinematics, a target point tracks the flow field in which it is suspended and its trajectory is governed by the equation

$$\frac{d\mathbf{x}}{dt} = \mathbf{v}(\mathbf{x},t), \tag{4.6}$$

where $\mathbf{v}(\mathbf{x},t)$ is the Eulerian velocity field. The particle path is given by the solution of equation with $\mathbf{x}=\mathbf{X}$ at $t=0$. We assume that the y and z components of velocity is zero and any point in the flow moves only along the x direction. Equation

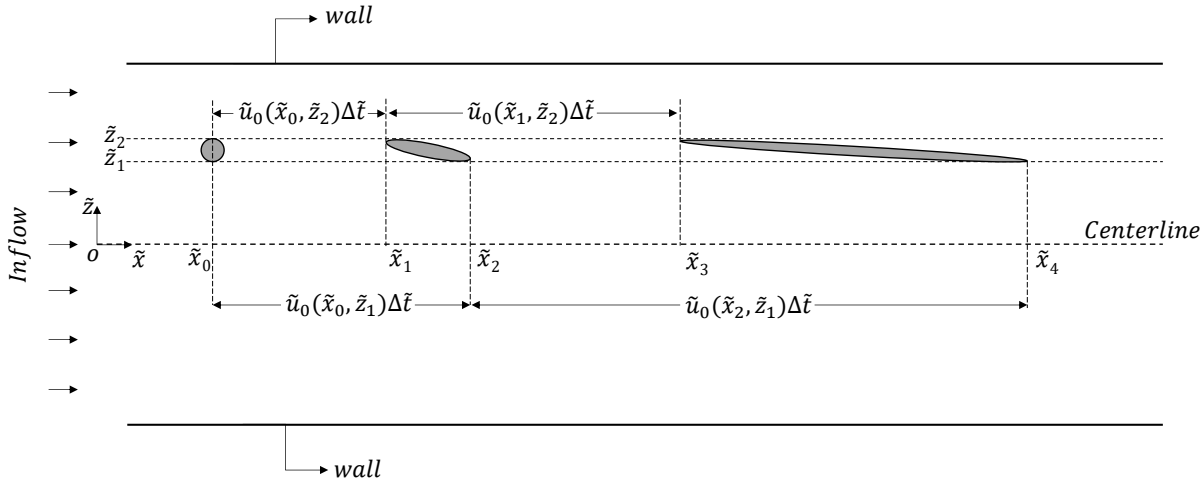

Figure 4.2: Side view of channel (as shown in Figure 4.1(b)) shown with a drop initially suspended at $(\tilde{x} = \tilde{x}_0, \tilde{y} = 0, \tilde{z} = (\tilde{z}_1 + \tilde{z}_2)/2)$. When the flow is actuated, the drop undergoes shear-influenced deformation but is restricted between $\tilde{z}_1$ and $\tilde{z}_1$.

4.6 becomes

$$\frac{dx}{dt} = u(x,t) \tag{4.7}$$

We convert equation 4.7 to non-dimensional form using equation 4.2 for velocity and $\lambda = 160\,\text{mm}$ as the length scale and obtain

$$\frac{d\tilde{x}}{d\tilde{t}} = \tilde{u}\frac{QT}{Lh^2}, \tag{4.8}$$

where $\tilde{t}$ is the dimensionless time and T is the time scale. Since a length scale and velocity scale was already defined in equations 4.1 and 4.2, we assume their ratio as the time scale T. Thus, $T = Lh^2/Q$ and we integrate equation 4.8 from 0 to $\tilde{t}_f$ where $\tilde{t}_f$ is the dimensionless time spent by the particle in the flow. The equation that predicts the particle trajectory is thus given by

$$\tilde{x} = \int_0^{\tilde{t}_f} \tilde{u} d\tilde{t} \tag{4.9}$$

We are now in a position to apply this concept to study the behavior of a suspended drop in the flow. In a small time interval Δt, the point $(\tilde{x}_0, \tilde{z}_2)$ translates a distance equal to $\tilde{u_0}(\tilde{x}_0, \tilde{z}_2)\Delta t$ and reaches $(\tilde{x}_1, \tilde{z}_2)$. The point $(\tilde{x}_0, \tilde{z}_1)$ translates a distance equal to $\tilde{u_0}(\tilde{x}_0, \tilde{z}_1)\Delta t$ and reaches $(\tilde{x}_2, \tilde{z}_1)$. Since $\tilde{z}_2$ is closer to the wall of the channel, $\tilde{u_0}(\tilde{x}_0, \tilde{z}_2)$ is smaller than $\tilde{u_0}(\tilde{x}_0, \tilde{z}_1)$. This causes the drop to shear and it elongates to attain a length equal to $|\tilde{x}_1 - \tilde{x}_2|$ as seen in the xy plane. The process continues in time and the drop becomes longer. Flow history seen by the

two points is important to take into account while integrating equation 4.9. This is because the drop is moving through a gradient in the x component of velocity.

Finally, we make the following assumptions for the model.

1. The flow is low Reynolds number and thus develops near-instantaneously to the steady state everywhere as indicated in equation 4.4. This allows us to ignore any transients in the flow as it develops to the form shown in equation 4.4.

2. The imposed capillary number on the drop – which compares the magnitude of external viscous force and the interfacial force – at the flow onset is ~ 10. The magnitude of viscous force on the drop increases further along the flow. Large capillary numbers allow us to ignore the effect of the interfacial force which resists deformation.

3. Related to the previous point, when drops exhibit large deformation the difference in viscosity between the drop and the surrounding can be neglected. This is an important assumption since viscosity ratio does indeed affect the behavior of suspended drops at low capillary numbers. Since we test the model at large capillary numbers, the drop is expected to track the flow in equation 4.4.

4. A previous analysis by Lauga et al. [7] showed that there is a z component of velocity in the flow which has the tendency to migrate the drop towards the centerline. However, we ignore the z velocity component and assume that the

drop is restricted to flow between $\tilde{z}_1$ and $\tilde{z}_1$. Since the drop is always along $\tilde{y} = 0$, the y component of velocity is also zero.

To illustrate an example of the predictive power of equation 4.9, we numerically solve equation 4.9 for $\tilde{t}_f = 1$. We discretize total time $\tilde{t}_f$ into 100 steps and offset $\tilde{z}$ into 50 units. We then implement a simple time marching scheme and obtain $\tilde{x}$ of all points in the flow at every time interval. This generates a space-time phase space of trajectories of all points offset of the centerline ($\tilde{z} = 0$ to $\tilde{z} = 1$) and will be discussed in section 4.5.

4.4 Experiments

To test the model, we injected a drop of Silicone oil (viscosity $= 0.35\,\mathrm{kg\,m^{-1}\,s^{-1}}$ and density $= 970\,\mathrm{kg\,m^{-3}}$) into the flow of Castor oil (viscosity $= 0.72\,\mathrm{kg\,m^{-1}\,s^{-1}}$ and density $= 961\,\mathrm{kg\,m^{-3}}$) through the channel. The initial volume of the drop was $50\,\mu\mathrm{L}$ and the flow rate was approximately $4600\,\mathrm{mm^3 s^{-1}}$. The slight difference in density did not affect the experiment since the imposed flow rate was much larger than the motion due to gravity effect. A previous study [16] has provided a detailed description of the apparatus and experimental procedure. Images of the flow were taken at 6 frames per second and Figure 4.3 shows the motion and deformation of the drop in the flow injected at $\tilde{z} = 0.5$.

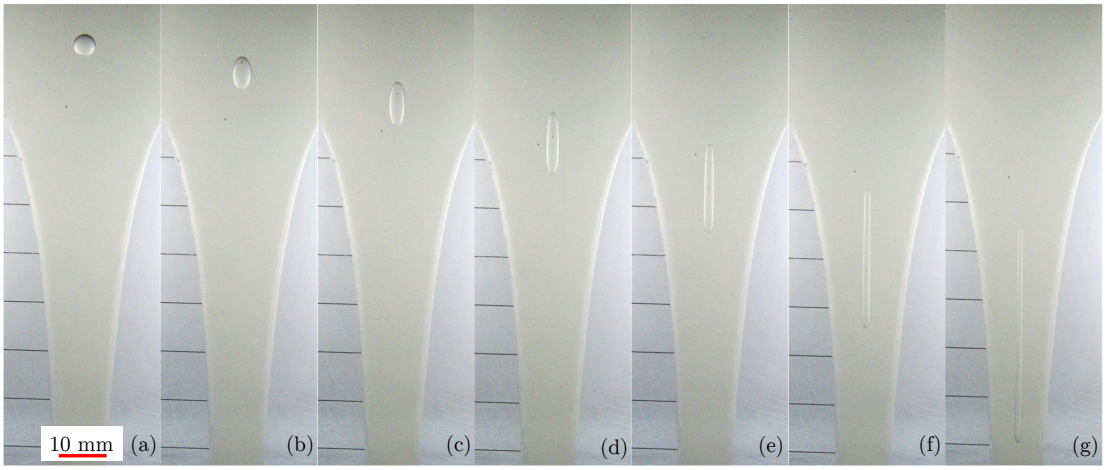

Figure 4.3: Shear-influenced deformation of a Silicone oil drop in Castor oil flow. (a) shows the initial configuration at rest where the diameter of the drop is approximately 4.5 mm and the drop is located at $\tilde{z} = 0.5$. (b) to (g) show the subsequent motion induced deformation. See Figure 4.2 for a kinematic description of the drop behavior from the side view. In (g) the drop has attained a length of approximately 44 mm. Experiment was repeated for different $\tilde{z}$ initial drop locations.

Initially, the drop and the background fluid were at rest as shown in figure (a). After flow actuation, the drop underwent shear-induced deformation and the photography was stopped before the leading end of the drop exited the field of view of the camera. We measured the final length of the drop length at this position. To validate our theoretical model, we performed three separate experiments at the same flow rate by injecting drops at $\tilde{z} = 0.4, 0.5, 0.6$. We did this to illustrate the effect of increasing shear on the drop with increasing offset distance $\tilde{z}$ from the centerline. For every experiment, the final drop length attained was measured and compared with the prediction from the model.

4.5 Results and discussion

4.5.1 Spatial-temporal phase space

Substituting equation 4.4 in 4.9 and integrating for $\tilde{t} = 1$, we obtain a phase space for $\tilde{x}$ as a function of $\tilde{z}$ and $\tilde{t}$. The phase space is a representation of the Lagrangian tracking of points seeded in the flow at $\tilde{x} = 0$. Figure 4.4 shows the space where $\tilde{z} = 0$ is the centerline of the flow and $\tilde{z} = 1$ is the wall of the channel.

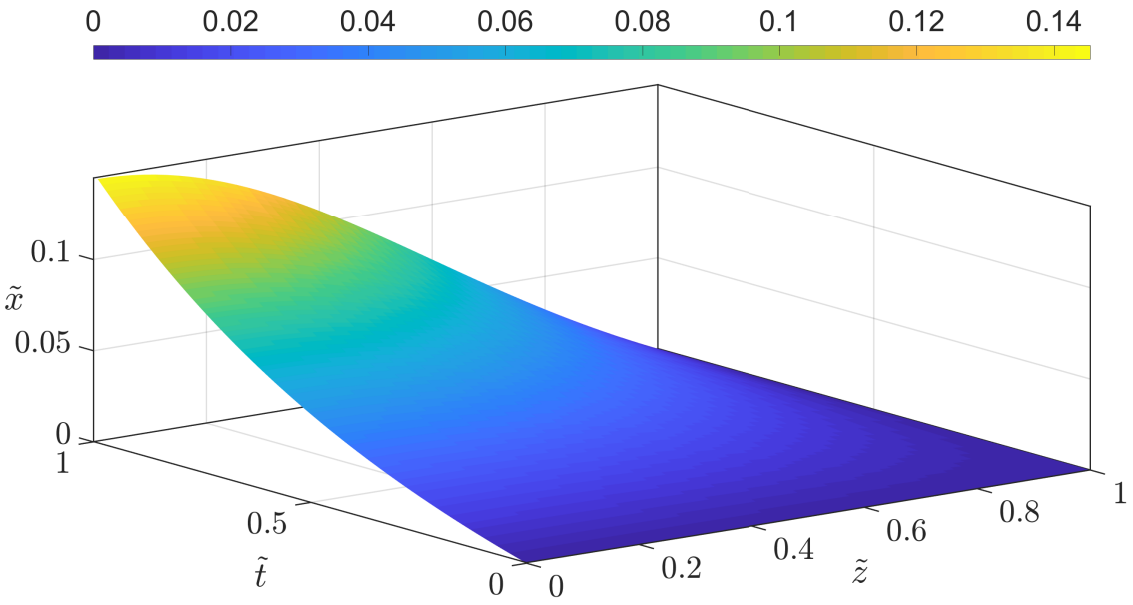

Figure 4.4: Space-time phase space of trajectories of points in flow described by equation 4.4 and following notation shown in Figure 4.1. At $\tilde{t} = 0$, $\tilde{x} = 0$. As time progresses, particle paths follow the background velocity field. Points at the center of the channel ($\tilde{z} = 0$) travel the furthest while points at the wall do not move.

The phase space has several interesting features worth elaborating. Figure 4.4 shows that any point at the wall ($\tilde{z} = 1$) does not undergo any motion in time and the point at the center of the flow ($\tilde{z} = 0$) undergoes the maximum translation. This is consistent with the boundary condition of no-slip at the wall and a parabolic

$\tilde{u}$ velocity profile where the magnitude is maximum at the center of the channel. The part of the phase space along $\tilde{z} = 0$ is also consistent with the results from a previous study [16] which experimentally validated equation 4.4. The phase space can also be extended to longer $\tilde{t} = 1$ depending on the flow time.

4.5.2 Comparison with experiments

The phase space in Figure 4.4 can be used to predict the final length attained by drops in the flow. We illustrate this by considering an example where a drop was initially injected into the flow at $\tilde{x} = 0$ and suspended between $\tilde{z}_1 = 0.4$ and $\tilde{z}_1 = 0.6$. By tracking the two points on the drop as explained in section 4.3, we obtain the trajectory of the points in time as shown in Figure 4.5. At $\tilde{t} = 1$, the final length attained by the drop is the difference in $\tilde{x}$.

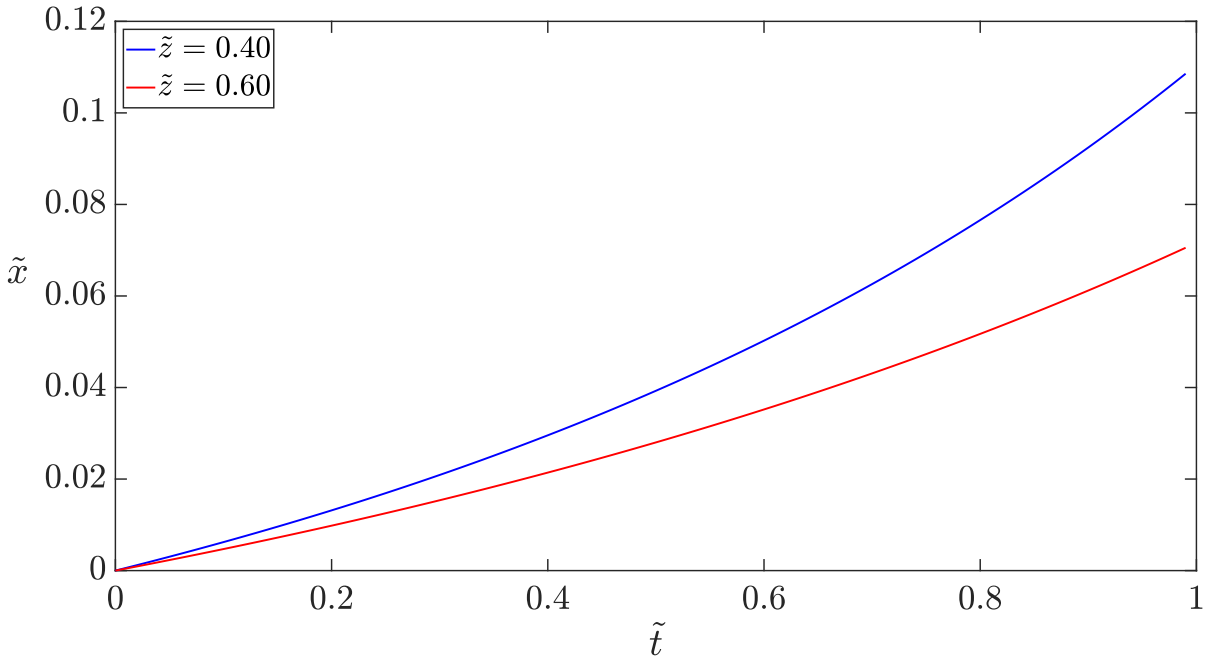

Figure 4.5: Trajectories for $\tilde{z}_1 = 0.4$ and $\tilde{z}_1 = 0.6$ extracted from Figure 4.4. The two points separate from each other along the plotted trajectories. Difference in $\tilde{x}$ at any time instant provides a measure of their separation.

Finally, we compare the model the with the experimental results for drops injected at $\tilde{z} = 0.4, 0.5, 0.6$. Figure 4.6 shows the final lengths predicted by the model and the experimentally obtained results. Given the assumptions in section, the model gives reasonably good predictions of the final lengths of the drops.

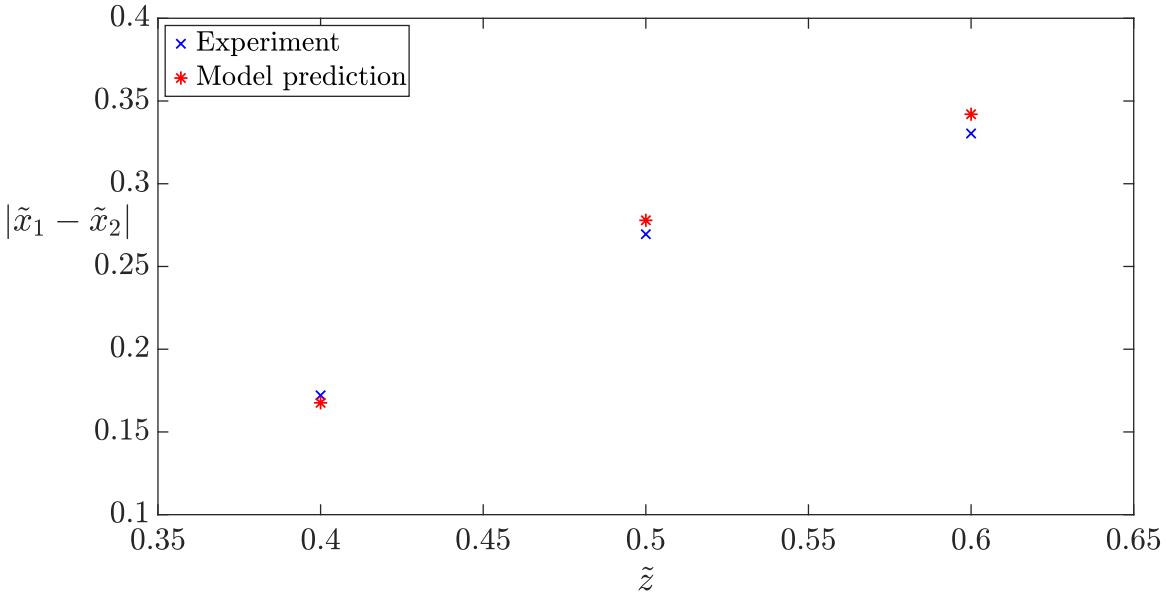

Figure 4.6: Comparison of model prediction of drop lengths $|\tilde{x}_1 - \tilde{x}_2|$ vs experimental measurements.

Figure 4.6 shows that drops injected closer to the channel walls deformed the largest for nearly the same time spent in the flow. Our results show that the influence of shear close to the channel walls imposes larger strain on the drop than a previous study [16] which deformed drops under pure extensional flow at the same flow rate.

4.6 Conclusion

In conclusion, we presented a model that described the deformation of drops suspended in a low Reynolds number flow. We chose a planar converging flow – commonly found in nozzles of additive manufacturing machines and extensional mixers in emulsion industries – and first described a low Reynolds number single phase flow using lubrication theory. While previous work [16] had successfully

validated the theory for pure extensional flow along the centerline, we studied other locations in the flow that were shear-influenced. As shown in section 4.5, such flows reliably elongate drops to lengths that are at least an order of magnitude larger than the initial drop size.

In the flow, we tracked the trajectory of points following the flow and presented a simple method to calculate the net deformation of suspended drops – specifically the final length attained after shear-influenced deformation. We performed experiments that validated our model for several combinations of processing conditions.

In summary we have shown in this work that, under specific assumptions, concepts from lubrication theory and mixing kinematics can be combined to predict drop deformation. We believe that our model will be useful to industries where drop dispersion in a well-defined mixer is a key process.

Chapter 5: Effect of inertia on extensional deformation and capillary-driven breakup of drops

5.1 Abstract

We investigated extensional deformation of drops suspended in stagnant and non-stagnant extensional flows, and the subsequent capillary-driven breakup after flow stoppage. While the low Reynolds number approximation of the problem has received experimental and theoretical attention over the years, the influence of inertia on both phenomena is not well studied. First, using direct numerical simulations we validated our scheme with previous experimental results and showed that the influence of inertia on elongating drops resulted in slightly longer stable shapes. Next, we considered a slender drop suspended in a quiescent fluid – representing external flow stoppage condition – and systematically studied the capillary-driven breakup of the drop in a previously unexplored part of the parametric space. Both inertial and viscous effects of the outside fluid were considered. In the new space, we showed how the structure of the flow field was modified upon addition of inertia and presented a stability diagram for slender drops.

5.2 Introduction

A fundamental trait of single-phase viscous fluid flow is the presence of spatial or temporal velocity gradients in the flow. These velocity gradients can be used to deform suspended particles – providing a way to produce dispersions in immiscible liquid-liquid systems [8, 86]. The fluid dynamics problem of drop deformation and breakup is of interest to several industries, like petroleum and pharmaceutical [87], all aiming to improve efficiency of their mixing devices. Flow in such mixing devices are typically associated with inertia, either in the laminar or turbulent regime, where the suspended drop first deforms in the flow and subsequently undergoes either flow-driven or capillary-driven breakup. While the drop deformation in low Reynolds number flows is well studied [22, 24, 88], the role of inertia in such systems – especially in the capillary-driven breakup regime – has received less attention. In this study, we investigate the role of inertia of the external flow in deforming drops and its subsequent influence on capillary-driven breakup.

The problem of drop deformation in another fluid undergoing motion is a classical fluid dynamics problem and has been well researched over the past century [4, 5]. Determining the shape of a drop in a flow is non-trivial because of the presence of the free boundary of the droplet whose shape has to be determined as part of the solution [8]. Thus, studying the problem experimentally necessitates simplification of other flow variables so that the problem is easier to solve. One such simplification is the assumption of a linear flow field external to the drop, far from it. Implicit in this assumption is that the size of the drop is small compared to a length scale of

the bulk flow [23]. Such linear flow fields generate a spatially homogeneous velocity gradient which deforms the drop. Using this assumption, drop deformation in the low Reynolds number regime has been investigated using experimental [2, 4, 33], theoretical [9, 26, 89], and numerical methods [90, 91, 91, 92, 93] – leading to the determination of the stability criterion for drops in such flows. A natural question that arises is: what happens to drops when inertial effects are considered in such systems?

While the problem of drop deformation with inertial effects is considerably harder to solve with classical methods, there have been some attempts to extend the small-deformation and slender body theories to the inertial domain [22, 94]. The presence of inertia in the external flow provides additional aid to the viscous force that deforms the drop. Thus, longer steady drop shapes that are stabilized by the larger dynamic pressure of drops in the flow is expected in this regime. Several numerical studies have shown this effect [95, 96, 97, 98] and we use that data to validate our numerical scheme in this study. While it is natural to assume that it would be easier to breakup drops in an inertial flow, it has been shown that the external flow – with or without inertia – continuously postpones breakup. Thus, another framework is necessary to breakup drops in such multiphase systems.

One way to achieve breakup of slender drops is by stretching them to the desired slenderness and stopping the external flow. This onsets a capillary flow in the drop which can induce breakup [1]. Another possibility is retraction of the drop back to the original shape if the slenderness is inadequate. Regardless of the outcome, since the capillary flow problem involves two fluids, the problem can be

studied in different parts of a parametric space that comprises viscosity ratio – which is the ratio of viscosity of inner fluid to the outer fluid – and the magnitude of Reynolds number. We now review the drop behavior in different parts of this parametric space and hypothesize the behavior in an unexplored part of the space.

When the viscosity ratio is very large, the viscosity of the external fluid can be neglected. At large Reynolds number, the behavior in this regime has been widely studied both experimentally [12, 13, 15] and theoretically [10, 14]. From an initial steady state, the two ends of the drop retract towards each other minimizing the interfacial area. A recent study has shown that capillary waves emerge from both ends on the surface of the drop and interact with each other leading to their interference [15]. Depending on the initial slenderness, the drop either retracts into a single sphere or undergoes end-pinching. Inertial effects in this regime also cause non-monotonic pinching of the ends especially at large Reynolds number. As the Reynolds number is reduced, increasing viscous effects lead to suppression of all capillary waves and at the limit $Re \to 0$, a slender drop cannot breakup regardless of slenderness [11].

The same problem of retraction of a slender drop at different Reynolds number can also be studied in finite viscosity ratio systems. In this part of the parametric space, the slender drop is surrounded by a another viscous fluid. Depending on the slenderness of the drop, at the limit $Re \to 0$, it either undergoes retractive end-pinching [1, 89], where the ends of the drop pinch-off successively, or undergoes breakup by the mechanism of capillary wave instability where a large number of daughter drops are formed at the same time. This begets the question: can the

dynamics of capillary wave interaction and non-monotonic end pinching seen in systems with infinite viscosity ratio be reproduced in the current space? To answer this question, we investigated the dynamics in the new part of the parametric space by adding inertial effects to the finite viscosity ratio problem.

This chapter is organized as follows. We first begin with a description of the problem statement and the numerical method we use to investigate it. Next, we present our findings in two parts. The first part reveals the effect of inertia on drops in an extensional flow field. In the second part, we remove the external flow field and allow an elongated drop to retract under the influence of interfacial tension. Finally, we summarize the effect of inertia on both phases and discuss the significance of our findings.

5.3 Methods

5.3.1 Problem setup

In this study, we first investigated the extensional behavior of immiscible drops in an externally imposed linear flow field at finite Reynolds number. The flow field was defined with x and y velocity components as u and v respectively. They were specified as

$$u = \dot{\gamma} x \tag{5.1}$$

and

$$v = -\dot{\gamma} y \tag{5.2}$$

where $\dot{\gamma}$ was the magnitude of the strain rate. This flow field produced a stagnation point at $(x, y) = 0$ and when a drop was suspended at this point, it underwent extension and the degree of extension depended on the magnitude of $\dot{\gamma}$. The schematic representation of the domain is shown in figure 5.1.

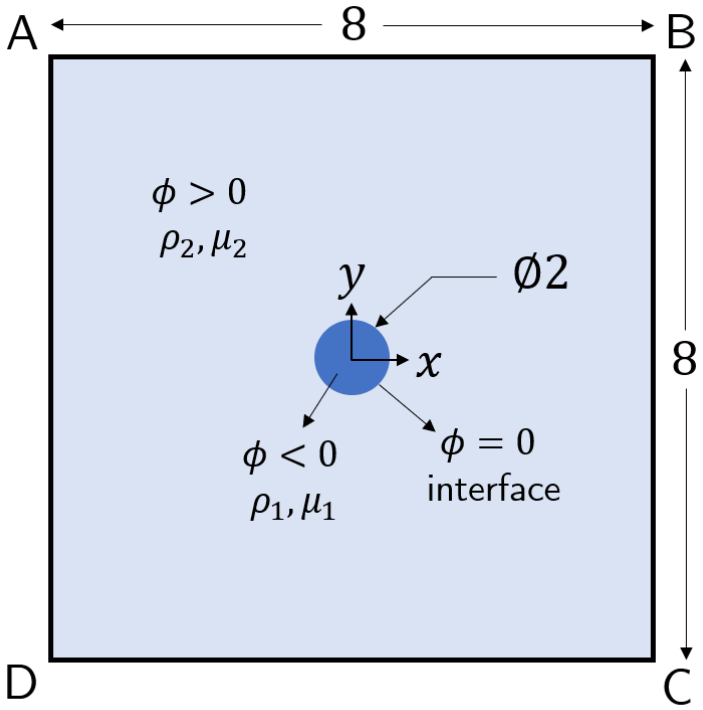

Figure 5.1: Domain for the stagnant extensional flow problem. The drop is shown suspended at the center of a square 8 X 8 domain. All dimensions are non-dimensionalized using a length scale equal to the initial radius of the drop.

The drop with viscosity μ_1 and density ρ_1 is shown suspended in another fluid with viscosity μ_2 and density ρ_2 at the center of a square domain with $\rho_1 = \rho_2$. The interfacial tension between the two fluids was σ. Using the initial radius (a) of the drop as the length scale and velocity magnitude (V) of the external flow at the edge center of the domain, we studied the drop elongation at various Reynolds numbers

(Re_s) and Weber numbers (We_s) defined as

$$Re_s = \frac{\rho_2 V a}{\mu_2} \tag{5.3}$$

and

$$We_s = \frac{\rho_2 V^2 a}{\sigma} \tag{5.4}$$

respectively.

To study non-stagnant extension of drops, a converging channel configuration shown in figure 5.2 was used. The walls of the channel was based on a hyperbolic equation and the flow was capable of imposing a constant extension rate along the centerline.

Reynolds number (Re_{ns}) and Weber number (We_{ns}) was redefined using length scale equal to the inlet width (L_{in}) and velocity scale equal to the inlet x component of velocity (V_{in}) at the origin in figure 5.2.

$$Re_{ns} = \frac{\rho_2 V_{in} L_{in}}{\mu_2} \tag{5.5}$$

and

$$We_{ns} = \frac{\rho_2 V_{in}^2 L_{in}}{\sigma} \tag{5.6}$$

As drops elongated in the flow for various values of Re_{ns} and We_{ns}, they attained elongated shapes consistent with the balance between viscous stress and interfacial stress. However, to study the effect of inertial and viscous forces on the drop when the forcing flow was removed, a simpler configuration of a slender drop

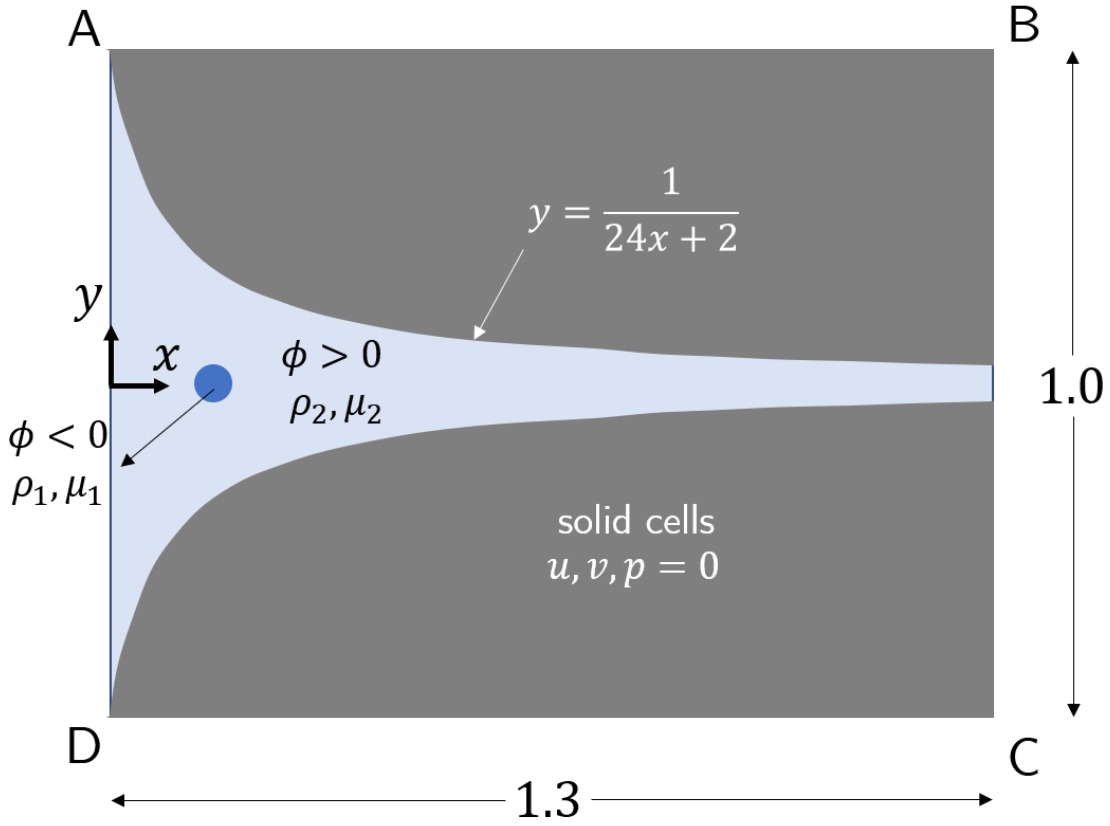

Figure 5.2: Domain for the non-stagnant extensional flow problem. The drop is shown suspended in a converging channel. All dimensions are non-dimensionalized using a length scale equal to the inlet width of the channel (120 mm).

with hemispherical ends – consistent with previous studies [3, 10, 12, 15] – was chosen. The schematic representation of a quarter of the domain is shown in figure 5.3.

The long, slender drop is shown suspended in the external fluid which is now quiescent. Due to the large curvature of the ends, a net force due to interfacial tension acted – leading to retraction of the drop. From the initial state, the slender drop was allowed to evolve under the influence of this interfacial tension and the phenomenon was studied for different Reynolds numbers (Re_c). Initial radius of the end cap (r_c) of the slender drop was the length scale for the problem. Since there

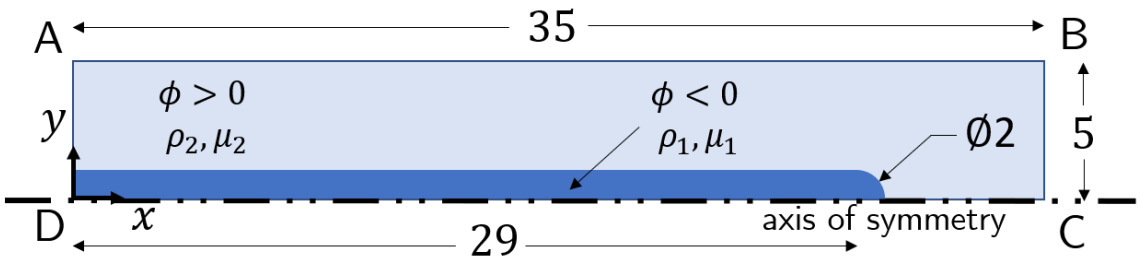

Figure 5.3: Quarter domain for the capillary-driven flow problem. A long slender drop is shown suspended in another quiescent fluid. The drop has an aspect ratio = 30. Such slender drops are unstable at moderate Reynolds numbers when the effect of the surrounding fluid is ignored.

was no imposed velocity scale like the previous case of an externally-driven flow, the velocity scale (V_c) for the problem was equal to $\sqrt{\sigma/\rho_1 r_c}$. This was equaivalent to setting the Weber number (We_c) equal to 1. Reynolds numbers (Re_c) was defined as

$$Re_c = \frac{\rho_1 V_c r_c}{\mu_1} \tag{5.7}$$

5.3.2 Governing equations

The governing equations for the problems were the mass conservation equation and the momentum conservation equation where both fluids were assumed to be incompressible and isothermal. The equations were

$$\nabla \cdot \mathbf{u} = 0 \tag{5.8}$$

and

$$\rho \left[\frac{\partial \mathbf{u}}{\partial t} + (\mathbf{u} \cdot \nabla)\mathbf{u} \right] = -\nabla p + \nabla \cdot \left[\mu \left(\nabla \mathbf{u} + \nabla \mathbf{u}^T \right) \right] + \rho \mathbf{g} \tag{5.9}$$

where $\mathbf{u}$ is the velocity vector, ρ is density, μ is the dynamic viscosity, p is pressure, t is time, and $\mathbf{g}$ is the gravity vector. These equations in the context of the current two-phase flow problem were valid within both fluids. However, the presence of an immiscible boundary between the two fluids needed separate treatment. We used a level-set function $\phi(\mathbf{x}, t)$ to capture the evolution of the immiscible boundary and the ghost-fluid method [99] to capture the interfacial dynamics. The level-set function was an implicitly defined function with magnitude equal to zero on the immiscible boundary, negative within the drop, and positive outside the drop. See figures 5.1 or 5.2 for definitions. The level-set function was advected using the local fluid velocity $\mathbf{u}$ by the equation

$$\frac{\partial \phi(\mathbf{x}, t)}{\partial t} + \mathbf{u} \cdot \nabla \phi(\mathbf{x}, t) = 0. \tag{5.10}$$

This provided a way to capture the evolution of the interface between the two fluids using the solution of the flow from equation 5.9. Since the same equation was numerically solved in both the phases, ρ and μ were specified as a function of $\phi(\mathbf{x}, t)$ so that a single equation for ρ and μ could be used in the entire domain. The equations for ρ and μ were:

$$\rho = \rho_1[1 - I(\phi)] + \rho_2 I(\phi) \tag{5.11}$$

and

$$\mu = \mu_1[1 - I(\phi)] + \mu_2 I(\phi). \tag{5.12}$$

In equations 5.11 and 5.12, $I(\phi)$ is a smooth function that allows for the variables to smoothly change across the interface where a sudden jump in ρ and μ occurs. We allowed a smooth transition of ρ and μ across a distance ϵ equal to twice the grid resolution Δ. Thus, $I(\phi)$ was given by

$$I(\phi) = -\frac{1}{2}\,\mathrm{erf}\left(\frac{\phi}{\varepsilon}\right) + \frac{1}{2}. \tag{5.13}$$

where erf $\in [-1, 1]$ was the error function. Since the problems we investigated had interfaces associated with interfacial tension, the pressure across the interface underwent a jump in magnitude $[p]_I$ depending on the degree of the interfacial curvature κ. Thus, $[p]_I$ was given by

$$[p]_I = \sigma\kappa. \tag{5.14}$$

The curvature κ of the interface was estimated using ϕ as

$$\kappa = \nabla \cdot \frac{\nabla\phi}{|\nabla\phi|} \tag{5.15}$$

5.3.3 Numerical scheme and boundary conditions

The domains shown in figures 5.1, 5.2, and 5.3 were discretized into staggered grids with square cells where the x component of velocity was computed at the center of east edge and y component of velocity was computed at the center of the north edge. Scalar variables like pressure, density, viscosity, and ϕ were computed

at the cell centers. A depiction of a staggered cell is shown in figure 5.4.

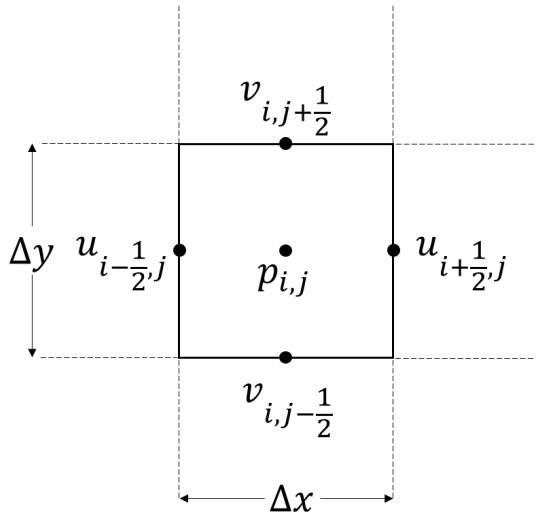

Figure 5.4: Discretization scheme for the numerical method. In the shown staggered cell with grid spacing $\Delta x = \Delta y$, the vector variables are defined on the cell faces and scalar variables are defined on the cell centers.

For the initial study of drop elongation in the external flow given by equation 5.1 and 5.2, we discretized the domain shown in figure into 128 X 128 cells. For the non-stagnant extension, we discretized the domain into 640 X 480 cells. Finally, for the study of capillary-driven breakup of the slender drop, we discretized the domain shown in figure into 980 X 70 cells. Grid independence was particularly important for the capillary-driven breakup problem and was verified at different levels of domain discretization. The governing equations were solved using the projection method. For the first stage of our study where we explored drop elongation in stagnant and non-stagnant extensional flows, we solved the equation in a two-dimensional domain to accurately capture the influence of a planar external flow. For the subsequent stage of our study where we explored capillary flow in slender drops, it was important to capture both the radii of curvature that characterized the

interface. We thus solved the governing equations in an axisymmetric domain for the second state of our study. We used a fifth-order weighted essentially nonoscillatory (WENO) scheme to discretize equation 5.10 and the ghost-fluid method to capture the pressure jump across the interface. Finally, after every time step, we reinitialized the interface by reconstructing ϕ as the minimum distance from the grid to the interface. This allowed for the projection of interface topology onto the cartesian grid without modifying the underlaying scalar variables [100]. The numerical scheme was validated in previous studies for different applications [101, 102, 103].

Boundary conditions for the stagnant extensional flow problem in figure 5.1 were as follows. We applied a Neumann boundary condition for pressure and imposed the constant velocity defined in equations 5.1 and 5.2 on the four walls of the domain. For the non-stagnant extensional flow problem in figure 5.2, Dirichlet boundary condition for pressure was applied on wall BC while Neumann boundary condition was used for the other three walls. At the inlet AD, a parabolic velocity profile – corresponding to a fully developed flow upstream – was defined with zero velocity at A and D. The solid cells along the walls of the channel had no-slip velocity condition. Fully developed flow profile for a single phase low Reynolds number flow was initialized throughout the domain.

For the axisymmetric problem in figure 5.3, the boundary conditions were slightly different. Dirichlet boundary condition for pressure was imposed on wall BC and the while Neumann boundary condition for pressure was imposed on walls AB and CD. Since CD was the axis of symmetry, we imposed a symmetric boundary condition for velocity while no-slip and no-flux was imposed on wall AB. On the wall

BC, we imposed a symmetric boundary condition for u and slip boundary condition for v allowing the fluid to freely flow out of the domain. The boundary conditions for pressure and velocity on the wall symmetric to BC (at $x = -70$) about the y axis was the same as the conditions on BC. At the initial state, we set $v, p = 0$ and allowed the capillary flow to develop.

Computations were perfomed using UMD supercomputing resources. The domain in all three cases was split into 4 zones and the governing equations were solved using a parallel computing framework.

5.3.4 Parametric space for numerical experiments

For problem defined in figure 5.1, we were interested in exploring the effect of inertia on extensional deformation of the drop. We first set viscosity ratio $\lambda = 1.00$, $Re_s = 1.00$, and systematically varied the We_s from 0.05 to 0.11. These conditions were consistent with the previous study by Ramaswamy et al. [96] who explored uniaxial elongation of drops in an axisymmetric external flow. We used the same parameters in our simulation for validation purpose. For every condition we allowed the drop to elongate till it attained a steady state in the flow.

Similarly, for the non-stagnant extensional flow, we studied conditions that caused stable and unstable drop behavior. A previous study by Sangli and Bigio [16] had classified drop behavior in non-stagnant extensional flows at different capillary numbers (Ca). We chose a condition from their study corresponding to unstable behavior of the drop at $Ca = 0.65$. Given our choice of velocity and length scales,

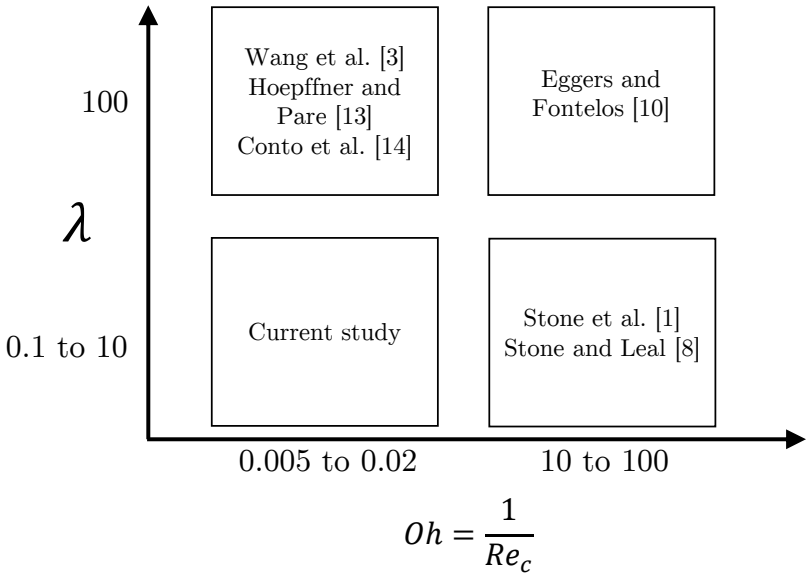

Figure 5.5: The parametric space for investigation of capillary-driven breakup of slender drops. The space comprises viscosity ratio (λ) and Ohnesorge number (Oh). In this study, both inertial and viscous effects of the outside fluid are considered.

these conditions corresponded to $Re_{ns} = 2.53, We_{ns} = 7.99$ respectively.

For the subsequent study of capillary-driven flow, the parametric space described in section 5.2 is succinctly represented in figure 5.5. We chose three different viscosity ratios $\lambda = 0.01, 0.10, 1.00$ and four different Reynolds numbers $Re_c = 25, 50, 100, 200$. Ohnesorge number (Oh) was defined as

$$Oh = \frac{\sqrt{We_c}}{Re_c} = \frac{1}{Re_c} \tag{5.16}$$

5.4 Results and discussion

5.4.1 Inertial effects on drop deformation in stagnant extensional flow

In this section, we report the drop elongation behavior for both the viscosity ratios studied at $Re_s = 1.00$. Figure 5.6 shows the steady elongated states attained by drops at various conditions.

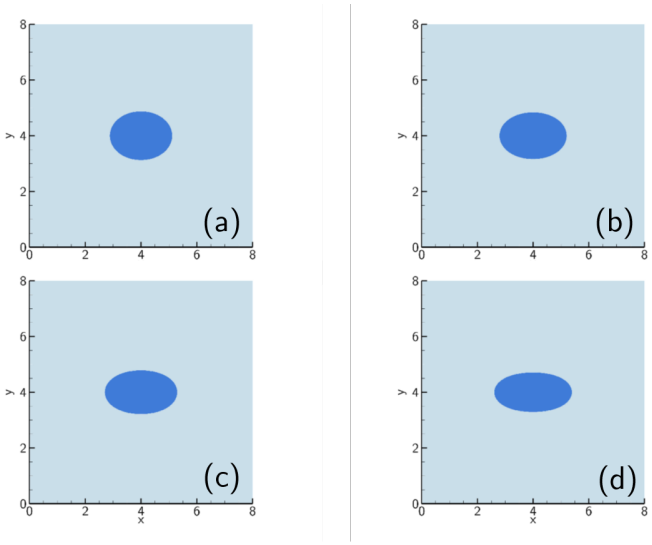

Figure 5.6: (a) to (d) shows the steady states of drops at $We_s = 0.05$, $We_s = 0.07$, $We_s = 0.09$, and $We_s = 0.11$ respectively. Reynolds number (Re_s) for all cases is equal to 1.

We defined a non-dimensional deformation metric for an elongated drop shown in figure 5.7 as

$$D_f = \frac{L - b}{L + b} \tag{5.17}$$

and compared it with the measurements by Ramaswamy et al. [96] in figure 5.8. Comparing the steady state D_f at $Re_s = 1.00$ with creeping flow $Re_s \to 0$, we observed that steady shapes tended to be longer. This observation was consistent

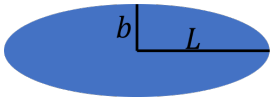

Figure 5.7: Semi-major length L and semi-minor length b of a deformed drop.

with the previous study in this area by Ramaswamy et al. [96]. Note that in creeping flows, capillary number captures the effect of viscous deforming force (instead of inertial deforming force) over the interfacial force. The Weber number is related to the capillary number as $We_s = Re_s * Ca$ where Ca is the capillary number. At $\lambda = 1.00$, longer steady shapes at the same Weber number indicated that the presence of slight inertia in the flow allowed the associated dynamic pressure to stabilize longer drops. The last Weber number studied was the critical Weber number beyond which no stable shape was observed.

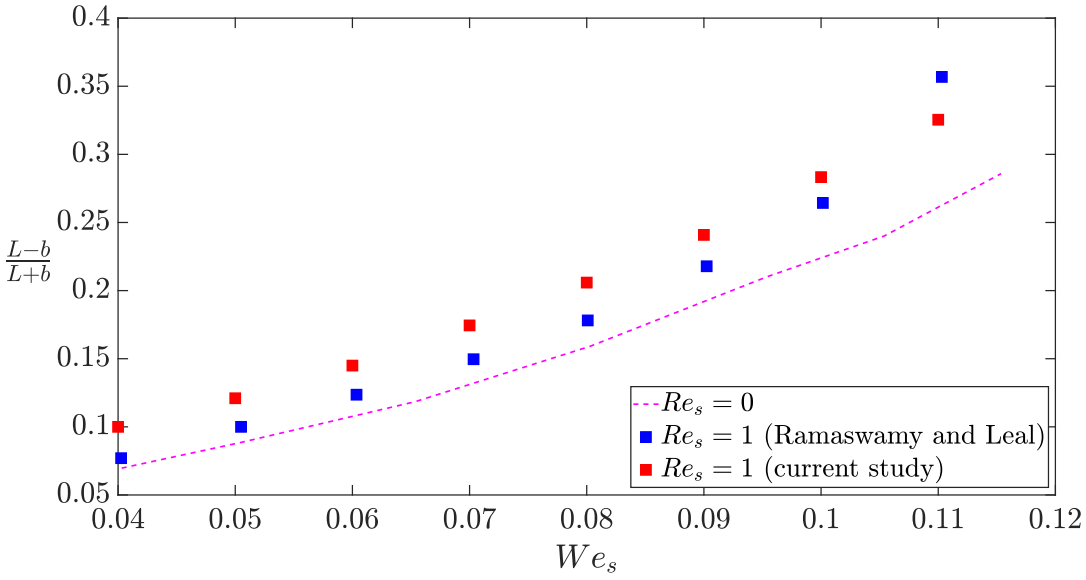

Figure 5.8: Effect of slight inertia at $Re_s = 1$ on drops undergoing stagnant extension.

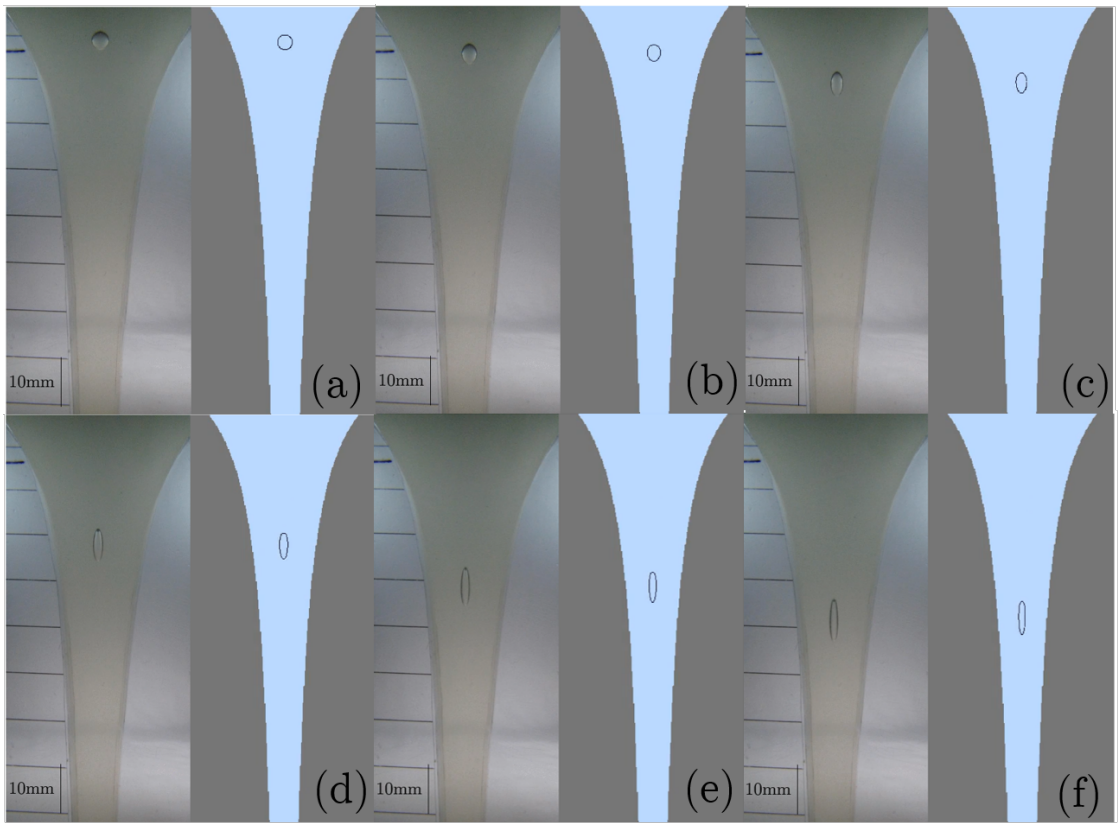

Figure 5.9: (a) to (f) represent transient deformation of drops in a non-stagnant extensional flow at $Re_{ns} = 2.53$ and $We_{ns} = 7.99$. The left panel in every image is the experimental observation and the right panel is the computational result.

5.4.2 Inertial effects on drop deformation in non-stagnant extensional flow

Figure 5.9 shows the transient drop deformation at $Re_{ns} = 2.53, We_{ns} = 7.99$. Note that the drop deforms and continuously elongates as long as it is present in the flow field. The flow is strain-limited because of the finite length of the channel. Thus, there is an upper bound for total strain on the drop. Figure 5.10 shows the comparison with experiments at the same condition.

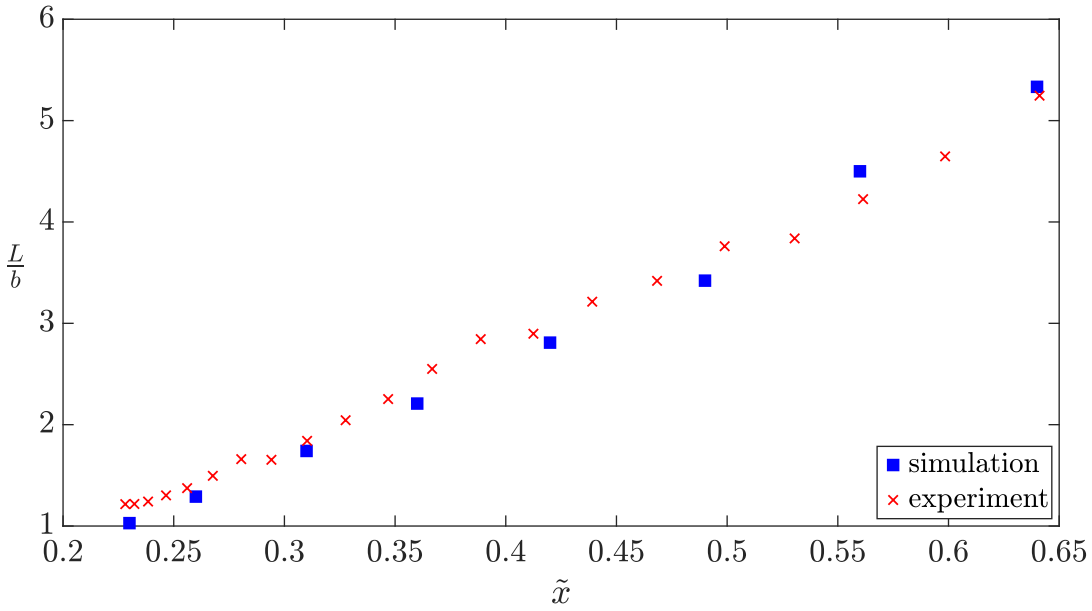

Figure 5.10: Comparison of simulation and experimental results for non-stagnant extension of a drop at $Re_{ns} = 2.53$ and $We_{ns} = 7.99$.

5.4.3 Inertial effects on capillary-driven breakup

In the previous sections, we studied how an external flow can cause drops to elongate and become unsteady after the critical Weber number is exceeded. As the deformation progresses, the drop becomes slender. However, breakup can be hard to achieve with this mode since the external flow stabilizes any perturbation on the surface whose growth can lead to breakup. For slender drops, the magnitude of interfacial force at the ends is inversely proportional to the radius of curvature. Thus, the large interfacial force can be taken advantage of to cause drop break-up. When the external flow is removed, the slender drop finds itself overstretched in the quiescent field. Interfacial force dictates the dynamics and tends to minimize the interfacial area. It achieves this by either retracting into a single drop or breaking

up the interface to create multiple smaller drops.

5.4.3.1 Validation with previous experiments

Before studying the capillary-driven breakup in the new parametric space, we validated the simulation scheme with previous experimental results. Wang et al. [3] studied retraction of water drops in air under inertia and presented a stability criterion for slender drops of different aspect ratios. We chose an experimental result reported at $Oh = 0.0057$, setup a numerical simulation as per sections 5.3.2 and 5.3.3, and compared the evolution of drop shape in the capillary-driven flow. Figure 5.11 shows the comparison between experimental results and the simulation.

Wang et al. [3] report the experimental result in figure 5.11 for a slender drop with initial aspect ratio equal to 12. However, we observed good agreement with the experimental result for an aspect ratio equal to 14. This slight discrepancy can be attributed to a combination of the following reasons.

1. Difference in numerical scheme between the two studies.

2. Experimental error in measurement of the initial drop shape in figure 5.11.

3. Difference in shape of the end and neglecting the initial impulse that resulted in the creation of the slender shape.

Since our numerical scheme was capable of providing insights into capillary-driven breakup, we chose to proceed with studying the dynamics in the parametric space of figure 5.5.

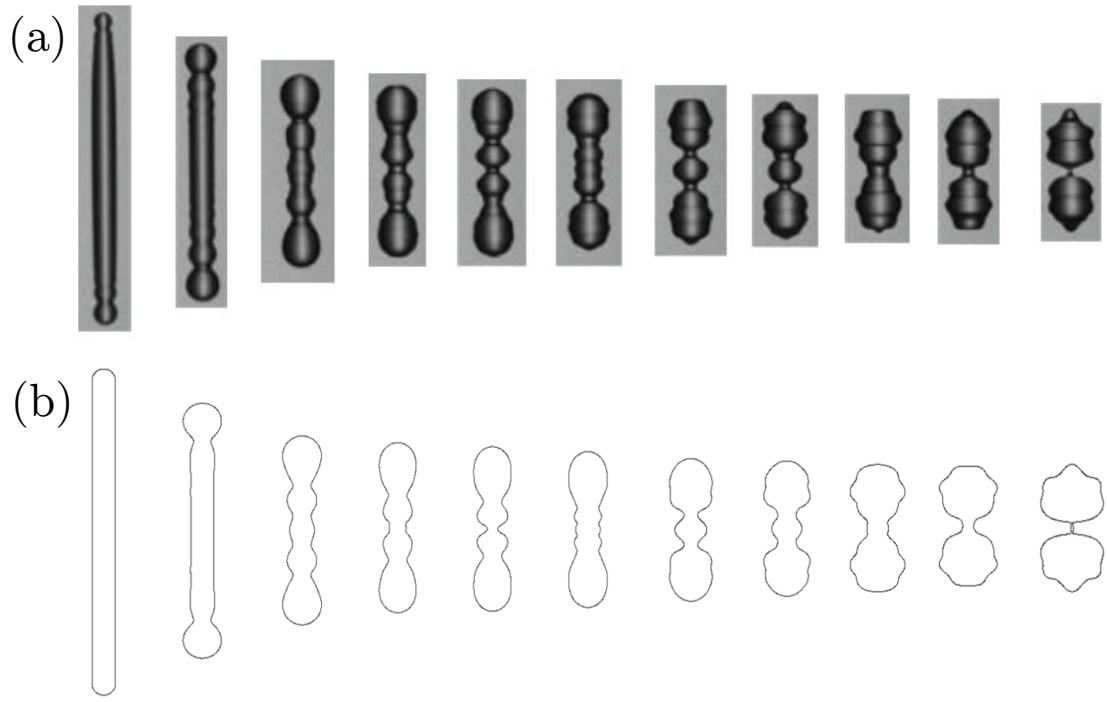

Figure 5.11: Comparison of (a) experimental results [3] and (b) simulations of capillary-driven breakup at $Oh = 0.0057$.

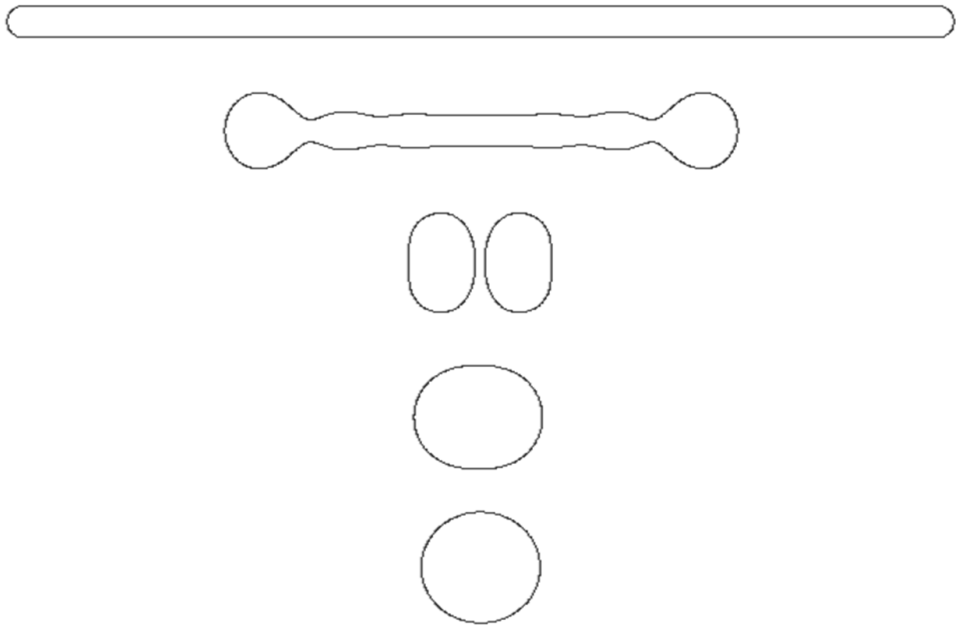

Figure 5.12: Capillary driven flow at $Re_c = 25$ and $\lambda = 1.00$. The drop is conditionally unstable – breaking up into two daughter drops – but asymptotically stable.

5.4.3.2 Capillary-driven breakup in new parametric space

Figure 5.12 shows the interfacial force driven flow for a sample case of $Re_c = 25$ at a viscosity ratio $\lambda = 1.00$.

The slender drop initially retracts under the effect of the interfacial force and the radius at the ends become larger. In time, it can be seen that the drops pinch off and yet re-coalesce to produce a single drop. Thus, the instability is conditional and the system is asymptotically stable. The behavior can be explained as follows. The bulb at the end of the slender drop traverses through the outer fluid of the same viscosity. Inertia in the system provided enough momentum for the bulbs from

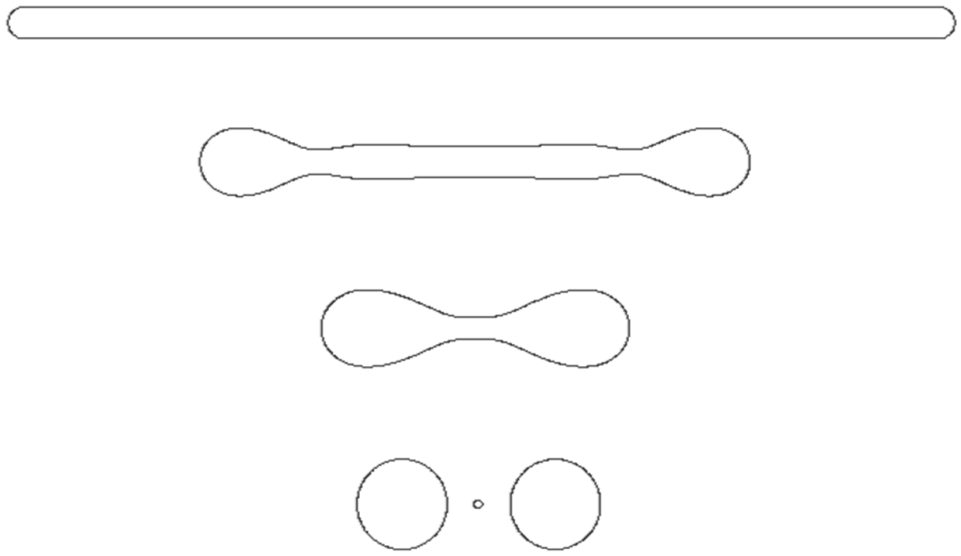

Figure 5.13: Capillary driven flow at $Re = 25$ and $\lambda = 0.10$. The drop is asymptotically unstable and results in two daughter drops with a small satellite drop suspended between them.

both ends to collapse into each other. However, after breakup, there was enough momentum available in the bulbs – which is basically an inertial effect – to cause re-coalescence. This observation can be used to tune the behavior of the slender drop to generate multiple drops after breakup by increasing the viscosity of the outside fluid. Figure 5.13 shows the drop behavior at viscosity ratio $\lambda = 0.10$.

In this case with the same amount of inertia in the system, the motion of the bulb through the higher viscosity fluid was hindered. This resulted in pinch off of the end of the drop and the bulbs were held in place in the high viscosity fluid. Viscous effect had a damping influence on the bulb momentum and the system asymptotically generated two drops. Continuing this trend by further increasing

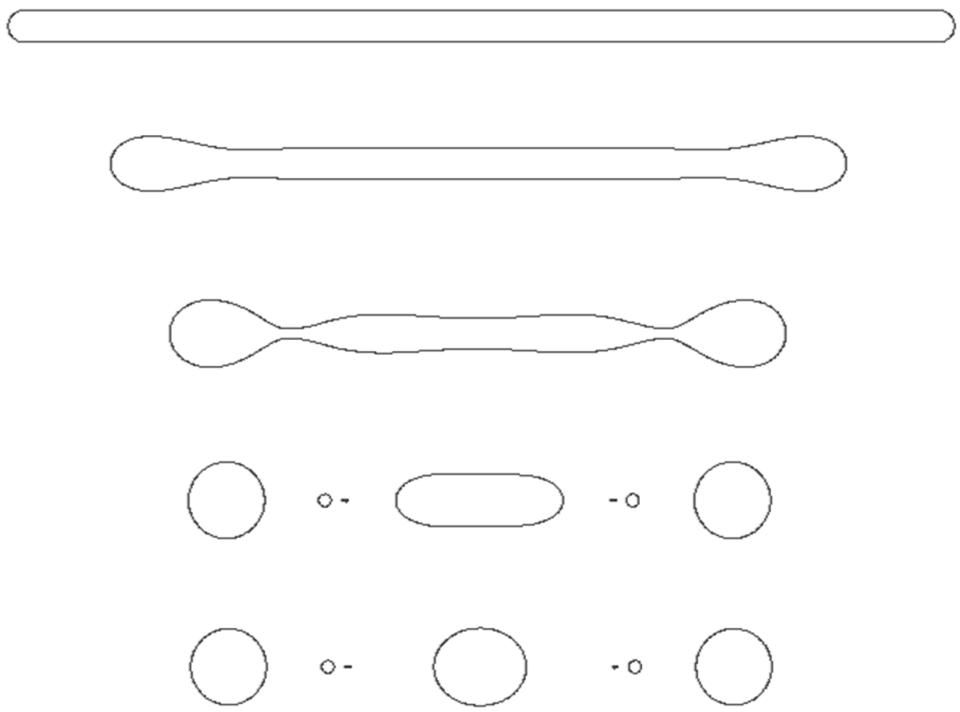

Figure 5.14: Capillary driven flow at $Re_c = 25$ and $\lambda = 0.01$. This drop is asymptotically unstable – resulting in three daughter drops with satellite drops between them.

the viscosity of the outside fluid ($\lambda = 0.01$), we see behavior shown in figure 5.14.

Three drops are asymptotically produced in this case. The system thus undergoes a transition from asymptotically stable to asymptotically unstable state between $\lambda = 1.00$ and $\lambda = 0.10$. We investigated this transition point over different Reynolds numbers. Figure 5.15 shows the asymptotic end states of the drops in the parametric space.

It can be seen in figure 5.15 that the transition point is inversely proportional to the Reynolds number. Since Reynolds number represents a balance between inertial and viscous forces, increasing Reynolds number equips the bulb with enough momentum to support coalescence over breakup. Thus, even when the surrounding

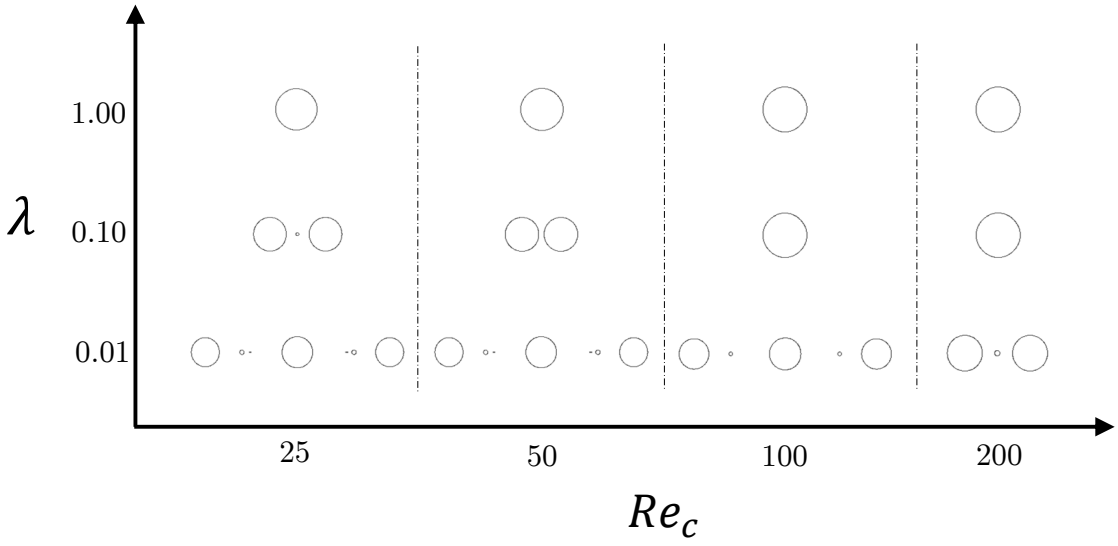

Figure 5.15: Asymptotic fates of the slender drop for different combinations of viscosity ratio (λ) and Reynolds number (Re_c).

fluid is highly viscous ($\lambda = 0.01$), inertia overcomes the damping effect of the outside fluid and reduces the number of daughter drops after breakup.

5.4.3.3 Effect of viscosity ratio on vorticity diffusion

Recent studies [3, 14, 15] have shown that the fate of a slender drop suspended in air ($\lambda \to \infty$), retracting under the effect of surface tension, depends on the interaction of capillary waves emerging from the two ends. Examination of vorticity inside the drop revealed the formation of a vortex ring and a detached-jet type of flow which caused the neck – the point of minimum radius on the stem – to reopen. In such systems, the pinch off was non-monotonic and was postponed to later time since the neck reopened. While the capillary wave interaction model can explain the fate

of drops suspended in air, the presence of the outside fluid complicates the associated dynamics. Our parametric space comprised of $\lambda \leq 1.00$ where viscous diffusion into the surrounding fluid could be an important factor affecting the dynamics. This is especially true at $\lambda = 0.01$ where, similar to breakup in systems with no inertia [1], the neck pinch-off was monotonic and no neck reopening effect was observed. Thus, a combination of signature effects of both parts of the parametric space – 1) $Re_c \to 0$ with finite λ and 2) Finite Re_c with $\lambda \to \infty$ – were observed in our study leading to the behavior seen in figure 5.15.

A closer examination of the capillary flow allowed for a detailed description of the neck reopening phenomenon reported in previous studies. Figures 5.16, 5.17, and 5.18 shows the evolution of the flow at three snapshots in time – before neck reopening, at minimum neck radius, and after neck reopening – at $Re_c = 100$ and $\lambda = 1.00$.

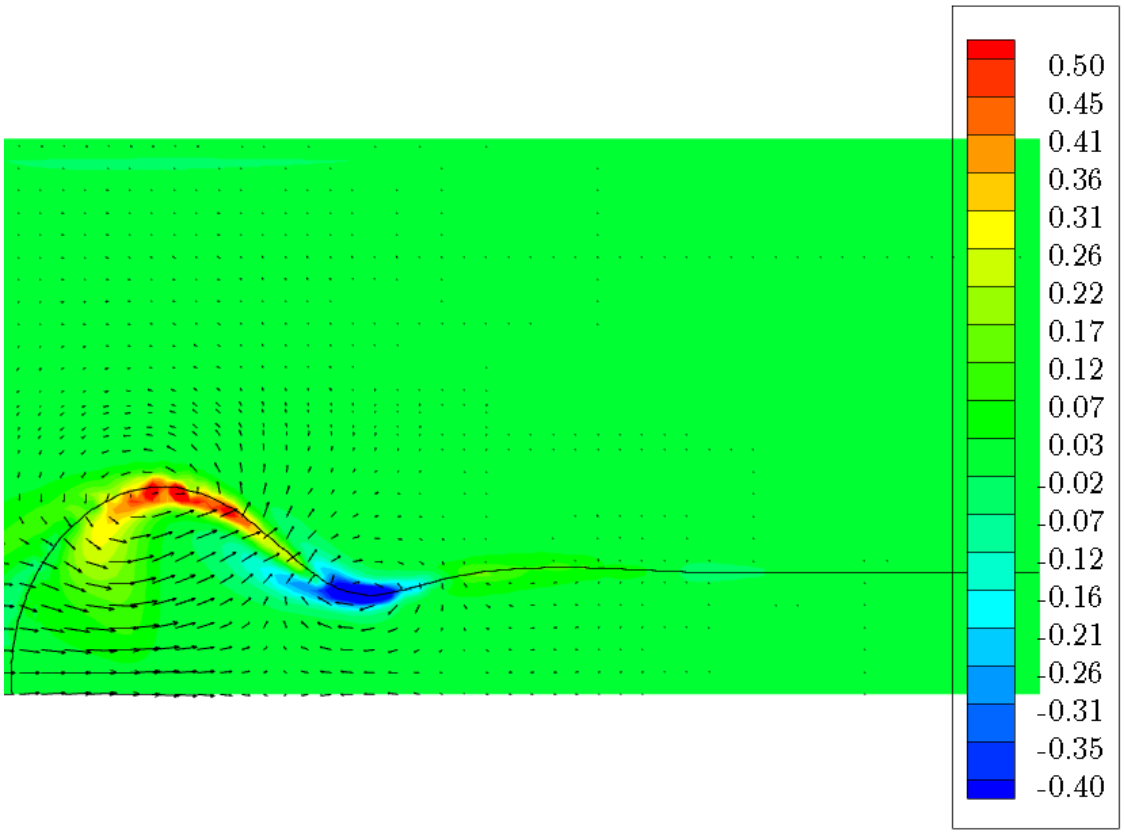

Figure 5.16: Vorticity distribution in the system at $Re_c = 100$ and $\lambda = 1.00$ before attainment of minimum neck radius. Regions of opposite signed vortices can be seen.

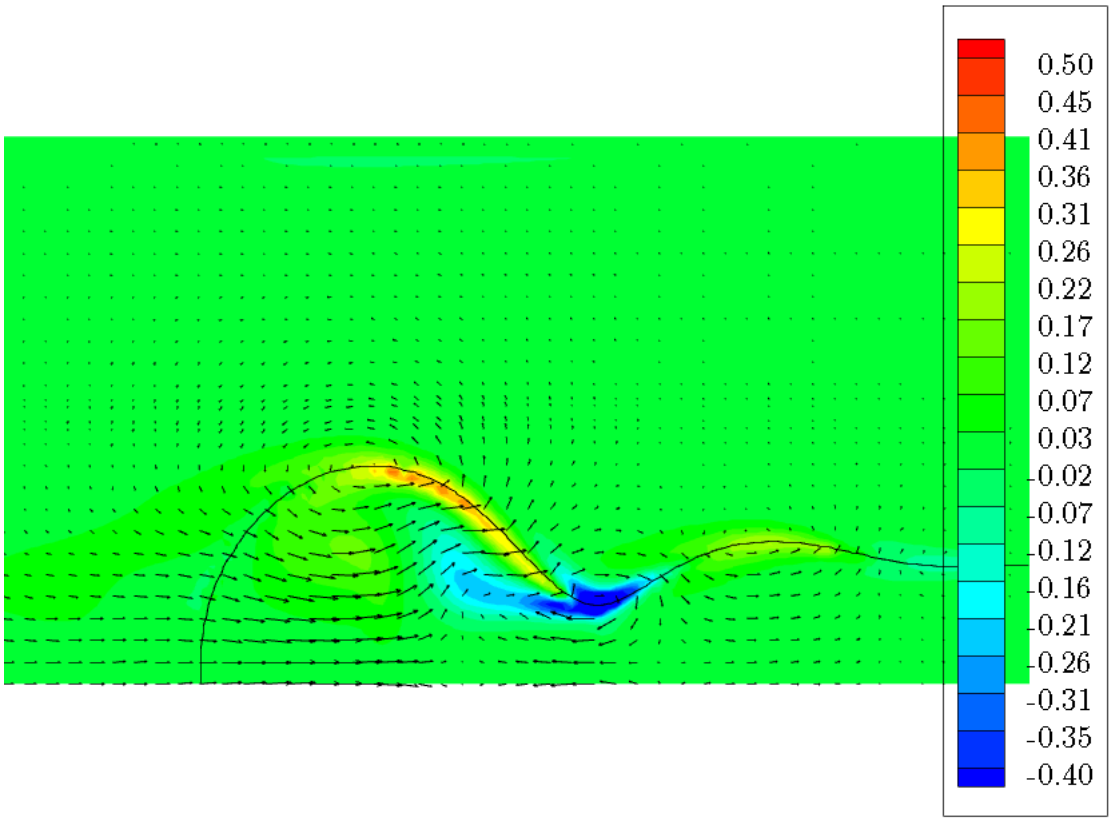

Figure 5.17: Vorticity distribution in the system at $Re_c = 100$ and $\lambda = 1.00$ at minimum neck radius. Onset of the separation of the jet flow from the neck to the bulb can be observed.

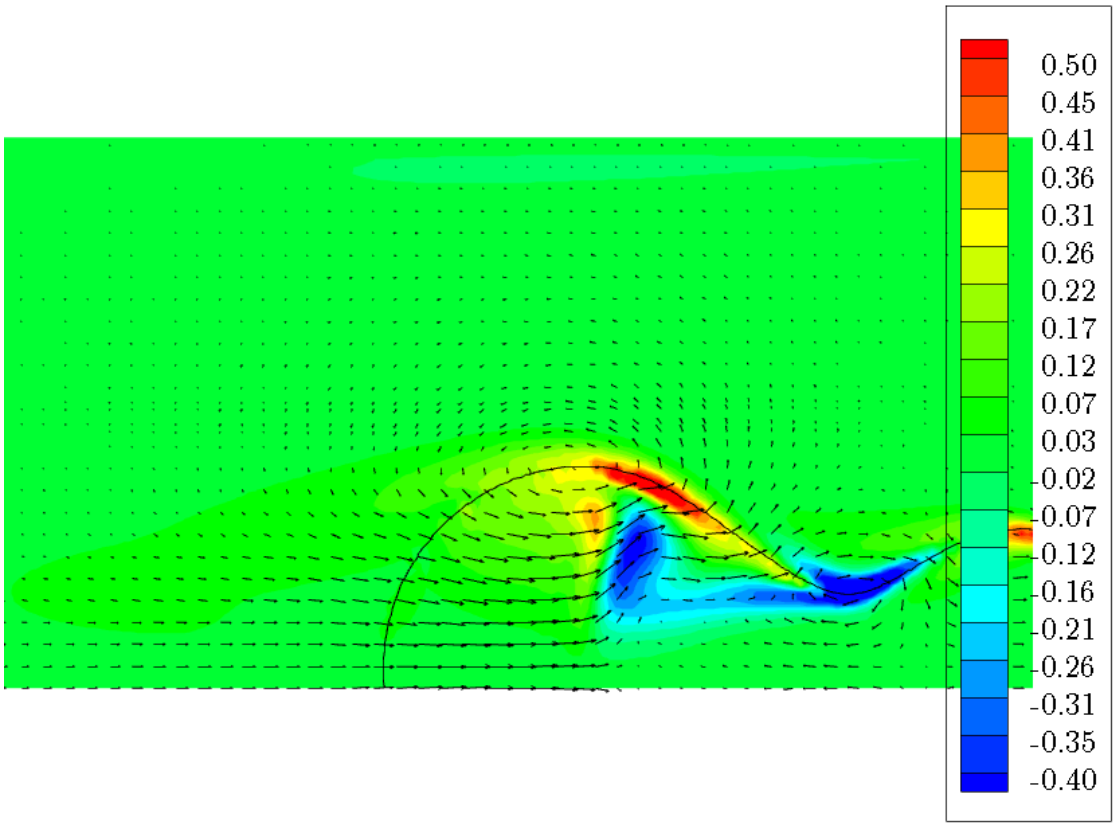

Figure 5.18: Vorticity distribution in the system at $Re_c = 100$ and $\lambda = 1.00$ after reopening of the neck. A prominent vortex ring can be seen persisting in the bulb.

A simple description of the dynamics as explained by Hoepffner and Paré [14] for a drop suspended in air can be applied to study the system. As the bulb retracted and neck radius reduced, fluid accelerated from the central portion of the slender drop into the bulb through the neck. As it accelerated, it did not recover all of the upstream pressure and the flow separated from the wall of the bulb downstream. Since the pressure was not fully recovered, the bulb was unable to withstand the capillary pressure and fluid was expelled back into the neck – causing neck to reopen. Examining the vorticity inside the bulb in figure 5.18, we observed a vortex ring whose formation – as reported by Hoepffner and Paré [14] – was critical to the neck

reopening phenomenon.

In figures 5.16 and 5.17, we also observed a narrow band of vorticity persisting at the interface with the opposite sign as the main vortex ring. This region of vorticity supported the formation of the vortex ring which in turn contributed to the neck reopening phenomenon. We realized that the diffusion of this region of vorticity would then hinder the neck reopening and allow for the recovery of the monotonic pinching. Indeed, examining a monotonic pinching at $Re_c = 100$ and $\lambda = 0.01$, we observe that raising the viscosity of the outside fluid at the same Reynolds number diffuses the vorticity in the system. Figure 5.19 shows the vorticity distribution associated with monotonic end pinching.

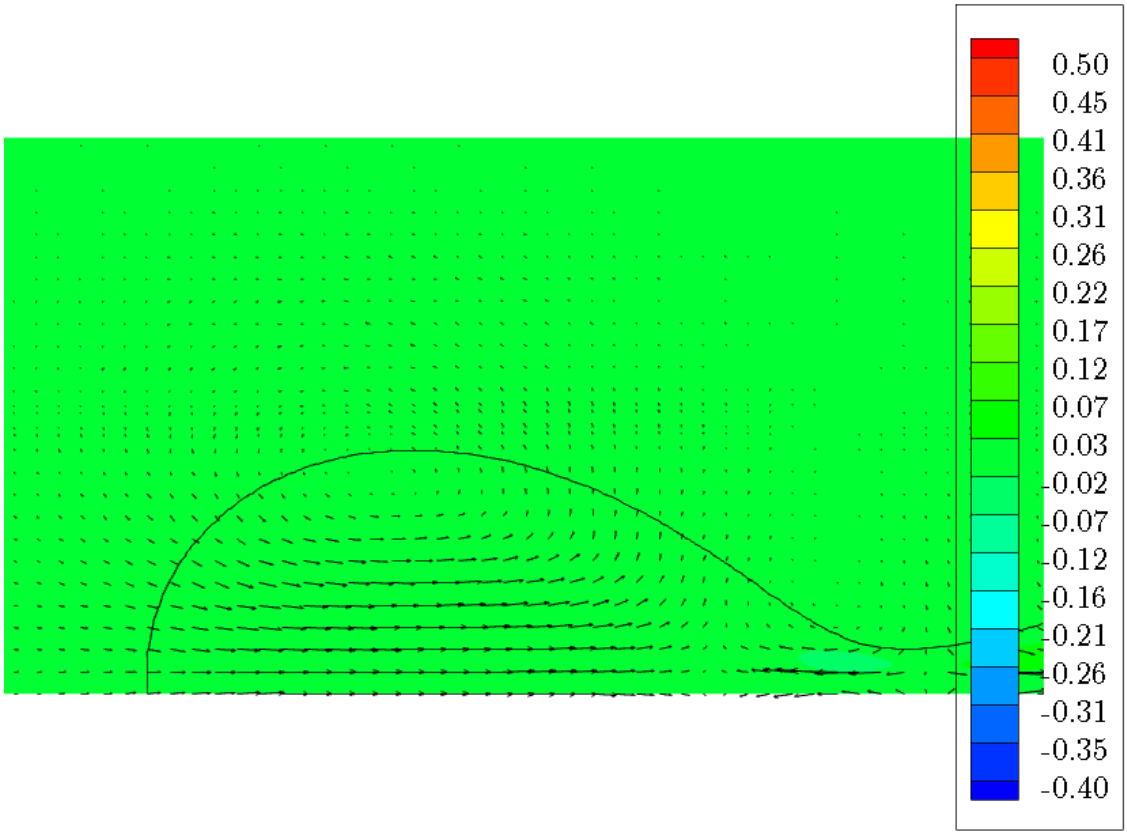

Figure 5.19: Vorticity distribution in the system just before monotonic pinch-off of the neck. Note that vorticity is diffused and no concentrated vortex rings are observed.

It is evident from figure 5.19 that the large viscosity of the surrounding fluid helped diffuse the vorticity in the system. When the viscosity of the external fluid was large, vorticity was able to diffuse across the interface leading to a diminished and almost non-existent vortex ring (see [104, 105] for a description of vorticity transport across a flexible interface). This did not allow the neck to reopen and the neck radius monotonically reduced to zero. The effect of vorticity diffusion was also implicit in the fact that the bulb motion through the high viscous fluid was difficult.

5.5 Conclusion

This study was an attempt to uncover the dynamics behind drop deformation and breakup in inertial systems. Most mixing processes in industries occur at large Reynolds number and this study unveiled the behavior of drops in such systems. Specifically, we investigated inertial effects on deforming drops using direct numerical simulations and validated it with previous results from both stagnant and non-stagnant extensional flows.

Subsequently, we studied the capillary-driven breakup of slender drops suspended in a quiescent fluid. This problem was a natural extension of the previous study where breakup of elongated drops was desired. While interfacial tension can be used to drive the flow that breaks up drops, it is unclear how the effect works in conjunction with viscous and inertial forces in the system. To address this issue, we investigated capillary-driven breakup in a previously unexplored part of the parametric space where viscosity of the outer fluid either supported or hindered breakup of drops. Such problems are also common in industries where transient capillary flows are used to dispersively mix drops within a fluid. In this study, we thoroughly explained the effect of surrounding fluid at various Reynolds numbers and rationalized the role of the three competing forces in the system. We presented a stability diagram for drops in the new parametric space which can be useful guide to industries during mixing process design. Experimental evidence will lead more weightage to our findings and is a natural area for future study.

Appendix A: Supplementary material to chapter 3

A.1 Numerical simulation in ANSYS FLUENT

The geometry for the simulation consisted of the three dimensional flow channel depicted in Fig. A.1 where fluid flow is streamwise along x in the direction of gravity. We discretized the entire three dimensional domain using 179,080 hexahedral elements.

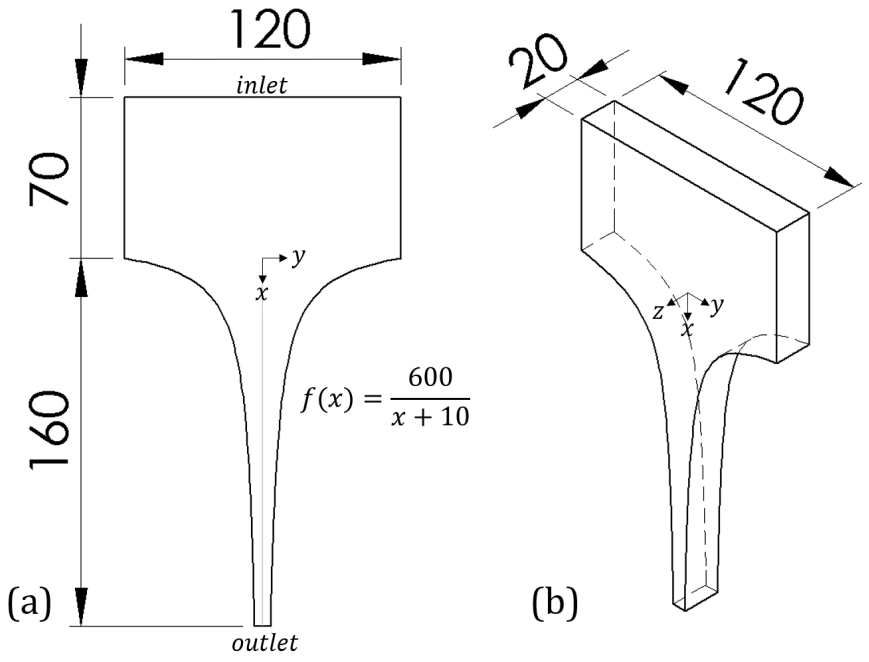

Figure A.1: (a) Front view and (b) isometric view of a planar channel with flow streamwise along x. The flow domain was discretized into 179,080 hexahedral elements.

Since the objective was to replicate experimental conditions, we performed the numerical simulation of the flow for the highest achievable inlet speed of $8\,\mathrm{mm\,s^{-1}}$. A small gauge pressure at the outlet was applied to prevent outflow of fluid under stationary conditions. The pertinent boundary conditions for the flow were as follows. At the inlet, a fixed velocity of $8\,\mathrm{mm\,s^{-1}}$ was applied. At the outlet, a small guage pressure of 1764 Pa was maintained to replicate the experimental condition. No-slip boundary condition for velocity was imposed along the channel walls.

A.1.1 Specifications of numerical solver

On the discretized geometry, we used a pressure-based solver to the integral form of the time dependent governing equations of the incompressible flow available as an option in ANSYS FLUENT. The pressure-velocity coupled scheme and spatial discretization of pressure at second order was chosen. We used the second order upwinding for momentum and an absolute convergence criteria of 1×10^{-4} for all residuals. The time step size was $5 \times 10^{-4}\,\mathrm{s}$ for the transient simulation.

A.1.2 Results and verification

The transient simulation solved the flow at every time step and we tracked the x component of velocity along the line joining (0, 0, 0) and (160 mm, 0, 0). We refer to this line as the centerline of the flow where, due to the symmetry in the channel, the y and z components of velocity are zero. Fig. A.2 shows the evolution of the non dimensional velocity $\tilde{u}$ along the centerline $\tilde{x}$ at various time steps starting from an

initial state of no motion. Velocity and streamwise distance are non dimensionalized as

$$u = \frac{Q}{h^2}\tilde{u} \tag{A.1}$$

and

$$x = \lambda\tilde{x} \tag{A.2}$$

out of which a non dimensional time scale arises. Q is the flow rate, $h = 10\,\text{mm}$, and $\lambda = 160\,\text{mm}$. Fig. A.2 shows that the flow becomes fully developed in a very short time scale that is much smaller than the time scale where a suspended phase can feel the effect of the outer flow and start translating. Since the simulation was performed at the highest achievable inlet speed in our experiments, we concluded that the Reynolds number for lower inlet speeds will be much smaller and the flow will develop almost instantaneously. Hence we chose to perform, and verify, steady state simulations for the flow with the assumption that transient effects on suspended particles were negligible.

To verify the results from the simulation, we performed a grid independence study by decreasing the number of elements to 23,544 since the original number of elements in the domain - 179,080 - was deemed too high. Fig. A.3 shows the identical results from the grid independence study for a steady state flow at different levels of discretization which verifies our original choice.

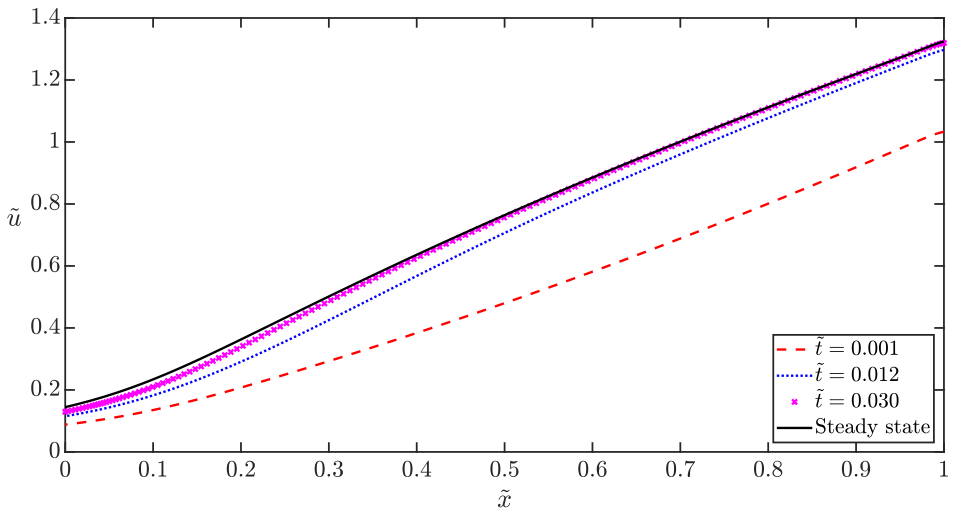

Figure A.2: Non dimensional velocity of the flow $\tilde{u}$ along the centerline $\tilde{x}$ at various non dimensional timesteps. The time is non dimensionalized using the velocity and length scale. Flow rapidly develops to the steady state.

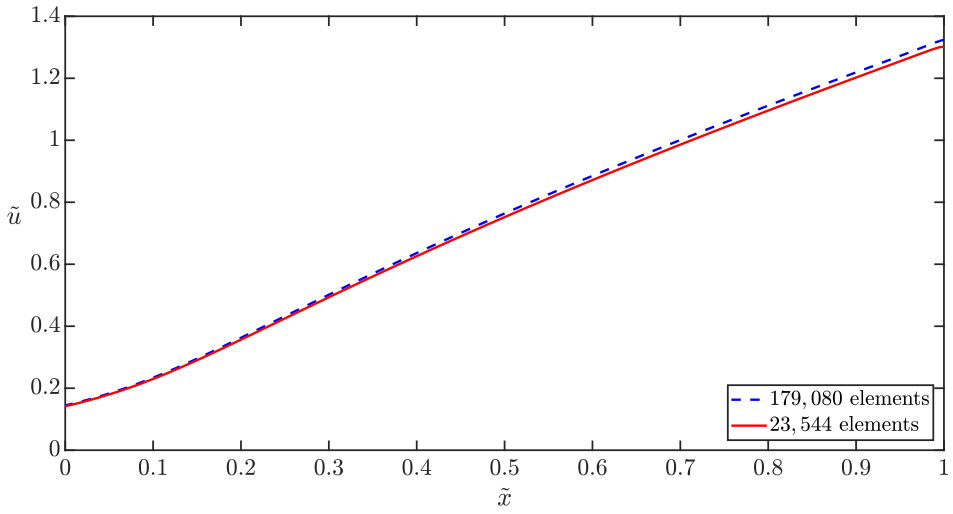

Figure A.3: Streamwise velocity along the centerline at two levels of flow domain discretization. Solid line represents 23,544 elements and dashed line represents 179,080 elements.

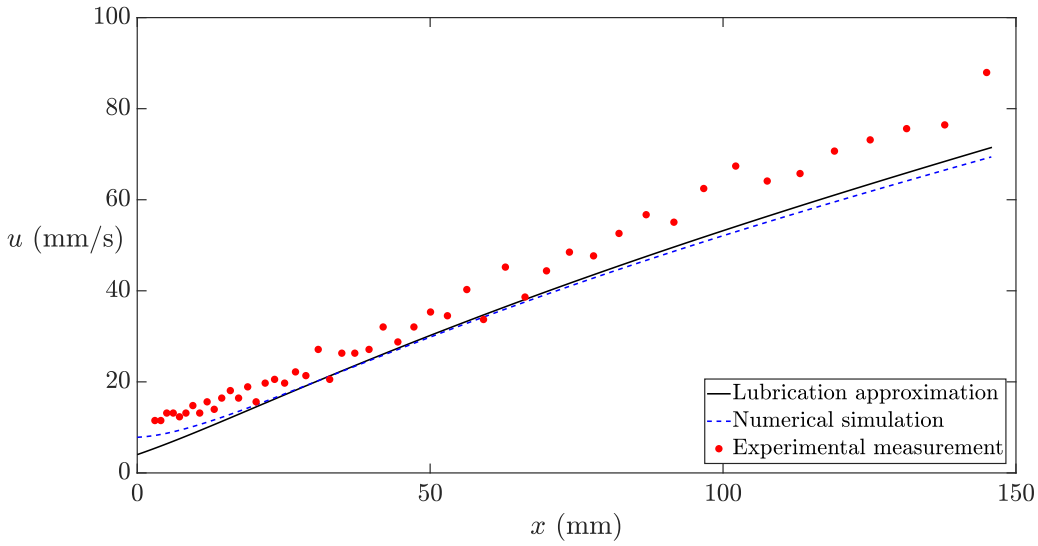

Figure A.4: Measurement of speed of tracer particle in a flow with inlet speed of $2.4\,\mathrm{mm\,s^{-1}}$

A.2 Raw experimental data

Experimental data for lubrication theory validation is shown in Fig. A.4 to Fig. A.6 and measurements of droplet speeds at various Capillary numbers is shown in Fig. A.7 to Fig. A.10. All plots use the coordinate system shown in Fig. A.1. The non-dimensional version of the data is presented in the main paper.

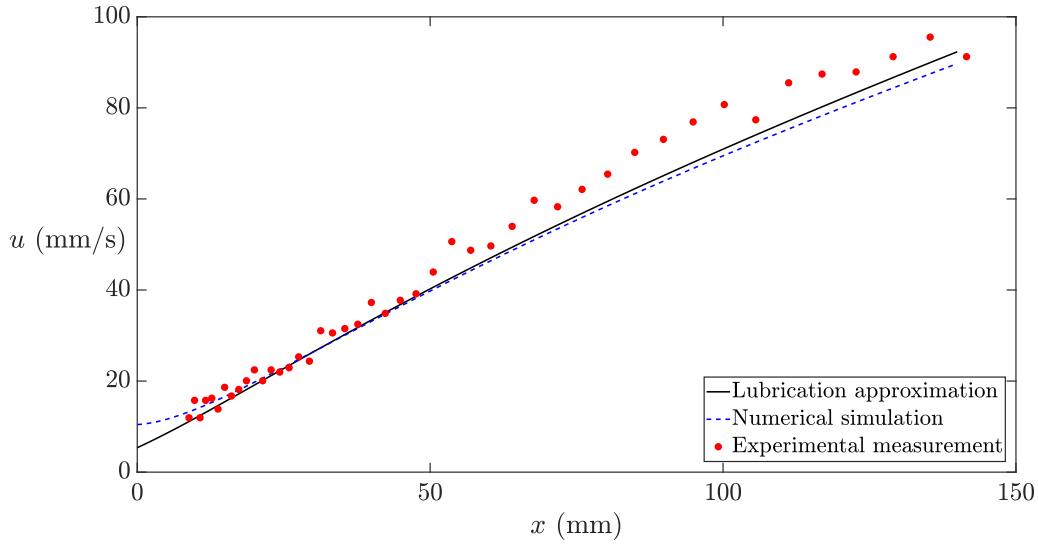

Figure A.5: Non-normalized data for speed of tracer particle in a flow with inlet speed of $3.2\,\mathrm{mm\,s^{-1}}$

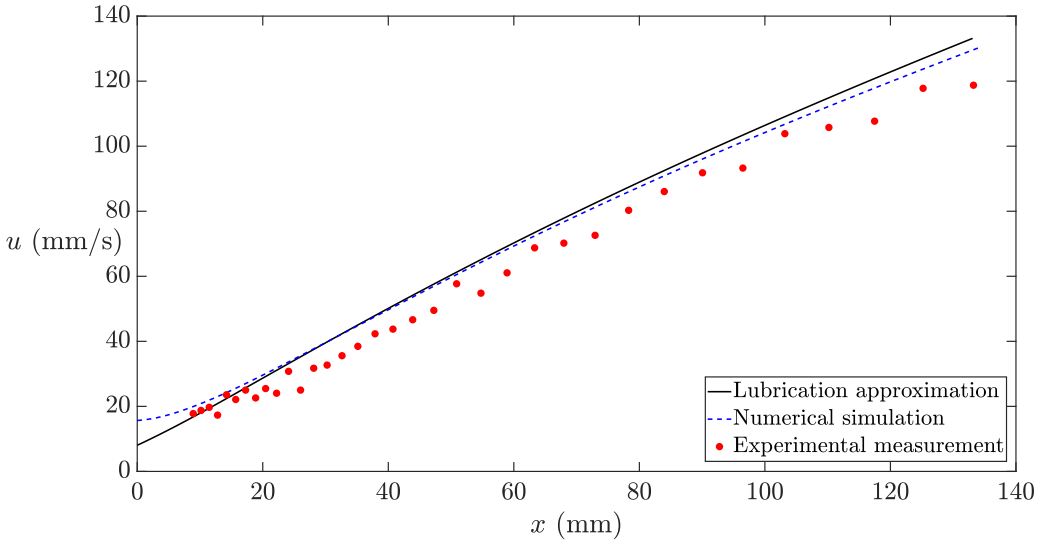

Figure A.6: Non-normalized data for speed of tracer particle in a flow with inlet speed of $4.8\,\mathrm{mm\,s^{-1}}$

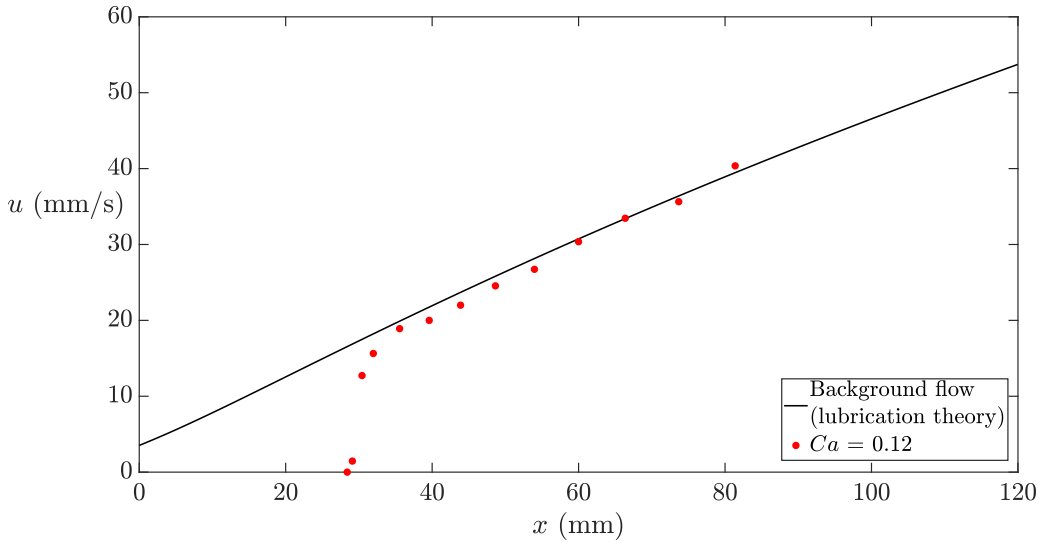

Figure A.7: Speed of droplet with initial Capillary number of 0.12 compared with the lubrication theory prediction.

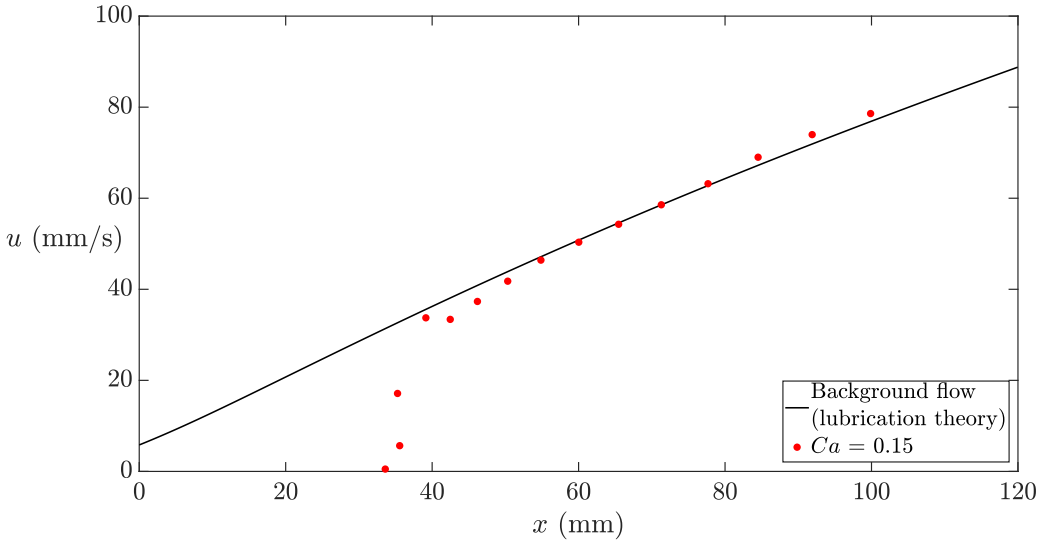

Figure A.8: Speed of droplet with initial Capillary number of 0.15 compared with the lubrication theory prediction.

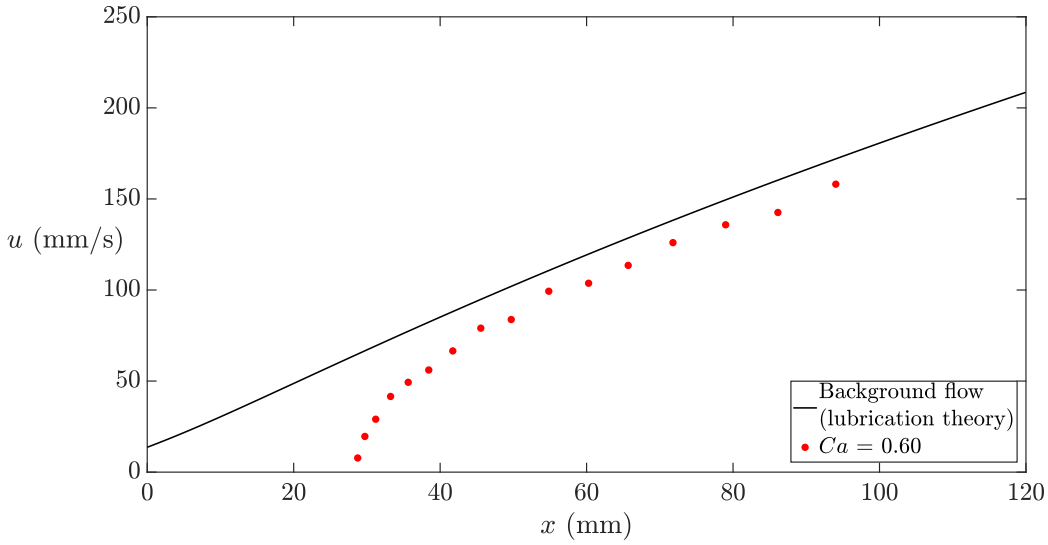

Figure A.9: Speed of droplet with initial Capillary number of 0.60 compared with the lubrication theory prediction.

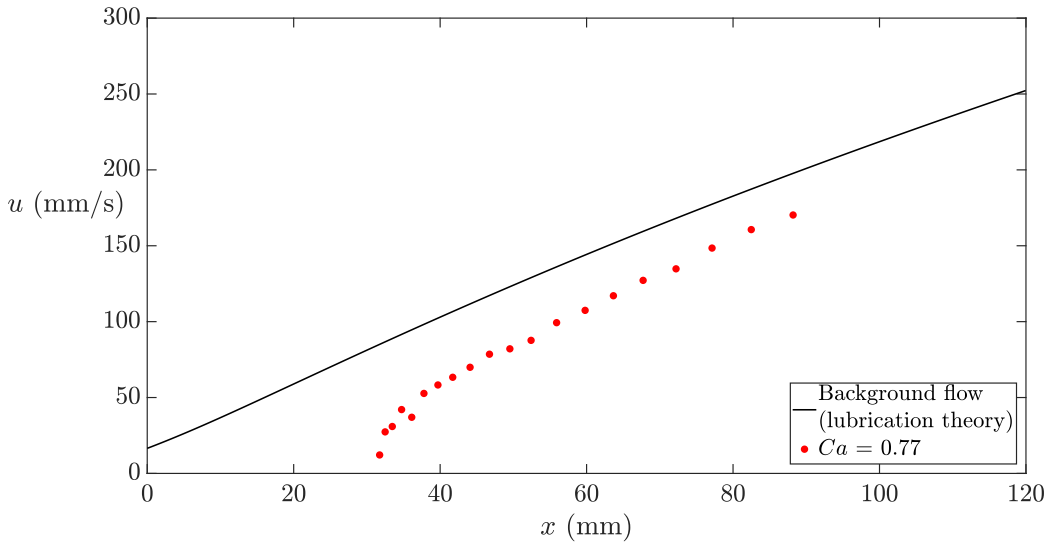

Figure A.10: Speed of droplet with initial Capillary number of 0.77 compared with the lubrication theory prediction.

Appendix B: Supplementary material to chapter 5

B.1 Grid independence study

For the capillary-driven breakup problem, verifying grid independence was important to ensure validity of the numerical results. A sample case is illustrated here to establish the validity of the results. We considered a case ($Re_c = 50$ and $\lambda = 0.10$) where the capillary-driven flow produced an asymptotically unstable state. Two levels of domain discretization – 980 X 70 and 1176 X 84 – was performed and the RMS velocity of the flow was tracked. The latter discretization represents the resolution used for all results reported in this study. Figure B.1 establishes grid independence where nearly the same RMS velocity was observed for both levels of discretization.

B.2 Inertial effect on breakup of slender drop in [1]

To provide some context to the results discussed in chapter 5, results from Stone et al. [1] can be explored in the new part of the parametric space by varying the level of inertia in the system. Figure B.2 shows the initial configuration from the study by Stone et al. [1]. To this system, various levels of inertia is added and

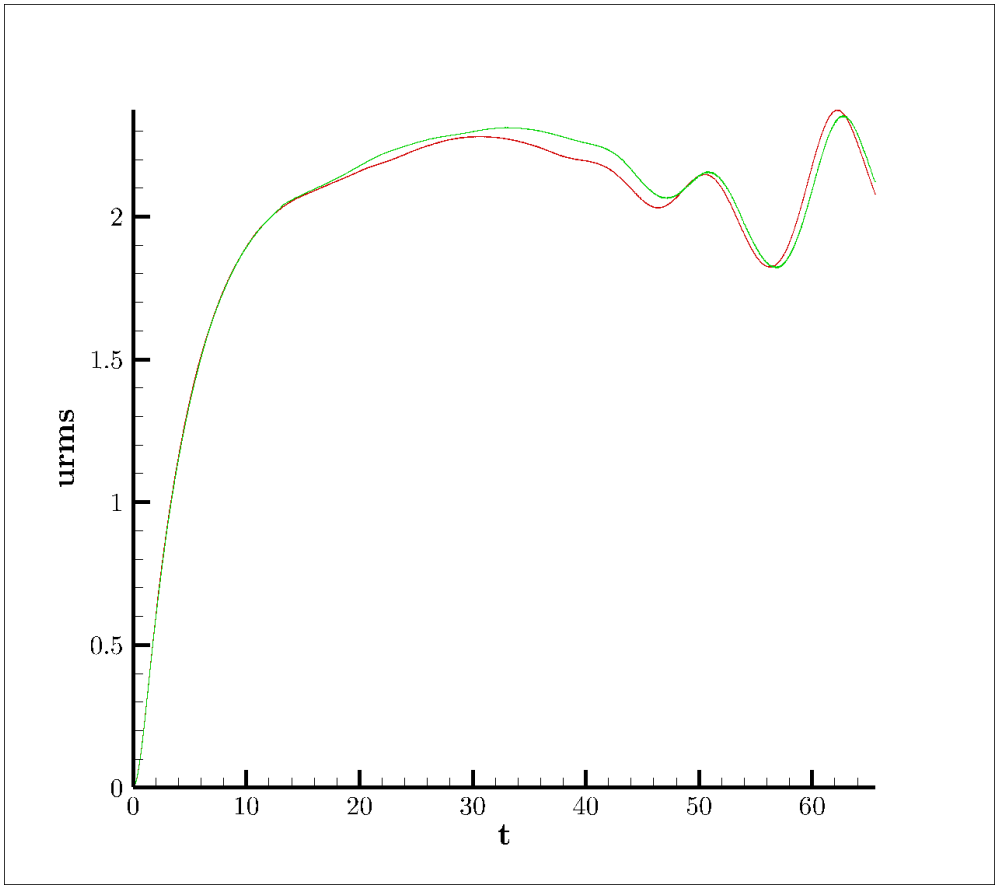

Figure B.1: RMS velocity in the domain at $Re_c = 50$ and $\lambda = 0.10$ for two levels of domain discretization. Red is at 1176 X 84 resolution and green is at 980 X 70.

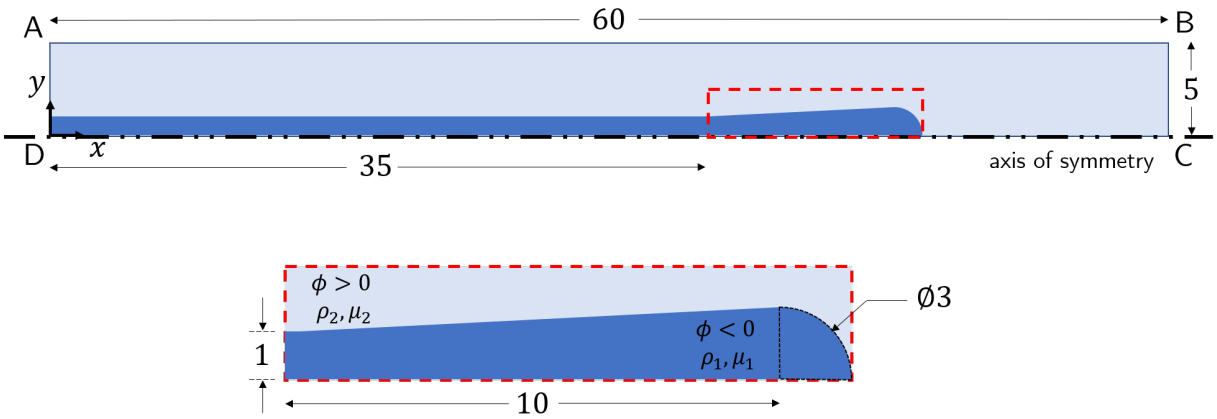

Figure B.2: Initial configuration for the capillary-driven flow problem in [1]

the drop behavior is tracked.

At $Re_c \to 0$ and $\lambda = 0.05$, Stone et al. [1] studied the retraction of the slender drop formed in a four-roll mill. When the external flow was stopped, the bulb at the ends started to increase in radius and traverse towards the center of the slender drop. However, this motion of the bulb was hindered because the outside fluid was highly viscous. Since the ends of the drop could not retract, a neck – defined as the section with minimum radius – was formed and resulted in pinch-off. Figure B.3 shows the development of the capillary flow that resulted in the creation of six daughter drops. Each daughter drop was formed successively in a phenomenon known as retractive end pinching. In this section, we report several attributes of this capillary flow by considering the effect of inertia which has largely been neglected in previous studies. The development of the capillary flow for the same slender drop at $Re_c = 100$ is shown in figure B.4.

The two ends of the slender drops shown in figure B.4 were initially drawn towards each other by a strong capillary flow that tried to minimize the interfacial

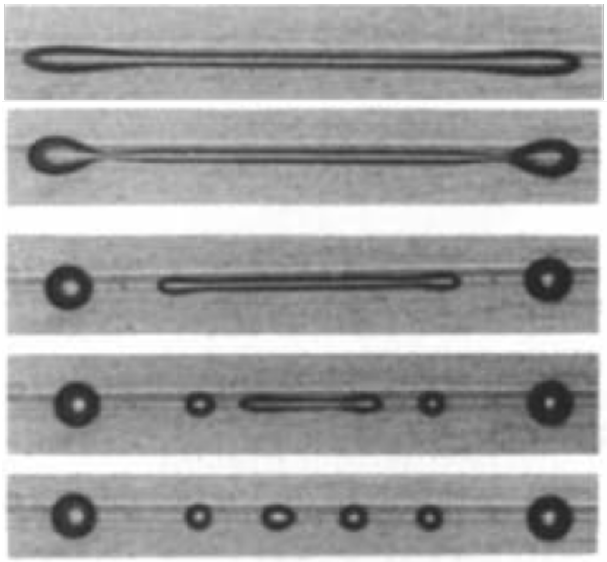

Figure B.3: Capillary-driven breakup in a slender drop at $R_c \to 0$ and $\lambda = 0.05$. Figure is reproduced from Stone et al. [1] with permission.

area. The radius of the bulb at the end increased and a neck was formed. Pinch-off was defined as the instant where the neck radius became zero. However, the radius of the neck did not reach zero monotonically. After attaining a local minimum, the neck reopened and the radius at the neck increased. Pinch-off was postponed to a later time which resulted in the formation of daughter drops. From figure B.4, it can be seen that at $Re_c = 100$, five daughter drops were formed. The reopening of the neck happened twice in the case of $Re_c = 250$ and $Re_c = 500$. However, the consequence of the neck reopening with increasing Reynolds numbers resulted in completely different final distributions of daughter drops as shown in figures B.5 and B.6.

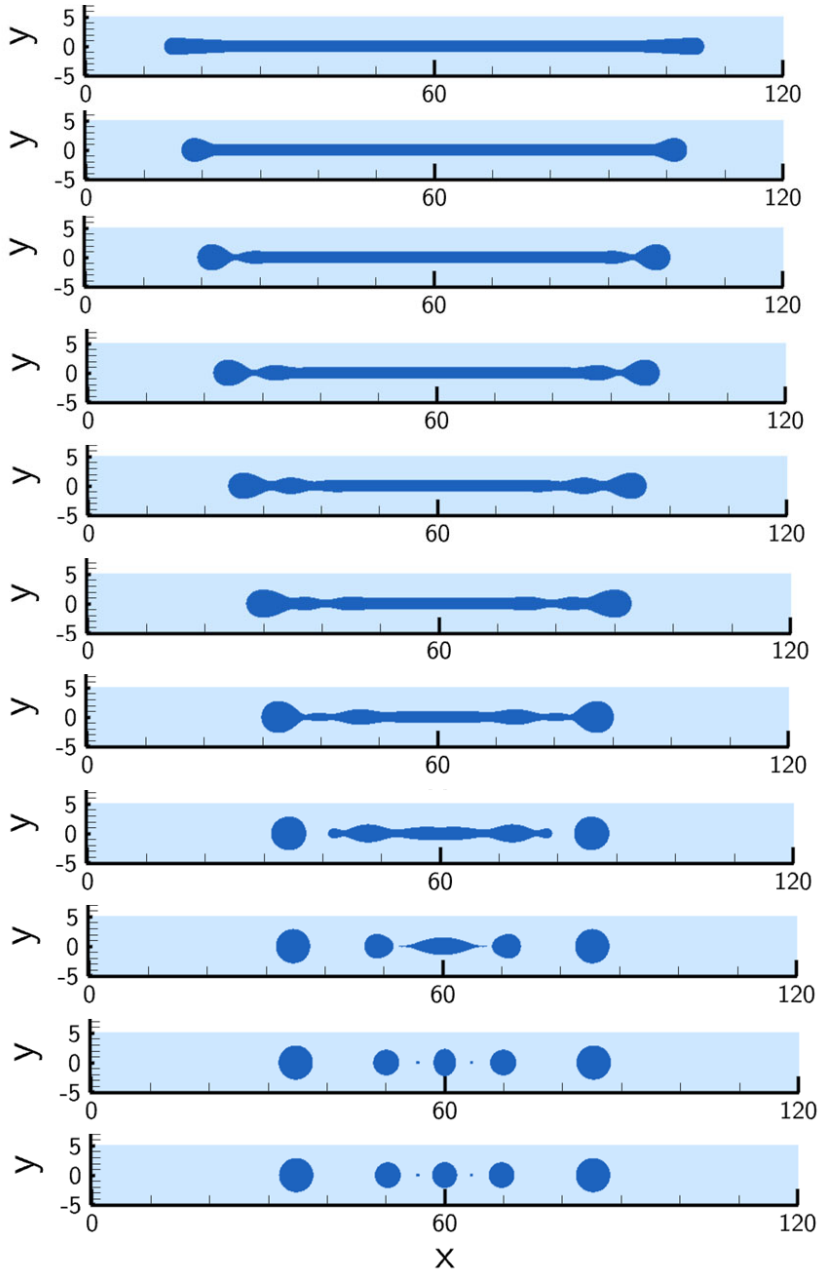

Figure B.4: (a) to (k) show the capillary-driven breakup in a slender drop at $Re_c = 100$ and $\lambda = 0.05$. Comparing with figure at $Re_c \to 0$, only five daughter drops were obtained at steady state (k).

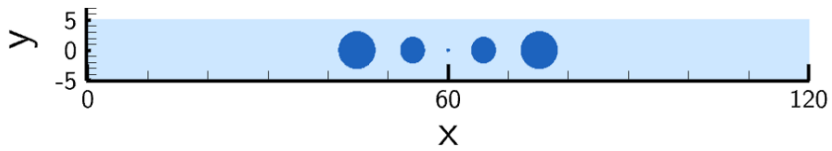

Figure B.5: Steady state after capillary-driven breakup at $Re_c = 250$ and $\lambda = 0.05$ producing four daughter drops.

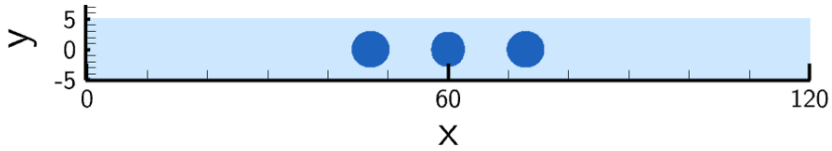

Figure B.6: Steady state after capillary-driven breakup at $Re_c = 500$ and $\lambda = 0.05$ producing three daughter drops.

B.3 Influence of the end-shape on capillary-driven flow

The shape of the ends of the slender drop has an effect on the capillary-driven flow. The effect can be rationalized with a simple description. When the radius of the end of the drop is large, the curvature is small and thus the magnitude of interfacial force driving the flow is small. Large bulbs thus weakly drive the capillary flow and bulb pinch-off becomes more likely. The opposite effect occurs when the radius of the bulb is small. The flow is strongly dominated by interfacial force leading to the system preferring coalescence instead of end-pinch.

Consider the case of the capillary-driven flow in a slender drop with $Re_c = 50$ and $\lambda = 0.10$. In chapter 5, it was shown that this condition leads to an asymptotically unstable end state where two daughter drops were formed. In this section, we will show how changing the shape of the end for the same flow parameters will result in a completely different configuration at the end.

To this end, consider an artificially imposed shape of the end as shown in figure

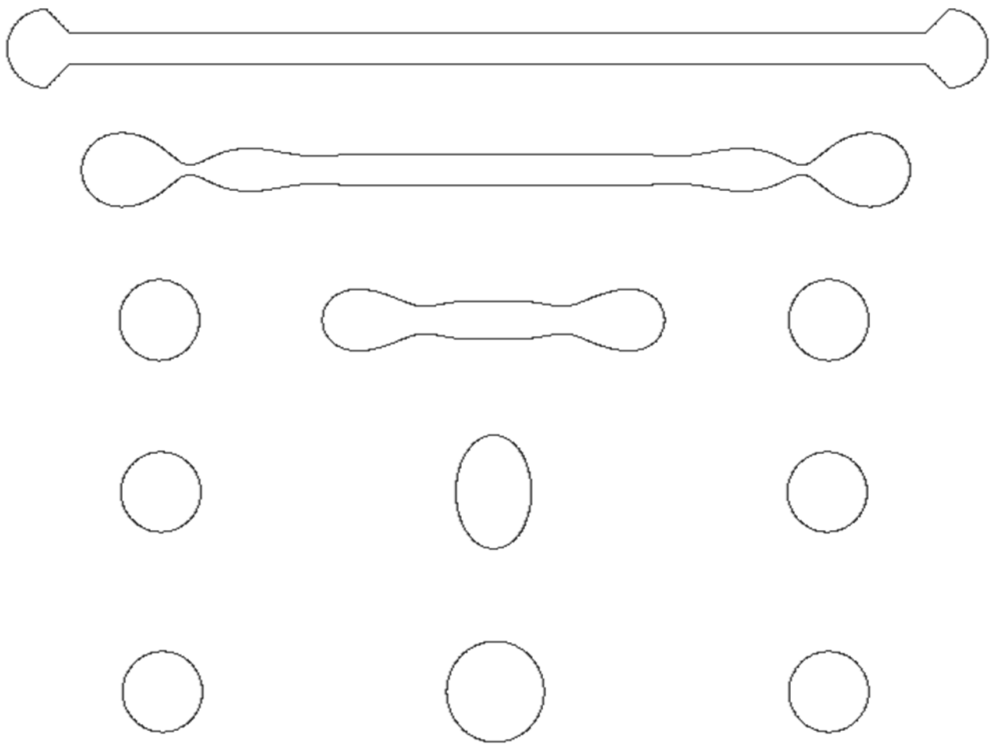

Figure B.7: Transient flow in a slender drop with a large radius of curvature near the tips.

B.7. The bulb has a radius equal 2.5 times than the slender stem. Analyzing the transient flow in figure B.7 reveals that the heavy bulb pinches off from the stem very early and the steady state configuration yielded three daughter drops.

B.4 Non-trivial breakup modes under large inertia

Inertial effects can result in non-trivial behavior of slender drops that is completely different from behavior at low Reynolds number. In this section we report two such observations and discuss the mechanism.

B.4.1 Entrapment of surrounding fluid

Consider a slender drop with aspect ratio = 10 in a system with $\lambda = 1.00$. When inertial effects are considered – i.e. setting $Re_c = 50$ – in the capillary-driven flow, we observed that the drop was conditionally unstable and asymptotically stable. The drop underwent breakage at the middle and the two bulbs merged together to form a stable drop. The mechanism was discussed in chapter 5 but here we report a non-trivial behavior where the surrounding phase gets entrapped into the drop. Figure B.8 shows the transient behavior of the drop and the phase entrapment.

B.4.2 Torus formation

The parametric space shown in chapter 5 can be extended for $\lambda > 1.00$. In this part of the parametric space, viscous effects from the surrounding fluid are less important than the inertia associated with the capillary-driven flow. This causes an interesting behavior where tori start to form in the transient flow. We investigated this at $\lambda = 100$ and $Re_c = 100$ for a slender drop with aspect ratio = 30. Figure B.9 shows the formation of a torus after the bulbs pinch off.

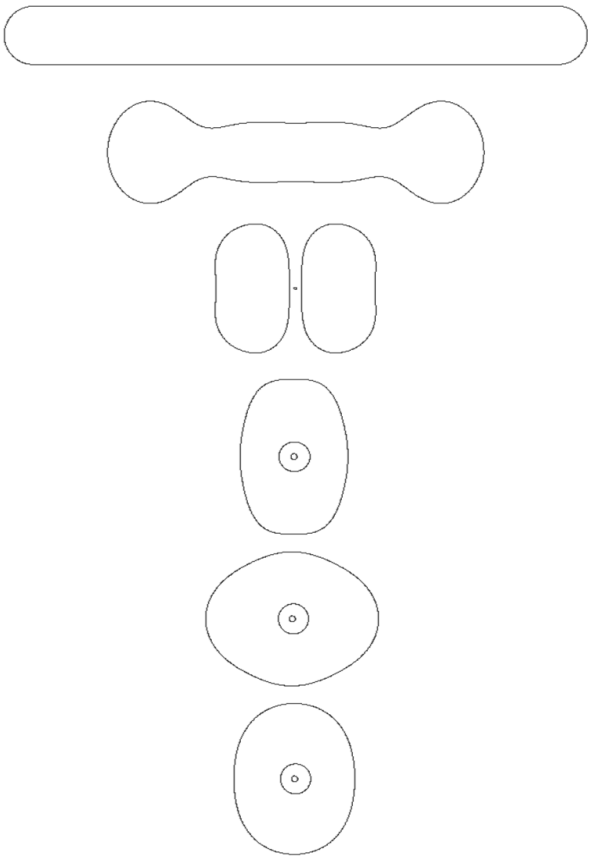

Figure B.8: Inertial capillary flow in a slender drop with aspect ratio = 10 resulting in entrapment of the surrounding phase.

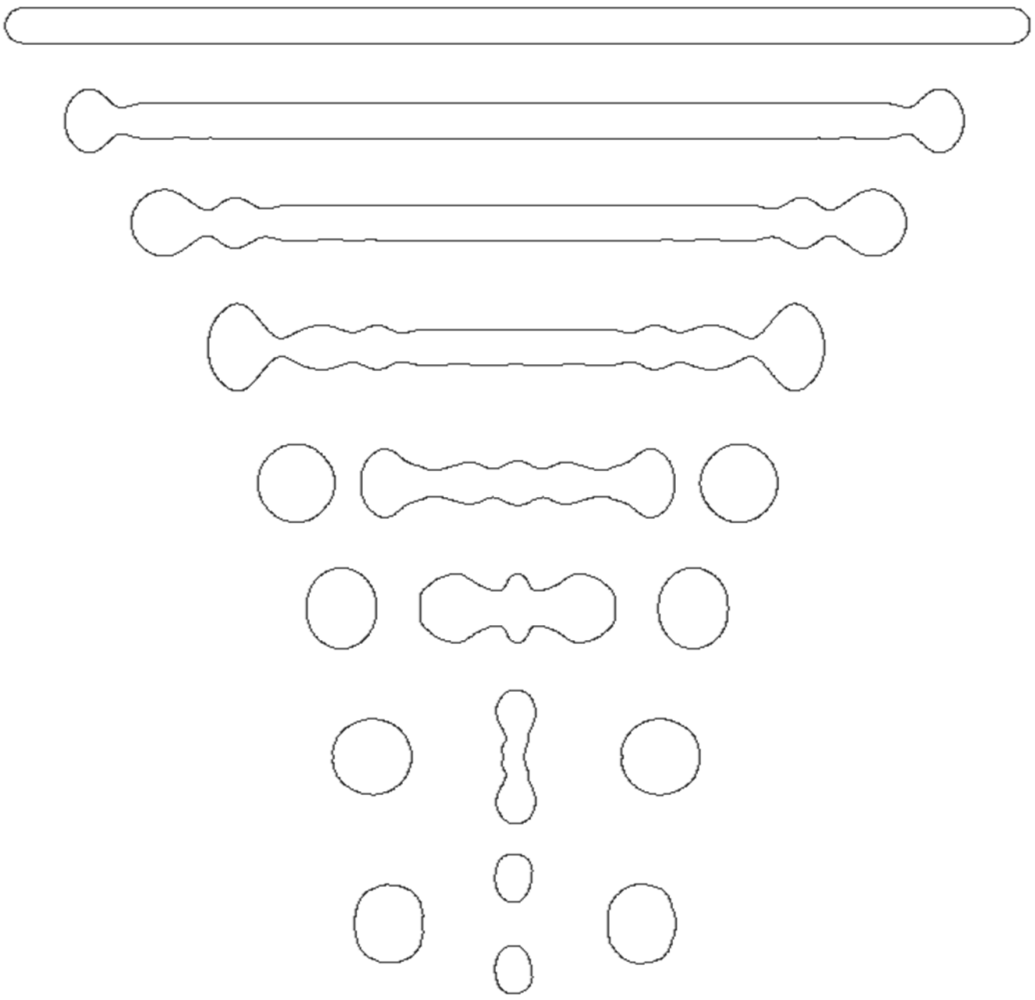

Figure B.9: Formation of a torus structure in the transient flow. In the bottom frame, the torus is surrounded by two daughter drops. The initial slender drop had an aspect ratio = 30. For the inertial-capillary flow, $Re_c = 100$ and $\lambda = 100$.

Bibliography

[1] H. A. Stone, B. J. Bentley, and L. G. Leal. An experimental study of transient effects in the breakup of viscous drops. *Journal of Fluid Mechanics*, 173:131–158, December 1986.

[2] B. J. Bentley and L. G. Leal. An experimental investigation of drop deformation and breakup in steady, two-dimensional linear flows. *Journal of Fluid Mechanics*, 167:241–283, June 1986.

[3] F. Wang, F. P. Contò, N. Naz, J. R. Castrejón-Pita, A. A. Castrejón-Pita, C. G. Bailey, W. Wang, J. J. Feng, and Y. Sui. A fate-alternating transitional regime in contracting liquid filaments. *Journal of Fluid Mechanics*, 860:640–653, February 2019.

[4] G. I. Taylor. The Formation of Emulsions in Definable Fields of Flow. *Proceedings of the Royal Society of London. Series A, Containing Papers of a Mathematical and Physical Character*, 146(858):501–523, 1934.

[5] Harold P. Grace. Dispersion Phenomena in High Viscosity Immiscible Fluid Systems and Application of Static Mixers as Dispersion Devices in Such Systems. *Chemical Engineering Communications*, 14(3-6):225–277, March 1982.

[6] Yvonne W. Stegeman, Frans N. Van De Vosse, and Han E. H. Meijer. On the Applicability of the Grace Curve in Practical Mixing Operations. *The Canadian Journal of Chemical Engineering*, 80(4):1–6, August 2002.

[7] Eric Lauga, Abraham D. Stroock, and Howard A. Stone. Three-dimensional flows in slowly varying planar geometries. *Physics of Fluids*, 16(8):3051–3062, July 2004.

[8] L. Gary Leal. *Advanced Transport Phenomena: Fluid Mechanics and Convective Transport Processes*. Cambridge University Press, June 2007.

[9] H. A. Stone and L. G. Leal. Relaxation and breakup of an initially extended drop in an otherwise quiescent fluid. *Journal of Fluid Mechanics*, 198:399–427, January 1989.

[10] Patrick K. Notz and Osman A. Basaran. Dynamics and breakup of a contracting liquid filament. *Journal of Fluid Mechanics*, 512:223–256, August 2004.

[11] Jens Eggers and Marco A. Fontelos. Isolated inertialess drops cannot break up. *Journal of Fluid Mechanics*, 530:177–180, May 2005.

[12] Alfonso A. Castrejón-Pita, J. R. Castrejón-Pita, and I. M. Hutchings. Breakup of Liquid Filaments. *Physical Review Letters*, 108(7):074506, February 2012.

[13] Theo Driessen, Roger Jeurissen, Herman Wijshoff, Federico Toschi, and Detlef Lohse. Stability of viscous long liquid filaments. *Physics of Fluids*, 25(6):062109, June 2013.

[14] Jérôme Hoepffner and Gounséti Paré. Recoil of a liquid filament: escape from pinch-off through creation of a vortex ring. *Journal of Fluid Mechanics*, 734:183–197, November 2013.

[15] Francesco Paolo Contò, Juan F. Marín, Arnaud Antkowiak, J. Rafael Castrejón-Pita, and Leonardo Gordillo. Shape of a recoiling liquid filament. *Scientific Reports*, 9(1):15488, October 2019.

[16] Aditya N. Sangli and David I. Bigio. Velocity of suspended fluid particles in a low Reynolds number converging flow. *Physics of Fluids*, 33(1):013316, January 2021.

[17] J. A Depree and G. P Savage. Physical and flavour stability of mayonnaise. *Trends in Food Science & Technology*, 12(5):157–163, May 2001.

[18] Jose Maria Franco, Antonio Guerrero, and Crispulo Gallegos. Rheology and processing of salad dressing emulsions. *Rheologica Acta*, 34(6):513–524, November 1995.

[19] M. Kowalska, M. Ziomek, and A. Żbikowska. Stability of cosmetic emulsion containing different amount of hemp oil. *International Journal of Cosmetic Science*, 37(4), 2015.

[20] R. Lambourne and T. A. Strivens. *Paint and Surface Coatings: Theory and Practice*. Elsevier, August 1999.

[21] Timo Vesikari, Markus Knuf, Peter Wutzler, Aino Karvonen, Dorothee Kieninger-Baum, Heinz-Josef Schmitt, Frank Baehner, Astrid Borkowski, Theodore F. Tsai, and Ralf Clemens. Oil-in-Water Emulsion Adjuvant with Influenza Vaccine in Young Children. *New England Journal of Medicine*, 365(15), October 2011.

[22] Andreas Acrivos. The Breakup of Small Drops and Bubbles in Shear Flows*. *Annals of the New York Academy of Sciences*, 404(1):1–11, May 1983.

[23] J. M. Rallison. The Deformation of Small Viscous Drops and Bubbles in Shear Flows. *Annual Review of Fluid Mechanics*, 16(1):45–66, 1984.

[24] H. A. Stone. Dynamics of Drop Deformation and Breakup in Viscous Fluids. *Annual Review of Fluid Mechanics*, 26(1):65–102, 1994.

[25] G. I. Taylor. The viscosity of a fluid containing small drops of another fluid. *Proc. R. Soc. Lond. A*, 138(834):41–48, October 1932.

[26] R. G. Cox. The deformation of a drop in a general time-dependent fluid flow. *Journal of Fluid Mechanics*, 37(3):601–623, July 1969.

[27] G. Hetsroni and S. Haber. The flow in and around a droplet or bubble submerged in an unbound arbitrary velocity field. *Rheologica Acta*, 9(4):488–496, November 1970.

[28] D. Barthès-Biesel and A. Acrivos. Deformation and burst of a liquid droplet freely suspended in a linear shear field. *Journal of Fluid Mechanics*, 61(1):1–22, October 1973.

[29] Andreas Acrivos and T. S. Lo. Deformation and breakup of a single slender drop in an extensional flow. *Journal of Fluid Mechanics*, 86(4):641–672, June 1978.

[30] E. J. Hinch and A. Acrivos. Long slender drops in a simple shear flow. *Journal of Fluid Mechanics*, 98(2):305–328, May 1980.

[31] Moshe Favelukis. A slender drop in a nonlinear extensional flow. *Journal of Fluid Mechanics*, 808:337–361, December 2016.

[32] J. M. Rallison and A. Acrivos. A numerical study of the deformation and burst of a viscous drop in an extensional flow. *Journal of Fluid Mechanics*, 89(1):191–200, November 1978.

[33] B. J. Bentley and L. G. Leal. A computer-controlled four-roll mill for investigations of particle and drop dynamics in two-dimensional linear shear flows. *Journal of Fluid Mechanics*, 167:219–240, June 1986.

[34] K. E. Spells. A Study of Circulation Patterns within Liquid Drops moving through a Liquid. *Proceedings of the Physical Society. Section B*, 65(7):541, 1952.

[35] R. R. Lagnado and L. G. Leal. Visualization of three-dimensional flow in a four-roll mill. *Experiments in Fluids*, 9(1-2):25–32, January 1990.

[36] C. Marks. *Drop breakup and deformation in sudden onset strong flows*. Doctor of Philosophy, University of Maryland, College Park, Maryland, 20740, USA, 1998.

[37] Jong-Wook Ha and L. Gary Leal. An experimental study of drop deformation and breakup in extensional flow at high capillary number. *Physics of Fluids*, 13(6):1568–1576, May 2001.

[38] Hong Bai Chin and Chang Dae Han. Studies on Droplet Deformation and Breakup. I. Droplet Deformation in Extensional Flow. *Journal of Rheology*, 23(5):557–590, October 1979.

[39] F. D. Godbille and J. J. C. Picot. Drop breakup in combined shear and extensional flow conditions. *Advances in Polymer Technology*, 19(1):14–21, January 2000.

[40] Luiz C. Wrobel, Delfim Soares, and Claire L. Das Bhaumik. Drop deformation in Stokes flow through converging channels. *Engineering Analysis with Boundary Elements*, 33(7):993–1000, July 2009.

[41] K. Feigl, F. X. Tanner, B. J. Edwards, and J. R. Collier. A numerical study of the measurement of elongational viscosity of polymeric fluids in a semihyperbolically converging die. *Journal of Non-Newtonian Fluid Mechanics*, 115(2):191–215, November 2003.

[42] Mónica S. Neves Oliveira, Manuel A. Alves, Fernando T. Pinho, and Gareth H. McKinley. Viscous flow through microfabricated hyperbolic contractions. *Experiments in Fluids*, 43(2-3):437–451, August 2007.

[43] Molly K. Mulligan and Jonathan P. Rothstein. The effect of confinement-induced shear on drop deformation and breakup in microfluidic extensional flows. *Physics of Fluids*, 23(2):022004, February 2011.

[44] Yanan Liu, Konstantinos Zografos, Joana Fidalgo, Charles Duchêne, Clément Quintard, Thierry Darnige, Vasco Filipe, Sylvain Huille, Olivia du Roure, Mónica S. N. Oliveira, and Anke Lindner. Optimised hyperbolic microchannels for the mechanical characterisation of bio-particles. *Soft Matter*, 16(43):9844–9856, November 2020.

[45] J. R. Pearson. *Mechanics of Polymer Processing*. Springer Science & Business Media, 1985.

[46] Xiangchun Xuan and Dongqing Li. Particle motions in low-Reynolds number pressure-driven flows through converging–diverging microchannels. *J. Micromech. Microeng.*, 16(1):62–69, December 2005.

[47] Ran Tao, Tiniao Ng, Yan Su, and Zhigang Li. A microfluidic rectifier for newtonian fluids using asymmetric converging–diverging microchannels. *Physics of Fluids*, 32(5):052010, 2020.

[48] Nazım Kurtulmuş, Harun Zontul, and Besir Sahin. Heat transfer and flow characteristics in a sinusoidally curved converging-diverging channel. *International Journal of Thermal Sciences*, 148:106163, 2020.

[49] Nnamdi Fidelis Okechi and Saleem Asghar. Fluid motion in a corrugated curved channel. *Eur. Phys. J. Plus*, 134(4):165, April 2019.

[50] Nehir Tokgoz. Experimental and numerical investigation of flow structure in a cylindrical corrugated channel. *International Journal of Mechanical Sciences*, 157:787–801, 2019.

[51] Lucie Ducloué, Laura Casanellas, Simon J. Haward, Robert J. Poole, Manuel A. Alves, Sandra Lerouge, Amy Q. Shen, and Anke Lindner. Secondary flows of viscoelastic fluids in serpentine microchannels. *Microfluid. Nanofluid.*, 23(3):33, February 2019.

[52] R. J. Poole, A. Lindner, and M. A. Alves. Viscoelastic secondary flows in serpentine channels. *J. Non-Newtonian Fluid Mech.*, 201:10–16, November 2013.

[53] Oguzhan Der and Volfango Bertola. An experimental investigation of oil-water flow in a serpentine channel. *International Journal of Multiphase Flow*, page 103327, 2020.

[54] Ivan C. Christov, Vincent Cognet, Tanmay C. Shidhore, and Howard A. Stone. Flow rate–pressure drop relation for deformable shallow microfluidic channels. *J. Fluid Mech.*, 841:267–286, April 2018.

[55] Xiaojia Wang and Ivan C Christov. Theory of the flow-induced deformation of shallow compliant microchannels with thick walls. *Proceedings of the Royal Society A*, 475(2231):20190513, 2019.

[56] Alejandro Martínez-Calvo, Alejandro Sevilla, Gunnar G Peng, and Howard A Stone. Start-up flow in shallow deformable microchannels. *Journal of Fluid Mechanics*, 885, 2020.

[57] Roberto Rusconi, Sigolene Lecuyer, Laura Guglielmini, and Howard A. Stone. Laminar flow around corners triggers the formation of biofilm streamers. *J. R. Soc., Interface*, 7(50):1293–1299, September 2010.

[58] Laura Guglielmini, R. Rusconi, S. Lecuyer, and H. A. Stone. Three-dimensional features in low-Reynolds-number confined corner flows. *J. Fluid Mech.*, 668:33–57, February 2011.

[59] Mohsen Akbari, David Sinton, and Majid Bahrami. Laminar Fully Developed Flow in Periodically Converging–Diverging Microtubes. *Heat Transfer Eng.*, 31(8):628–634, July 2010.

[60] M. Akbari, D. Sinton, and M. Bahrami. Viscous flow in variable cross-section microchannels of arbitrary shapes. *Int. J. Heat Mass Transfer*, 54(17):3970–3978, August 2011.

[61] M. Akbari, A. Tamayol, and M. Bahrami. A General Model for Predicting Low Reynolds Number Flow Pressure Drop in Non-Uniform Microchannels of Non-Circular Cross Section in Continuum and Slip-Flow Regimes. *J. Fluids Eng.*, 135(7):071205, July 2013.

[62] Emil Barić and Helfried Steiner. Extended lubrication theory for generalized couette flow through converging gaps. *International journal of heat and mass transfer*, 99:149–158, 2016.

[63] Rogers Bill Cordova Hinojosa, Kim Pham, and Corinne Rouby. Extension of the lubrication theory for arbitrary wall shape: An asymptotic analysis. *Comptes Rendus Mécanique*, 347(5):389–396, 2019.

[64] Behrouz Tavakol, Guillaume Froehlicher, Douglas P. Holmes, and Howard A. Stone. Extended lubrication theory: improved estimates of flow in channels with variable geometry. *Proc. R. Soc. A.*, 473(2206):20170234, October 2017.

[65] Lailai Zhu and Luca Brandt. The motion of a deforming capsule through a corner. *J. Fluid Mech.*, 770:374–397, May 2015.

[66] Rémi Dangla, François Gallaire, and Charles N. Baroud. Microchannel deformations due to solvent-induced PDMS swelling. *Lab Chip*, 10(21):2972–2978, November 2010.

[67] Bhargav Rallabandi, Naomi Oppenheimer, Matan Yah Ben Zion, and Howard A. Stone. Membrane-induced hydroelastic migration of a particle surfing its own wave. *Nat. Phys.*, 14(12):1211–1215, December 2018.

[68] A. J. Goldman, R. G. Cox, and H. Brenner. Slow viscous motion of a sphere parallel to a plane wall—I Motion through a quiescent fluid. *Chem. Eng. Sci.*, 22(4):637–651, April 1967.

[69] H. A. Stone. On lubrication flows in geometries with zero local curvature. *Chem. Eng. Sci.*, 60(17):4838–4845, September 2005.

[70] J. Y. Jang and M. M. Khonsari. On the granular lubrication theory. *Proc. R. Soc. A.*, 461(2062):3255–3278, October 2005.

[71] Mónica S. N. Oliveira, Lucy E. Rodd, Gareth H. McKinley, and Manuel A. Alves. Simulations of extensional flow in microrheometric devices. *Microfluid. Nanofluid.*, 5(6):809, April 2008.

[72] Konstantinos Zografos, Simon J Haward, and Mónica SN Oliveira. Optimised multi-stream microfluidic designs for controlled extensional deformation. *Microfluidics and Nanofluidics*, 23(12):131, 2019.

[73] Halil L. Tekinalp, Vlastimil Kunc, Gregorio M. Velez-Garcia, Chad E. Duty, Lonnie J. Love, Amit K. Naskar, Craig A. Blue, and Soydan Ozcan. Highly oriented carbon fiber–polymer composites via additive manufacturing. *Compos. Sci. Technol.*, 105:144–150, December 2014.

[74] Louis H. Bangert and Pradipkumar M. Sagdeo. On Fiber Alignment Using Fluid-Dynamic Forces. *Text. Res. J.*, 47(12):773–780, December 1977.

[75] H. A. Stone, A. D. Stroock, and A. Ajdari. Engineering flows in small devices: microfluidics toward a lab-on-a-chip. *Annual Review of Fluid Mechanics*, 36:381–411, 2004.

[76] Shelley Lynn Anna. Droplets and Bubbles in Microfluidic Devices. *Annual Review of Fluid Mechanics*, 48(1):285–309, 2016.

[77] Ian Gibson, David Rosen, and Brent Stucker. *Additive Manufacturing Technologies: 3D Printing, Rapid Prototyping, and Direct Digital Manufacturing*. Springer, November 2014.

[78] Vincenzo Sibillo, Gilberto Pasquariello, Marino Simeone, Vittorio Cristini, and Stefano Guido. Drop Deformation in Microconfined Shear Flow. *Physical Review Letters*, 97(5):054502, August 2006.

[79] Stefano Guido and Valentina Preziosi. Droplet deformation under confined Poiseuille flow. *Advances in Colloid and Interface Science*, 161(1):89–101, December 2010.

[80] Brett P. Conner, Guha P. Manogharan, Ashley N. Martof, Lauren M. Rodomsky, Caitlyn M. Rodomsky, Dakesha C. Jordan, and James W. Limperos. Making sense of 3-D printing: Creating a map of additive manufacturing products and services. *Additive Manufacturing*, 1-4:64–76, 2014.

[81] E A Saibel and N A Macken. The Fluid Mechanics of Lubrication. *Annual Review of Fluid Mechanics*, 5(1):185–212, 1973.

[82] John Happel and Howard Brenner. *Low Reynolds Number Hydrodynamics: With Special Applications to Particulate Media*. Prentice-Hall, 1965.

[83] A. Fasano and F. Rosso. Modelling breakup process of a liquid drop in shear flow. *Applied Mathematical Modelling*, 33(1):315–328, January 2009.

[84] Jonathan J. Stickel and Robert L. Powell. Fluid Mechanics and Rheology of Dense Suspensions. *Annual Review of Fluid Mechanics*, 37(1):129–149, 2005.

[85] J. M. Ottino. *The Kinematics of Mixing: Stretching, Chaos, and Transport*. Cambridge University Press, 1989.

[86] L G Leal. Particle Motions in a Viscous Fluid. *Annual Review of Fluid Mechanics*, 12(1):435–476, 1980.

[87] Douglas E. Leng and Richard V. Calabrese. Immiscible Liquid–Liquid Systems. In *Handbook of Industrial Mixing*, pages 639–753. John Wiley & Sons, 2003.

[88] John R. Lister and Howard A. Stone. Capillary breakup of a viscous thread surrounded by another viscous fluid. *Physics of Fluids*, 10(11):2758–2764, October 1998.

[89] H. A. Stone and L. G. Leal. The influence of initial deformation on drop breakup in subcritical time-dependent flows at low Reynolds numbers. *Journal of Fluid Mechanics*, 206:223–263, September 1989.

[90] G. Ryskin and L. G. Leal. Numerical solution of free-boundary problems in fluid mechanics. Part 3. Bubble deformation in an axisymmetric straining flow. *Journal of Fluid Mechanics*, 148:37–43, November 1984.

[91] I. S. Kang and L. G. Leal. Numerical solution of axisymmetric, unsteady free-boundary problems at finite Reynolds number. II. Deformation of a bubble in a biaxial straining flow. *Physics of Fluids A: Fluid Dynamics*, 1(4):644–660, April 1989.

[92] Kausik Sarkar and William R. Schowalter. Deformation of a two-dimensional drop at non-zero Reynolds number in time-periodic extensional flows: numerical simulation. *Journal of Fluid Mechanics*, 436:177–206, June 2001.

[93] T. Inamuro, R. Tomita, and F. Ogino. Lattice boltzmann simulations of drop deformation and breakup in shear flows. *International Journal of Modern Physics B*, 17(01n02):21–26, January 2003.

[94] J. F. Brady and A. Acrivos. The deformation and breakup of a slender drop in an extensional flow: inertial effects. *Journal of Fluid Mechanics*, 115:443–451, February 1982.

[95] Kapil S. Sheth and C. Pozrikidis. Effects of inertia on the deformation of liquid drops in simple shear flow. *Computers & Fluids*, 24(2):101–119, February 1995.

[96] S. Ramaswamy and L. G. Leal. A note on inertial effects in the deformation of Newtonian drops in a uniaxial extensional flow. *International Journal of Multiphase Flow*, 23(3):561–574, June 1997.

[97] Yuriko Y. Renardy and Vittorio Cristini. Effect of inertia on drop breakup under shear. *Physics of Fluids*, 13(1):7–13, December 2000.

[98] A. J. Wagner, L. M. Wilson, and M. E. Cates. Role of inertia in two-dimensional deformation and breakdown of a droplet. *Physical Review E*, 68(4):045301, October 2003.

[99] Mark Sussman, Peter Smereka, and Stanley Osher. A level set approach for computing solutions to incompressible two-phase flow. *Journal of Computational Physics*, 114(1):146–159, 1994.

[100] Zhipeng Qin, Keegan Delaney, Amir Riaz, and Elias Balaras. Topology preserving advection of implicit interfaces on Cartesian grids. *Journal of Computational Physics*, 290:219–238, June 2015.

[101] Zhipeng Qin, Soheil Esmaeilzadeh, Amir Riaz, and Hamdi A. Tchelepi. Two-phase multiscale numerical framework for modeling thin films on curved solid surfaces in porous media. *Journal of Computational Physics*, 413:109464, July 2020.

[102] Zhipeng Qin, Amir Riaz, and Elias Balaras. A locally second order symmetric method for discontinuous solution of Poisson's equation on uniform cartesian grids. *Computers & Fluids*, 198:104397, February 2020.

[103] Soheil Esmaeilzadeh, Zhipeng Qin, Amir Riaz, and Hamdi A. Tchelepi. Wettability and capillary effects: Dynamics of pinch-off in unconstricted straight capillary tubes. *Physical Review E*, 102(2):023109, August 2020.

[104] M. Brøns, M. C. Thompson, T. Leweke, and K. Hourigan. Vorticity generation and conservation for two-dimensional interfaces and boundaries. *Journal of Fluid Mechanics*, 758:63–93, November 2014.

[105] S. J. Terrington, K. Hourigan, and M. C. Thompson. The generation and conservation of vorticity: deforming interfaces and boundaries in two-dimensional flows. *Journal of Fluid Mechanics*, 890, May 2020.